UNIVERSITY OF CALIFORNIA,
IRVINE

Radiative, Chiroptical & Thermal effects at Illuminated Nanoprobes

DISSERTATION

submitted in partial satisfaction of the requirements
for the degree of

DOCTOR OF PHILOSOPHY

in Electrical and Computer Engineering

by

Abid Anjum Sifat

Dissertation Committee:
Professor Eric O. Potma, Chair
Professor Ozdal Boyraz
Professor Howard Lee

2022

DEDICATION

"In the name of Allah, The Most Gracious and The Most Merciful"
"Praise be to Allah, the Lord of the Universe"
Dedicated to my beloved parents & my caring sister.

TABLE OF CONTENTS

LIST OF FIGURES

ACKNOWLEDGMENTS

There is a list of people who deserve my sincere appreciation. First and foremost, I would like to thank my advisor, Professor Eric O. Potma for giving me the opportunity to work under his supervision. I cherish and appreciate all the academic and intellectual discussions that guided me throughout my Ph.D journey. I thank Professor Potma for engaging me in different scientific problems where I could harness my skills. I really appreciate Professor Potma's patience and kindness in giving an attentive ear to our difficulties, whether academic or non-academic, and providing constructive advice and counseling. In short, my sincere gratitude to Professor Potma for being such an inspiring and supportive leader and above all a wonderful person.

I would like to express my sincere gratitude to Professor Filippo Capolino and members of W.M. Keck lab, particularly Dr. Mohammad Albooyeh, Dr. Jinwei Zeng and Dr. Mohsen Rajaei with whom I started my PhD journey. Dr. Mohammad Albooyeh generously shared his own resources, knowledge and experiences on advanced electromagnetism that eventually helped me strengthen my conceptual knowledge and structure my Ph.D. work. I sincerely acknowledge Dr. Jinwei Zeng from whom I received my fundamental training in optics experiments and microscopy measurements.

I would like to thank all the collaborators and members of the Potma labs. I want to thank Evan Patrick Garcia for making me familiar with the photo-induced force microscopy system and also for assisting me with the measurements. I want to express my gratitude to Dr. Junghoon Jahng and Dr. Bongsu Kim for collaborations on several PiFM projects. I want to thank Yong Li with whom I performed my first optics experiment and also want to acknowledge his immense and generous support regarding computational resources for some of the numerical calculations. Lastly, I want to thank all the current and previous colleagues, including Dave Knez, Dr. Shamsul Abedin and Dr. Richard C. Prince for being such friendly and cooperative peers.

All the work presented in this dissertation is supported by National Science Foundation and W. M. Keck Foundation, U.S.A. I also acknowledge the department of Electrical Engineering and Computer Science and department of Chemistry at UC Irvine for their support through teaching assistant fellowships.

I acknowledge John Wiley & Sons, Ltd.(Journal of Raman spectroscopy), Royal Society of Chemistry(Chemical Society Reviews) and American Chemical Society(ACS Photonics & Journal of Physical Chemistry C) for giving the permission to incorporate the published work into my dissertation.

VITA

Abid Anjum Sifat

EDUCATION

Doctor of Philosophy in Electrical Engineering & Computer Science **2022**
University of California, Irvine *Irvine, CA*

Master of Science in Electrical Engineering & Computer Science **2021**
University of California, Irvine *Irvine, CA*

Bachelor of Science in Electrical & Electronic Engineering **2015**
Bangladesh University of Engineering and Technology *Dhaka, Bangladesh*

RESEARCH EXPERIENCE

Graduate Student Researcher **2017–2022**
University of California, Irvine *Irvine, California*

TEACHING EXPERIENCE

Graduate Teaching Assistant **2018–2021**
University of California, Irvine *Irvine, California*

REFEREED JOURNAL PUBLICATIONS

Abid Anjum Sifat, Filippo Capolino, and Eric O. Potma, "Force Detection of Electromagnetic Chirality of Tightly Focused Laser Beams" **2022**
ACS Photonics 2022, 9, 8, 2660–2667

Abid Anjum Sifat, Junghoon Jahng, and Eric O Potma, "Photo-induced force microscopy (PiFM) – principles and implementations" **2022**
Chem. Soc. Rev., 2022, 51, 4208-4222

Abid Anjum Sifat, and Eric O Potma, "Optimizing the near-field and far-field properties of tips in tip-enhanced Raman scattering" **2021**
Journal of Raman Spectroscopy, 2021, 52 (12), 2018-2028

REFEREED CO-AUTHORED JOURNAL PUBLICATIONS

Bongsu Kim, Junghoon Jahng, Abid Sifat, Eun Seong Lee, and Eric O Potma, "Monitoring fast thermal dynamics at the nanoscale through frequency domain photoinduced force microscopy" **2021**
J. Phys. Chem. C 2021, 125, 13, 7276–7286

Jinwei Zeng, Mohammad Albooyeh, Mohsen Rajaei, Abid Anjum Sifat, Eric O. Potma, H. Kumar Wickramasinghe and Filippo Capolino, "Direct detection of photoinduced magnetic force at the nanoscale reveals magnetic nearfield of structured light " **2022**
Sci. Adv., 2022, 8, 45, eadd0233

Shamsul Abedin, Yong Li, Abid Anjum Sifat, Khokan Roy, and Eric O. Potma, "Enhancement of Molecular Coherent Anti-Stokes Raman Scattering with Silicon Nanoantennas" **2022**
Nano Lett. 2022, 22, 16, 6685–6691

REFEREED CONFERENCE PRESENTATIONS

Abid Anjum Sifat, Filippo Capolino, Eric Potma, "Force detection of electromagnetic beam chirality at the nanoscale" **Jan 2022**
Proc. SPIE PC12017, Complex Light and Optical Forces XVI, PC120170T

SOFTWARE

COMSOL Multiphysics https://www.comsol.com/
RF Module, Heat transfer in Solid Module, Solid mechanics Module

Lumerical https://www.lumerical.com/
FDTD

MATLAB https://www.mathworks.com/products/matlab.html

ABSTRACT OF THE DISSERTATION

Radiative, Chiroptical & Thermal effects at Illuminated Nanoprobes

By

Abid Anjum Sifat

Doctor of Philosophy in Electrical and Computer Engineering

University of California, Irvine, 2022

Professor Eric O. Potma, Chair

Light-based scanning-probe microscopy (SPM) uses a sharp tip with an apex of nanoscopic dimensions for enabling probing at the nanoscale. The region near the tip's apex is called the nanoprobe. When the nanoprobe is brought in close proximity to the sample and it is illuminated, several electrodynamics effects are at play in the tip-sample nanojunction, and these effects can be used to unveil numerous physical and chemical properties of the sample. Even in the absence of any target sample, the electromagnetic interaction at illuminated nanoprobe can bring out interesting properties of the incident light at a scale that is beyond the reach of conventional optical microscopy tools. Whereas the goal of nanoscopic probing is to reveal properties of the sample, the intrinsic response of the nanoprobe itself can sometimes overwhelm the sample's response. This dissertation highlights the above aspects by studying several electrodynamic effects that take place near the illuminated nanoprobe. The first part of the dissertation discusses the near-field enhancement and far-field radiation properties of nanoprobes in tip enhanced Raman spectroscopy (TERS). We numerically design and optimize gold tips decorated with vertical grooves at the tip apex. The proposed designs constitute a feasible route toward a tip fabrication process using focused ion beam (FIB) milling that promises ~ 10 fold stronger TERS signal compared to a conventional TERS tip. In the second part of the dissertation, we theoretically investigate the photo-induced force on an illuminated nanoprobe with nonzero chirality above a bare glass substrate . We find

the differential force due to left circularly polarized (LCP)/right circularly polarized (RCP) is directly related to the chirality of the illuminating light, also known as the helicity density. Under realistic experimental conditions, including the illumination intensity, tip dimension, and the chirality parameter of the tip, we predict that force values can reach several hundreds of fN, just above the noise floor of common force-based SPM techniques, including photo-induced force microscopy (PiFM). Our findings show that a direct characterization of optical chirality at the nanoscale is possible, which may have implications for chiro-optical applications such as enantiomer sorting. In the third and final part of the dissertation, we investigate the thermal expansion of the illuminated nanoprobe and determine the expected relaxation dynamics at the nanoprobe's apex due to light modulation. Finally, we also explore the effect of the tip expansion in PiFM measurements. Our analysis provides important information on the thermal response of the illuminated nanoprobe as well as its impact on PiFM's sensitivity to the thermal response of the sample.

Chapter 1

Introduction

A nanoprobe is a small object of nanoscopic dimensions that, upon optical excitation, produces confined electromagnetic fields in the near zone. Such near-fields provide an opportunity to optically excite a sample, where the length scale of the excitation is defined by the dimensions of the nanoprobe, thus providing a mechanism for achieving high-resolution optical microscopy. When a nanoprobe is attached to a macroscopic structure, such as in the case for an atomically sharp tip attached to a cantilever, then the structure's apex can be used as a local source of optical excitation in a scanning probe microscope (SPM). In such an implementation, the nanoprobe (the tip's apex) can be scanned across the sample, thus enabling high-resolution optical imaging of a wide variety of samples.

The advent of nanotechnology and nanophotonic research has been successful in bringing out novel photo-induced features in different nanostructured elements in the form of nanoantennas [3, 4], nano-cavities [5], nanoparticle assemblies [6, 7] i.e. dimer [8, 9], trimer [10, 11] etc, broken symmetry [5, 9] and chiral nanostructures [12, 13, 14], to name just a few. These studies emphasize that the near-field physics is rich and that numerous phenomena could potentially be leveraged for generating signal contrast for nanoscopic imaging. This notion

applies in particular to SPM, which is not only suitable for mapping topographic features at the nanoscale but is also capable of producing observable signals based on a wide range of electrodynamic effects upon tip illumination. In light-based SPM, it is important to understand such effects, both for a better interpretation of photo-induced SPM contrast as well as a deeper understanding of potential background signals. In this dissertation, we highlight and discuss several notable electrodynamic effects that occur in the vicinity of illuminated nanoprobes. In particular, we study nanoprobe designs with enhanced near-field and far-field properties, discuss the potential of imaging electromagnetic chirality with chiral nanoprobes, and lastly, describe a quantitative measure of laser-induced thermal dynamics at the nanoprobe's apex.

Metallic cones with a sharp apex are the common choice for nanoprobes in SPM. Although the use of gold nanoprobes is typical, other metals such as tungsten [15], silver [16, 17] and even metal-coated dielectrics i.e. silver/gold coated silicon [18] are also regularly used. Upon light illumination, the metallic cone introduces local field enhancement at the apex due to the excitation of localized surface plasmon resonances. When a target molecule is placed in the vicinity of the local evanescent field associated with the plasmon resonance, the optical transition rate in the molecule can be significantly enhanced, which includes electronic transitions and Raman transitions. Furthermore, the radiative properties of the nanoprobe helps with coupling radiation from the molecule's polarization into the far-field, thereby increasing its radiative rate as well as steering radiation into a specific direction, thus improving the collection efficiency of the signal. In fact, optimal nanoprobe design derives from both effects: the near-field enhancement as well as the probe's ability to couple the ensuing radiation into a desired direction for collection. Interestingly, the radiative antenna properties of the nanoprobe are typically overlooked in SPM applications. In the first part of the dissertation, we propose a design of decorated gold tips with vertical grooves for tip-enhanced Raman spectroscopy (TERS) [1], see Figure 1.1. For this purpose, we perform numerical analysis using finite difference time domain (FDTD) methods for optimizing the

probe design, with an emphasis on the feasibility of fabrication based on focused ion beam (FIB) milling. In Section 2.1 of Chapter 2, we present a brief introduction of TERS, followed by a discussion on the details of the simulation model used for the FDTD simulations, including the configuration for light excitation and signal detection. In Chapter 3, we provide an detailed evaluation of the designed tip, showing its promise to increase the far-field TERS intensity by at least an order of magnitude compared to a regular sharp tip.

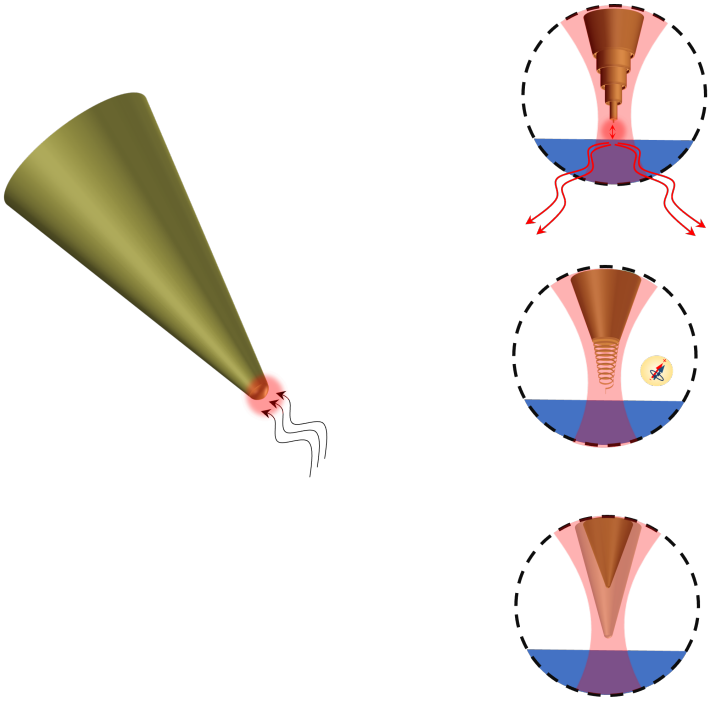

Figure 1.1: Illuminated nanoprobe (a) with enhanced near field and far field response , (b) with non zero chirality (c) experiencing laser induced heating.

Cantilevered tips are commonly used in force-based SPM, such as in atomic force microscopy (AFM) [19]. These tips also form the nanoprobe in light-based scan probe microscopy techniques, with photo-induced force microscopy (PiFM) as the prime example [20]. Contrary to emission/scattering based SPM techniques like TERS and apertureless (or scattering) scanning nearfield optical microscopy (a-SNOM or s-SNOM) [21, 22], PiFM measures the cantilever dynamics to determine the forces acting on it. The observed force carries signatures

of tip-sample interactions as well as any photo-induced response of the sample underneath the tip. In section 2.2 of Chapter 2, we present the operating principles of PiFM along with a discussion on various contributions to the photoinduced force that can be manifest in a PiFM experiment. The detected forces in PiFM derive from various mechanisms. Originally conceived for probing the instantaneous electromagnetic force between the tip and the sample [20, 23] it has become clear that other contributions to the force play a role as well. Among other forces, the one derived from light absorption by the sample or tip, and the subsequent thermal expansion of the sample [2, 24, 25, 26, 27, 28] is of particular relevance in this dissertation.

In PiFM, the nanoprobe itself plays significant role in manipulating the observed signal even without the presence of any sample under it. For instance, using a scanning gold-coated silicon probe over a bare glass slip, the electric field distribution of an incident focused light field has been mapped with the PiFM principle [29, 30, 31]. In addition, the distribution of the magnetic component of structured light near focus has been visualized with the aid of a truncated silicon cone in the PiFM microscope [32, 33]. This indicates a potential route for studying the hidden or otherwise invisible properties of light at the nanoscale. In the second part of the dissertation, in Chapter 4, we theoretically investigate the photo-induced force exerted on a chiral nanoprobe under differential illumination with either right handed circularly polarized (RCP) or left handed circularly polarized (LCP) light. Using image dipole theory, we have found a direct relation between the calculated differential force and the chiral properties of the incident electromagnetic field, namely helicity density. We further examine numerous design considerations modeling the chiral nanoprobe as a chiral nanosphere using a Mie formalism and complement our dipole model with full-wave, finite element method (FEM) simulations.

Over the years since 2010, PiFM has been used to detect electronic resonances [20] in the visible range to vibrational transitions in the mid-infrared range [24, 34, 35], to probe nonlinear

polarizations in the sample, resulting in images based on stimulated Raman transitions [36] and pump–probe transitions [37, 38]. In addition, depending on the sample's absorption coefficient, thermal diffusivity and the illuminated sample volume, PiFM experiments can detect thermal effects related to sample expansion [2, 28]. A recent implementation of PiFM named Fourier transform PiFM (FT-PiFM) has been shown to be sensitive to force dynamics on a sub-μs timescale due to the relaxation of the sample's thermal expansion [39]. In these measurements, along with the sample, the illuminated nanoprobe also undergoes laser-induced heating and subsequent expansion. In general, the relevant nanoprobe expansion is considered negligible compared to the sample expansion. However, for tip sample distances of few nanometers the nanoprobe expansion can still affect the distance-dependent force observed in PiFM. In the third part of the dissertation, we numerically investigate the laser modulation induced thermal expansion at the nanoprobe apex and subsequent relaxation dynamics. Furthermore, we validate our numerical analysis with experimental measurements using the FT-PiFM model. In Section 2.2.2 of Chapter 2, we introduce the principles of FT-PiFM and also presented a simple model for extracting the relaxation time of the expanded sample within a single cycle of the laser modulation. In Chapter 5, we present a numerical model based on FEM to calculate the laser modulation induced thermal expansion and relaxation dynamics at the nanoprobe's apex for bare silicon and gold coated silicon tips. We perform FT-PiFM measurements on the nanoprobes above a bare glass coverslip to determine the relaxation time during typical measurement conditions, and show that these results corroborate the simulations. Finally, we use the tip expansion parameters to study its implications for the thermal contribution to the PiFM signal. While the tip's effect barely changes the PiFM response for a broad range of sample expansion lengths and relaxation times, we find a noticeable impact of tip expansion on PiFM's sensitivity when samples are studied that are thin, below a threshold thickness which depends on the thermal properties of the sample, and that exhibit a fast thermal relaxation time [2, 28].

Chapter 2

Nanoprobe-based Spectroscopy and Microscopy - Methods & Principles

Scanning probe Microscopy (SPM) enables optical imaging with nanoscale resolution. When combined with light, SPM makes it possible to perform optical probing at a spatial resolution that is well beyond the diffraction limit. Among numerous light-based scan probe techniques, two particular methods, namely tip enhanced Raman spectroscopy (TERS) and photo-induced force microscopy (PiFM), are highlighted in this Chapter, as the topics discussed in the subsequent Chapters are directly related to these techniques.

In TERS, the inherently weak Raman scattering of molecular vibrational modes is enhanced in the presence of the sharp tip. An illuminated sharp tip in the vicinity of a Raman active molecule not only boosts the Raman polarization through local field enhancement, but also works as a nanoantenna to efficiently couple the radiating polarization to the far field.

PiFM is an imaging technique based on raster-scanning a sharp tip across the sample. When the tip is illuminated with light, it experiences an extra force due to the light-induced interactions between the sample and probe. This so-called photo-induced force constitutes

the contrast mechanism in PiFM images.

This chapter provides an introductory description of both TERS and PiFM techniques. In addition, a proposed simulation model of TERS is presented in section 2.1 that provides insight into the near-field and far-field contributions to the TERS signal as well as a proper comparison between free-space Raman and tip-enhanced Raman processes. In section 2.2, several major physical origins of the photo-induced force are discussed along with a brief description of a newly proposed Fourier transform PiFM that is capable of sensing force dynamics on μs time scales.

2.1 Tip enhanced Raman Spectroscopy (TERS)

A typical TERS configuration is illustrated in Fig. 2.1 where the sample containing the Raman active bonds is placed underneath a sharp metallic tip. The tip or the sample stage is scanned to produce an image with spectroscopic contrast and nanoscale resolution. Upon light illumination, the localized surface plasmon at the tip apex introduces significant field enhancement (EF) near the sample location, which is an important indicator of TERS signal enhancement compared to the regular Raman signal. Although the Figure shows that the the light is incident from the bottom of the AFM based system, other configurations are commonly used as well, including top or side illumination [40, 41], excitation by surface plasmon polaritons (SPP) [42] with either a scanning tunneling microscope (STM) tip [43] or a tuning fork mounted tip [44]. In TERS, the Raman shifted signal from the vibrational modes in the sample is re-scattered by the tip with enhanced directivity and eventually captured by a collection lens before it is filtered and detected by a photo-detector. Since a precise analytical modeling of the re-scattering is quite complicated, TERS enhancement is conventionally described by an overall factor of $(EF)^4$. However, this description does not explicitly take the direction specific radiation properties of the tip antenna system into

account.[45]

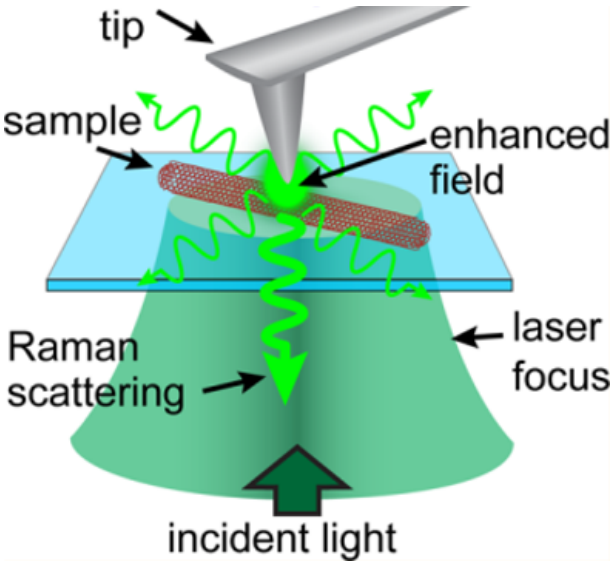

Figure 2.1: Illustration of an AFM-based TERS measurement system [1]

.

A proper numerical modelling of the TERS system would include the radiation aspect of the tip. This can provide a better understanding of the overall TERS enhancement, capturing both the localized near-field and radiating far-field action of the nanoprobe. In the following subsections, a simplified numerical model of TERS, based on finite difference time domain (FDTD) calculation, is presented and discussed. The results are compared with those of regular Raman scattering.

2.1.1 Simulation methods in FDTD

Figure 2.2 shows the 3D schematics of a regular TERS simulation model. The incident light is an x-polarized plane wave that is focused by a high numerical aperture (NA) objective (NA = 1.2 oil, $n_{\text{oil}} = 1.51$) onto the sample surface. The substrate consists of a semi-infinite glass substrate of $\varepsilon_{\text{glass}} = 2.25$ and a 200 nm thick polymeric host medium of poly-methyl

methacrylate (PMMA) with $\varepsilon_{\text{host}} = 3$. The molecular targets are modeled as point dipoles that are placed atop the host medium. The gold tip is modeled as a cone with a cone angle of 20^o. The dielectric permittivity of gold is taken from reference [46] and fitted by a Drude-Lorentz dispersion model. The simulation region is optimized by modeling the tip shaft up to 10 μm to minimize reflection from the tip's upper edge [47]. Note that a sufficiently long shaft is needed in the simulation to suppress finite size effects at the top of the tip's cut-off [47, 48]. A perfectly matched layer (PML) of sufficient thickness is imposed on the rectangular boundary to eliminate and reduce unwanted reflections from the simulation domain boundary. All the material media including the tip, host layer and the substrate extend into the PML region to mimic an infinitely extended system. As shown in Fig. 2.2, three different tip geometries are considered: a) a sharp tip with a tip apex radius of 10 nm; b) a modified tip made from a blunt tip of 50 nm apex radius; c) a tip modified with vertical grooves. The design details and performance evaluations are elaborately discussed in Chapter 3 .

FDTD simulations are performed to determine the far-field intensity pattern radiated by the light-induced dipole that is placed in the vicinity of the gold tip. Due to the azimuthal symmetry of the system under consideration, the simulations are preformed in two dimensions (2D). A 1 nm separation between the tip and the molecule is assumed in all simulations. Near the molecule and near sharp features, a small mesh size of 0.1 nm is used to avoid discretization errors. The calculations are divided into two steps. First, the local fields in the near-field are calculated in the time domain $[\mathbf{E}_{\text{loc}}(t, r), \mathbf{H}_{\text{loc}}(t, r)]$ without the presence of the molecule. A Fourier transform is performed to obtain the local fields in the frequency domain $[\mathbf{E}_{\text{loc}}(\omega), \mathbf{H}_{\text{loc}}(\omega)]$ at the location of the molecule. In the second step, the molecule is placed at the desired location and its dipole moment is computed as $\mathbf{p} = \alpha \mathbf{E}_{loc}$, where α is the (relative) Raman polarizability.

The far-field intensity profile $I(\theta)$ is calculated by a near-to-far-field projection method in

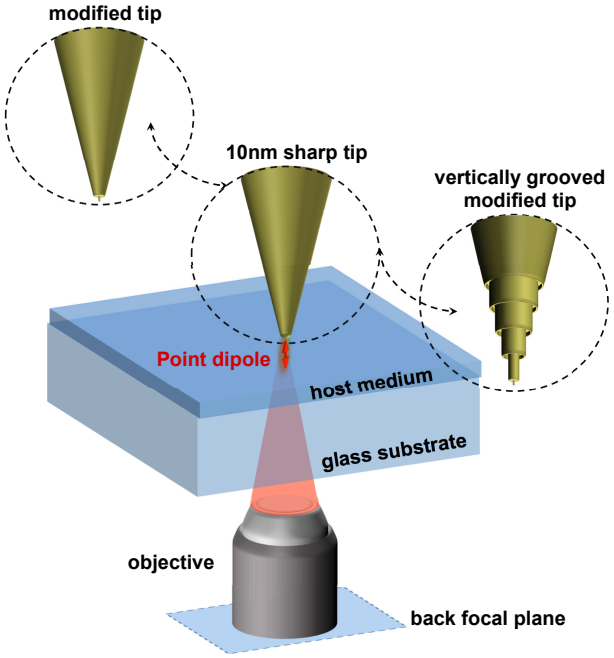

Figure 2.2: Schematics of the simulation model. Linearly polarized incident light is focused on the top surface of the host medium by an 1.2 NA objective. The radiated signal from the tip-sample junction is collected in epi-mode and the normalized intensity is mapped in the back focal plane. Three different types of gold tips (10 nm sharp tip, modified tip, vertically grooved modified tip) are considered. The modified tip and vertically grooved modified tip are discussed in detail in the later chapter.

the bottom-half plane. In this method, the field intensity on a hemispherical surface of 1 m radius is calculated as the angular spectrum of near zone data in the vicinity of the scatterer in the simulation domain. The basis of the angular spectrum is a set of plane waves that propagate at different angles and are weighted by the near-zone data [23]. See reference [23, 49] for more details on the near-to-far-field projection method. Here, the near-zone data is collected along a horizontal line (virtual detector) that is placed near the dipole source in the glass substrate. The horizontal line is sufficiently long to capture the majority of radiation in the bottom-half plane. The average far-field radiation is computed from an ensemble of isotropically polarizable molecules in the focal plane, and use the resulting response as a reference indicative of the signal measured in conventional Raman microscopy. The normalized far-field Raman signal serves as an effective single molecule response in the absence of the tip. To represent the TERS measurement, a tip is placed in the focal field and

the far-field radiation is computed in a similar fashion. Furthermore, the 2D data is used to reconstruct the intensity distribution in the back focal plane of the microscope objective.

The total detected intensity is obtained by integrating $I(\theta)$ over the detection surface as:

$$I_{\text{tot}} = \int_0^{\theta_{\max}} \int_0^{2\pi} I(\theta) \sin(\theta) d\theta d\phi \tag{2.1}$$

where $\theta_{\max}$ is the maximum collection angle of the objective lens and ϕ is the azimuthal angle.

2.1.2 Bulk Raman response versus tip-enhanced Raman scattering

In this subsection, the distinctions between the near-field distribution and the far-field behavior is discussed for the processes of regular Raman and TERS. First, the excitation fields in the near-field zone are considered for regular Raman excitation without the presence of a tip. The incident light is a 650 nm x-polarized plane wave propagating in the y-direction and focused by the objective lens, as shown in Figure 2.3(a). The profile of the incident beam's horizontal $|\mathbf{E}_{\text{inc,x}}|$ and vertical $|\mathbf{E}_{\text{inc,y}}|$ components in the simulation plane (xy) is shown in Figure 2.3(b) and (c), which display the well-known focal fields of linearly polarized light[23].

For the tip-enhanced Raman process, a sharp gold tip with a 10 nm apex radius is placed in the focal field, with a molecular dipole placed in the top layer of the dielectric host medium, directly underneath the tip apex, as shown in Figure 2.3(d). To ensure efficient enhancement along y, the tip apex is placed in the location of maximum $|\mathbf{E}_{\text{inc,y}}|$, as indicated by the white dashed line in Figure 2.3(c). Figures 2.3(e) and (f) show the magnitude of the total, y-component and x-component of the local electric field enhancement along the lateral dimension (black dashed line in Figure 2.3(d)) and axial dimension (green dashed line in Figure 2.3(d)) starting from the tip edge. All the local field enhancements are normalized

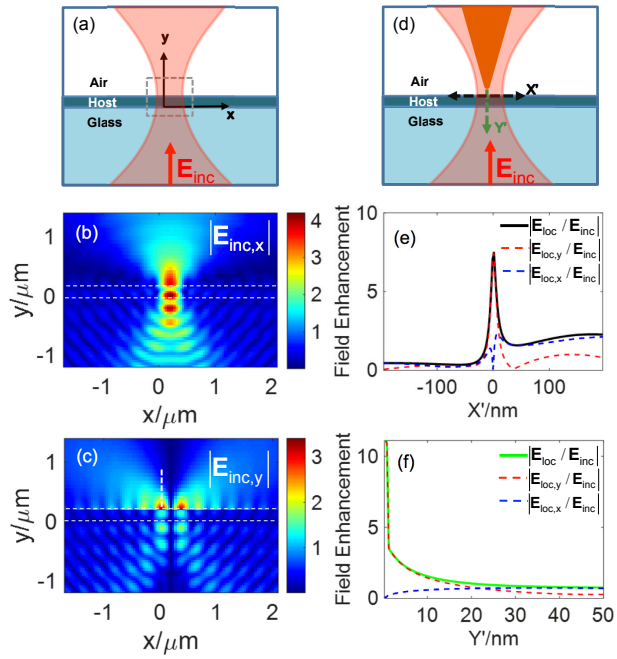

Figure 2.3: Near-field distribution in regular and tip-enhanced excitation schemes. (a) Schematic of the excitation scheme without tip. (b) Magnitude of the x-polarized component of the focal field $|\mathbf{E}_{\mathrm{inc,x}}|$. (c) Magnitude of the y-polarized component of the focal field $|\mathbf{E}_{\mathrm{inc,y}}|$. The white dotted lines denote the interfaces between air (upper), host (middle) and glass (bottom) media. (d) Schematic of the excitation scheme in the presence of a tip with 10 nm radius. The tip is placed at the point of maximum $|\mathbf{E}_{\mathrm{inc,y}}|$ indicated by the white dashed line in panel (c). (e) Magnitude of the total (black), y-component (red) and x-component (blue) of the local electric field enhancement along the black dashed line in panel (d). (f) Magnitude of the total (green), y-component (red) and x-component (blue) of the local electric field enhancement along the green dashed line in panel (d). The field enhancements in panel (e) and (f) are normalized relative to the maximum $|\mathbf{E}_{\mathrm{inc,y}}|$ component of the incident focused field on the substrate surface shown in panel (c)

relative to the maximum $|\mathbf{E}_{\mathrm{inc,y}}|$ component on the substrate surface. The field enhancement under the tip apex in the top of the host layer displays a peak value of ~ 7 with a FWHM of 6 nm in the lateral dimension. The right tail in Figure 2.3(e) exhibits a secondary bump which traces the profile of the incident focal field. The field enhancement in the axial direction shows a peak of ~ 11 right under the tip apex, reaching a value of ~ 7 on the host surface and finally decays dramatically inside the host layer. It is evident from both Figures 2.3(e) and 2.3(f) that the y-component is the dominant contribution in the local field enhancement. Note that the current near-field enhancements are generally lower than what

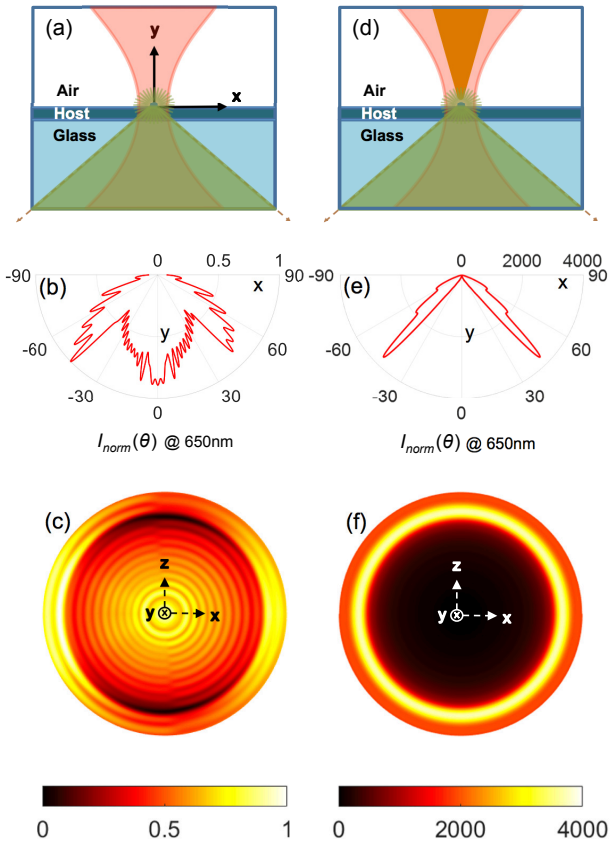

Figure 2.4: (a) Schematic of dipole radiation in conventional Raman microscopy. (b) The normalized far-field intensity from an ensemble of dipoles radiated into the xy-bottom half plane at 650 nm. (c) Intensity map of the Raman radiation in the back focal plane of the objective lens. (d) Schematic of tip-enhanced point dipole radiation using a tip of 10 nm radius. (e) The far-field intensity in the xy-bottom half plane relative to the maximum intensity found for a vertical dipole at the same location without the tip. (f) The far-field intensity in the back focal plane of the objective lens.

has been reported in previous simulations of TERS-type tips. We attribute this difference in part to possible artifacts related to the finite tip size, which have been carefully suppressed in the proposed simulation model.

We next calculate the Raman radiation profile of molecular targets that are placed in the layer of the host medium in the absence of the tip. This situation corresponds to a conventional Raman microscopy measurement. The geometry of the experiment is as sketched in Figure 2.4(a). For this purpose, the molecular targets are assumed to exhibit an isotropic polarizability so that they are efficiently excited by the incident field. The simulation keeps the

focal fields fixed while molecules are distributed at random positions along the x-dimension. Possible near-field coupling among the dipoles is not considered in this calculation. The resulting radiation from the molecular ensemble is averaged and normalized to its maximum value, and displayed in Figure 2.4(b) for the 650 nm radiation wavelength. To note, the incident wavelength in the study is set at 650 nm, thus ignoring the possible differences in EF at the excitation and radiation wavelengths [48]. These difference are small and do not affect the general trends found. The averaged radiation pattern of the molecular ensemble shows directional emission at angles above the critical angle of $\sin^{-1}(1/n_{\text{glass}}) = 41.81^o$ [23], a direct consequence of the presence of the substrate/air interface. The signal component at these higher angles originates from dipoles that are driven in both the x- and the y-directions in the near-field. In addition, at lower angles direct dipolar radiation is observed that is mostly x-polarized. Figure 2.4(c) shows the calculated radiation in the back focal plane of the objective lens. This plot emphasizes that in a regular Raman microscopy experiment with randomly oriented molecules, a high numerical objective with a collection angle well above the critical angle is needed to capture the majority of the radiation into the epi-direction.

We next simulate the far-field radiation pattern in the presence of the tip by placing a single y-oriented molecular dipole directly underneath the tip apex, as shown in Figure 2.4(d). The far-field radiation pattern in the xy-plane is shown in Figure 2.4(e). To determine the signal enhancement, the tip-enhanced intensity is computed relative to the maximum intensity found for a vertical molecular dipole at the same location without the tip. Compared to the normalized intensity pattern of the ensemble average, the tip-enhanced far-field signal displays a highly directional profile that peaks at an angle of $\pm 44^o$, in agreement with findings previously reported [50]. This directional radiation reflects the strong enhancement of the y-component of the focal field by the tip, resulting in enhanced radiation at angles near and above the critical angle. Dipoles driven in the x-direction do not benefit from this directional enhancement, which is reflected in the absence of a radiation contribution that resembles that of x-polarized molecular dipoles.

Besides altering the radiation direction, the tip also increases the signal intensity $I_{\text{norm}}(\pm 44^o)$ by $\sim 3,700$ times compared to the single dipole signal without the tip. In addition, we calculate the total normalized intensity detected by the 1.2 NA oil immersion objective ($\theta_{\max} = 52.6^o$) using (2.1). It is helpful to relate the enhancement thus found to the typical TERS enhancement factor of $(EF)^4$. For this purpose, we may define the total intensity relative to that of a single dipole without the tip ($I_{\text{enh}} = I_{\text{tot}}^{\text{tip}}/I_{\text{tot}}^{\text{no tip}}$) as $I_{\text{enh}} = (EF)^4 \times AE$, where EF is the *near-field* enhancement factor, and AE is an effective measure of the antenna's *far-field* radiation efficiency. For the 10 nm radius tip considered here we observe $EF = 7$ and AE is found to be 1.43. Figure 2.4(f) shows the intensity distribution in the back focal plane. It is evident that the tip directs Raman scattered radiation into larger collection angles, revealing a profile of azimuthal symmetry that differs markedly from the light distribution seen in regular Raman microscopy, as in Figure 2.4(c). In Chapter 3, we use the simulation model above to study the expected TERS signal for tips that are designed to optimize both the near-field enhancement as well as the antenna's radiation efficiency.

2.2 Photo-induced force Microscopy (PiFM)

In the most basic implementation, the PiFM system is a scan probe microscope based on tapping-mode AFM [51]. Since the demonstration of PiFM in 2010 [20], amplitude modulated PiFM (AM-PiFM) is the most commonly used configuration of the technique, and the layout of the AM-PiFM microscope is sketched in Figure 2.5. The main component of the system is the cantilever beam which is equipped with a sharp tip. The latter is typically gold-coated to increase the polarizability of the tip's apex. The motions of the cantilever are measured with high precision by illuminating its backside with a laser beam (feedback laser), which is reflected off the cantilever's surface and detected with a quadrant photodiode. The sample is placed on a glass coverslip and is illuminated from below in an inverted microscope

configuration, although side-on illumination schemes are also common. The tip is positioned in close proximity to the sample and externally driven by a dithering piezoelectric element to force an oscillatory motion of the cantilever beam. The driving frequency is chosen to coincide with the mechanical resonance of the cantilever. In many PiFM measurements, the second mechanical resonance of the cantilever at frequency f_2 is chosen for recording the topographic AFM signal, which implies that the driving frequency is tuned to f_2. The PiFM signal is then derived from the cantilever's motions at its first mechanical resonance at frequency f_1. The roles of the f_1 and f_2 frequency channels can be reversed.

The incident light is amplitude modulated at f_m, which can be accomplished with an acousto-optic modulator (AOM). The light is subsequently focused at the tip-sample nano-junction with a high numerical aperture lens from below or with an off-axis parabolic mirror from the side. In the presence of photo-induced forces, the cantilever develops motions that depend on f_m, and these motions can be detected by analyzing the signal of the quadrant photodiode. In a typical configuration, a lock-in amplifier is used to demodulate the photodiode signal at pre-selected detection frequencies. To extract the photo-induced force in the AM-PiFM instrument, the demodulation frequency is tuned near f_1. There are two common detection modes: homodyne and heterodyne. In the homodyne detection mode, also known as the direct mode, f_m is adjusted to coincide with f_1, i.e. $f_m = f_1$. In this setting, the modulation of the incident light produces a force that is directly manifest at the first mechanical resonance of the cantilever. In the heterodyne detection mode, sometimes referred to as the sideband detection mode, the laser modulation is performed at the difference frequency ($f_m = |f_1 - f_2|$) or sum frequency ($f_m = |f_1 + f_2|$) of the cantilever resonance frequencies. Once again, the signal is demodulated near mechanical resonance frequency f_1, which now registers an optically induced force at a sideband of the second mechanical resonance, i.e. $f_1 = |f_2 \pm f_m|$. While the homodyne mode is sensitive to the photo-induced force itself, the heterodyne detection mode probes the gradient of the photo-induced force [31, 52].

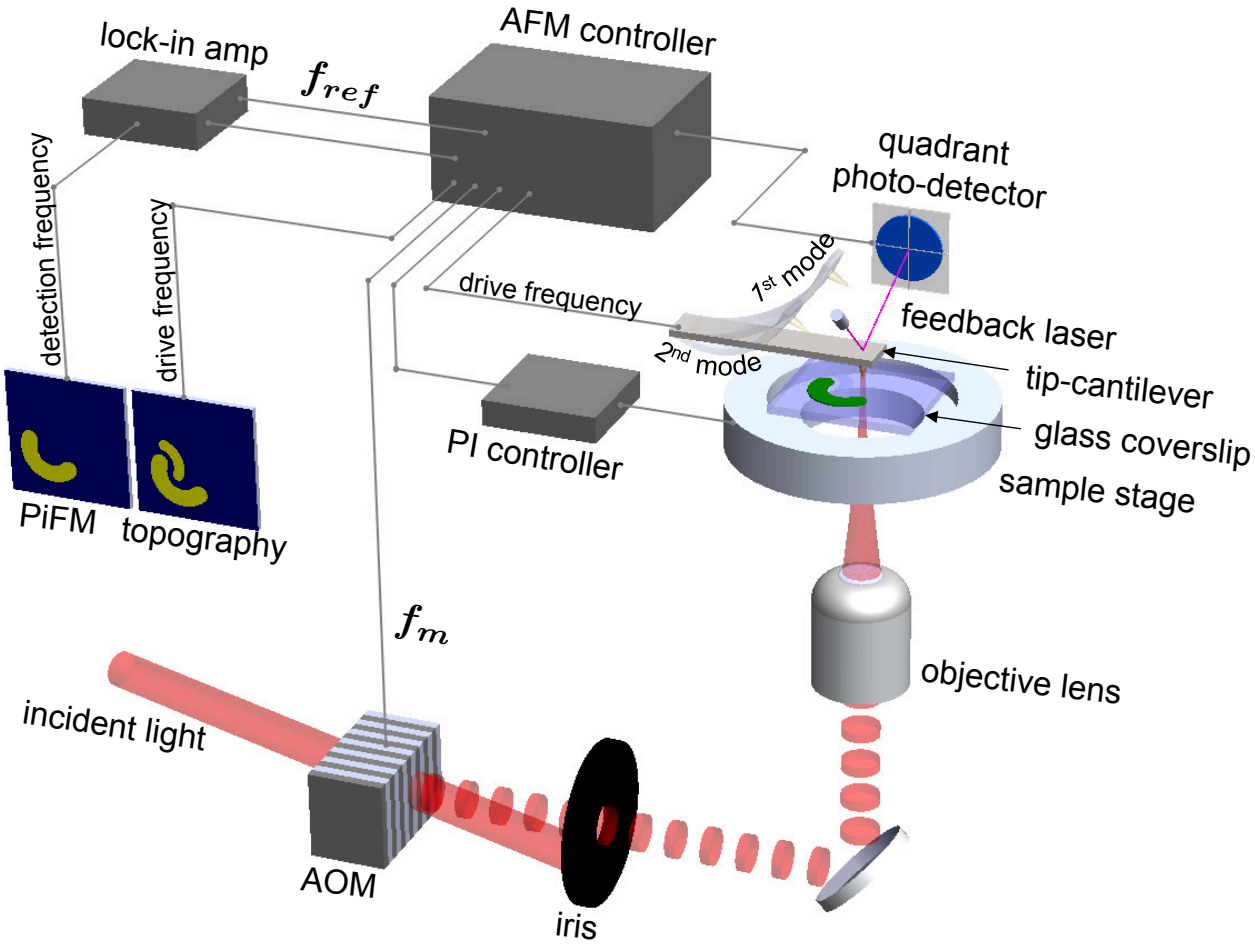

Figure 2.5: Simplified schematics of AM-PiFM. AOM denotes the acoustic optic modulator, f_m is the modulation frequency, f_{ref} is the reference frequency of the lock-in amplifier that is the same as detection frequency.

In the following Section, we describe the major physical mechanisms that contribute to the photo-induced force, including the electromagnetic force and expansion forces. In Section 2.2.2, we also discuss a specific implementation of PiFM, namely a frequency domain version of AM-PiFM, which is sensitive to force dynamics on μs time scales in PiFM measurements.

2.2.1 Physical origin of the photo-induced force

The physics of the illuminated tip-sample junction is complicated, and it comes as no surprise that the detected forces in PiFM derive from various mechanisms. Depending on the

geometry of the experiment, wavelength setting and properties of the material, the instantaneous electromagnetic force may be inferior to other photo-induced forces. Chiefly among these are forces that are derived from light absorption by the sample or tip, and the thermal expansion of the sample that follows [24, 25, 26, 27, 28]. In this subsection, some of the major contributions to the force are discussed that can be manifest in a PiFM experiment.

Photo-induced electromagnetic force

When the cantilevered tip is illuminated, charge oscillations in the tip's material produce an induced polarization at the optical driving frequency. In most cases, this polarization can be approximated well as an oscillating dipole in the form $p_t = \alpha_t E$, where $\alpha_t = \alpha_t' + i\alpha_t''$ is the polarizability of the tip and E is the optical driving field. For simplicity, the polarizaibility is assumed a scalar quantity. The oscillating dipole experiences a time-averaged, electromagnetic force that is proportional to the gradient of the driving field as follows:

$$\langle F \rangle = \frac{\alpha_t'}{2} \sum_i \mathrm{Re}\left\{E_i^* \nabla E_i\right\} + \frac{\alpha_t''}{2} \sum_i \mathrm{Im}\left\{E_i^* \nabla E_i\right\} \tag{2.2}$$

where $i = \{x, y, z\}$ labels the Cartesian components. The first term in equation (2.2) is proportional to the real part of the tip's polarizability, and is a non-dissipative, conservative force [23, 31]. This term is related to the so-called gradient force. The second term in equation (2.2) is a dissipative, non-conservative force, which is proportional to the imaginary part of α_t. This force is related to the transfer of momentum of the scattered light and is called the scattering force [23].

The first term in particular is sensitive to the gradient of the optical field in the vicinity of the tip. A steeper gradient produces a stronger force. For instance, the force can be expected to be strong when the tip is placed near the strong local fields associated with surface plasmon resonances [53], which show a significant spatial dependence on the nanoscale, near objects

that display localized surface plasmons [39, 54], or material surfaces that support collective modes such as phonon polaritons [55, 56].

The details of the local field also change when the tip is brought into close proximity to the surface of dielectric substrates or objects, which in turn alters the photo-induced force. The resulting force can be modeled conveniently with image dipole theory as illustrated in Figure 2.6(a). Writing the image dipole as $p_{t'}$ with polarizability $\alpha_{t'}$, and assuming that the dominant polarization direction is along z, the distance-dependence force directed along the z-axis can be expressed as [31]:

$$\langle F_g \rangle_z \simeq -\frac{3\mathrm{Re}\{\alpha_t \alpha_{t'}^*\}}{4\pi\varepsilon_0\varepsilon_m z^4}|E_z|^2 \tag{2.3}$$

where ε_m is the permittivity of the medium surrounding the tip. This force referred to as the gradient force in this thesis, explicitly depends on the distance z between the tip and image dipoles, and scales as z^{-4}. Therefore, the optical gradient force is strongest when the tip-sample distance is small, whereas it falls off quickly when the tip is retracted. The negative sign indicates that the force is attractive. Since the magnitude of the image dipole depends on the permittivity of the substrate material, the magnitude of the photo-induced force felt by the tip is sensitive to the properties of the material underneath it.

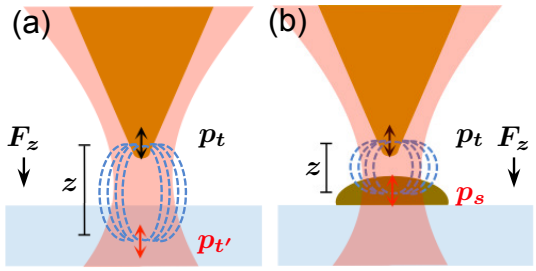

Figure 2.6: Illustration of (a) the image dipole force above the substrate, and (b) the dipole-dipole interaction force between tip and sample. z is the average distance of the tip dipole p_t from the image dipoles p_t' in (a), and from the sample dipole p_s in (b)

Dipole-dipole interaction force

Consider a small object, such as a cluster of molecules, that is illuminated by a focused light field. At the microscopic level the induced polarization of the sample is $p_s = \alpha_s E$, where $\alpha_s = \alpha_s' + i\alpha_s''$ is the polarizability of the sample. The real and imaginary parts of the polarizability is considered to follow the lorentzian lineshape near a single optical resonance of the sample [57]. The presence of p_s affects the local field near the induced dipole of the tip and thus has an effect on the electromagnetic force exerted on the tip [57]. Figure 2.6(b) shows a schematic of the interaction between the oscillating dipoles as mediated by the local electromagnetic field. This interaction is sometimes called the dipole-dipole force, and the time averaged dipole-dipole gradient force can be written as:

$$\langle F_g \rangle_z \simeq -\frac{3\mathrm{Re}\{\alpha_t \alpha_s^*\}}{4\pi\varepsilon_0\varepsilon_m z^4}|E_z|^2 \tag{2.4}$$

which also displays a z^{-4} dependence. The spectral response is proportional to $\mathrm{Re}\{\alpha_t\alpha_s^*\} \propto \{\alpha_t'\alpha_s' + \alpha_t''\alpha_s''\}$. For a typical metal, $\alpha_t' \gg \alpha_t''$ over the visible to infrared spectral range [25]. Under these conditions, the spectral response for the dipole-dipole gradient force assumes a characteristic dispersive lineshape. The presence of a dispersive lineshape in the photo-induced force near an optical resonance is thus an indication that the dipole-dipole force is a prominent contribution to the PiFM measurement. Calculations show that the optical gradient force that can be expected between the tip and a small nanometer-sized structure, such as a molecular cluster or quantum dot, is on the order of a pN [57]. Though small, such forces can still be measured with confidence in the PiFM microscope.

Photo-thermal expansion force

Photo-thermal expansion forces follow from the sample expansion after light absorption, shown schematically in Figure 2.7(a). The thermal expansion ΔL of the sample is related

to the rise in temperature, ΔT, at the location of laser illumination. The expansion can be modeled as $\Delta L \approx \alpha_T h \Delta T$, where h is the sample thickness and α_T is the linear thermal expansion coefficient of the sample [28, 58, 59]. ΔT can be obtained by solving heat equation with the incident light power as the heat source [28, 58]. Note that the photo-thermal expansion is a direct function of the sample thickness whereas the dipole-dipole interaction force is virtually insensitive to h [26]. For organic materials in the $h \sim 1 - 100$ nm range the material expansion is typically very small, on the order of $\Delta L \sim 1 - 100$ pm, which is often smaller than the size of an atom!

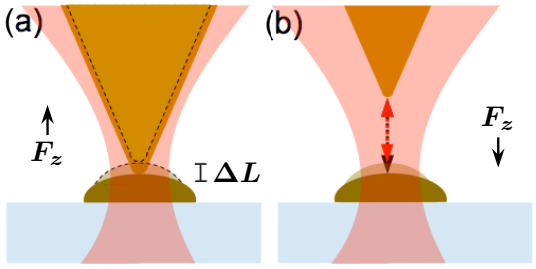

Figure 2.7: Sketch of (a) the thermal expansion force in contact mode, and (b) the thermally modulated van der Waals force contribution in non-contact PiFM. Modulation of the incident light produces a modulation in tip-sample distance, ΔL. This in turn results in modulation of van der Waals force (black arrow to red arrow) at f_m.

Nonetheless, such height variations can still be detected through changes in the force. In general, even in the absence of light, the tip experiences an interaction force due to its proximity to the sample. This tip-sample interaction force, $F_{ts}(z)$, is described well as the sum of conservative and non-conservative forces given by $F_{ts}(z) = F_c(z) - \Gamma(z)\dot{z}$, where F_c is the conservative force and $\Gamma(z)$ represents an effective damping coefficient of a given dissapative process [31, 52]. The F_{ts} strongly depends on the tip-sample distance and contains attractive and repulsive contributions. Figure 2.8 shows F_{ts} as a function of z. In the non-contact zone, F_{ts} is dominated by attractive forces, such as the van der Waals (vdW) force, whereas in the contact zone repulsive forces become the dominant force. At $z = 0$ and shorter distances the tip is in full contact with the sample and F_{ts} is exclusively repulsive. Such forces are described well by the Derjaguin–Muller–Toporov (DMT) model.

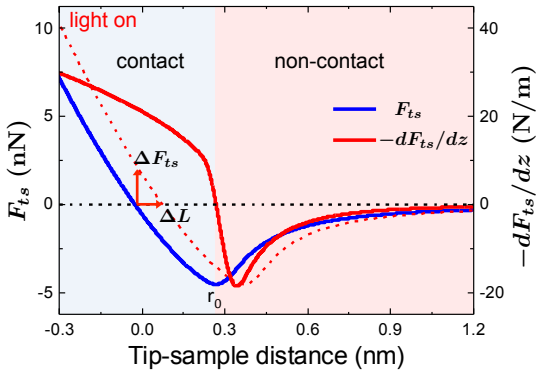

Figure 2.8: Effect of the thermal expansion ΔL on the tip-sample interaction force F_{ts}. Blue curve shows F_{ts} when the light is off, while red dashed curve shows F_{ts} when the light is on. Red solid curve shows -$\partial F_{ts}/\partial z$, which is proportional to the magnitude of the thermal expansion force.[2]

Both vdW force and the DMT force depend on z. Sample expansion causes a change in the tip-sample distance, and thus produces a difference in the force:

$$\Delta F_{ts}(z) = F_{ts}(z - \Delta L) - F_{ts}(z) \tag{2.5}$$

The effect of the light-induced sample expansion is given by the dashed red curve in Figure 2.8, which emphasizes that there is a periodic force difference due to a periodic modulation of the light, both in the contact and non-contact zones. In the small oscillation limit, the tip-sample force can be expanded in a Taylor series around the average position z_c, which in the first-order approximation takes on the form:

$$F_{ts} \approx F_{ts}(z_c) + \frac{\partial F_{ts}}{\partial z}(z - z_c) + ... \tag{2.6}$$

so that the force difference can be generally expressed as:

$$\Delta F_{\mathrm{ts}}(z) \approx -\frac{\partial F_{ts}}{\partial z}\Delta L \tag{2.7}$$

The magnitude of the force difference is thus related to the spatial derivative of the tip-sample force, shown by the red curve in Figure 2.8. In the contact zone, using a DMT model

for F_{ts}, the thermal expansion force F_{th} can be written as:[59]

$$F_{th}(z) = \Delta F_{ts}(z) \approx 2\text{E}^* \sqrt{R(r_o - z)} \cdot \Delta L = C(z) \cdot \Delta L \tag{2.8}$$

where E^* is the reduced Young's modulus of the material, R is the radius of the tip, r_o is the intermolecular distance in the material and $r_o - z$ is the indentation depth. The repulsive expansion force depends linearly on ΔL. Since ΔL is modulated at f_m in a PiFM experiment, the repulsive force F_{th} shows up as PiFM signal when operated in contact mode. Even for small ΔL, F_{th} can be significant. For instance, for molecular monolayers, a value for $C(z)$ as high as $\sim$ 40 N/m has been reported, so that the force measures 130 pN for a sample expansion of only 3.2 pm [59]. Since the photothermal response depends on the absorption of the sample, the force spectrum follows the dissipative part of the material response, resulting in a non-dispersive resonance lineshape.

Thermally modulated van der Waals force

The discussion in this subsection discuss about the thermal expansion that gives rise to a modulation of the tip-sample force in the non-contact zone[60], shown schematically in Figure 2.7(b). Assuming that the force in this zone is described well by the attractive vdW force, the photoinduced thermal expansion force can be obtained from equation (2.7) as:

$$F_{\text{th}}(z) \approx -\frac{H_{\text{eff}} R}{6} \frac{1}{z^3} \Delta L \tag{2.9}$$

where H_{eff} is the effective Hamaker constant between the tip and the sample. In the non-contact zone, this force is referred to as the thermally modulated vdW force F_{vdW} [28, 61].

The thermal expansion of the sample can be split into two parts and written as $\Delta L_{tot}(z) = \Delta L_t(z) + \Delta L_d$. Here ΔL_d is the thermal expansion due to the total illuminated sample

volume, which is independent of the tip-sample distance. The thermal expansion due to the heating right underneath the tip is described by $\Delta L_t(z)$, which relies on the field enhancement in the tip-sample junction and thus depends on the tip-sample distance [28]. For ΔL_d the heated volume is calculated from the beam radius and sample thickness, whereas for $\Delta L_t(z)$ the heated volume is related to the thermal diffusion length l_p of the sample material [28, 60]. For a laser pulse duration of τ_p, the diffusion length is defined as $l_p \sim \sqrt{D\tau_p}$, where D is the thermal diffusivity of the sample [28, 62]. While the direct thermal expansion ΔL_d is linearly proportional to the sample thickness L up to the beam radius, the tip-enhanced thermal expansion reaches a near constant value after a certain sample thickness, which is related to l_p [28].

Besides the thermally modulated vdW force, other mechanisms have been proposed to explain dissipative lineshapes in the PiFM. This includes the thermally induced photo-acoustic force, which would introduce a near constant background on top of other force contributions with steeper distance dependencies [26, 27]. Another mechanism that gives rise to dissipative lineshapes is based on the photo-induced damping principle [27].

2.2.2 Fourier transform Photo-induced Force Microscopy (FT-PiFM)

In this section, we introduce the working principle of a frequency domain version of PiFM, namely FT-PiFM. This method is based on direct mode (homodyne) detection of the PiFM signal, where the force is commonly detected at the intensity modulation frequency ω of the incident laser light. Here, ω (rads^{-1}) is the angular frequency that is related to frequency, f(Hz) as $\omega = 2\pi f$. A strong PiFM response is obtained when the modulation frequency is tuned to a mechanical resonance ω_o of the cantilever beam, i.e., $\omega \sim \omega_o$. The effective time resolution of the experiment can be improved by detecting the force also at overtones of the modulation frequency, which can be achieved by tuning the modulation frequency

such that $\omega = \omega_o/n$ where n is the nth overtone frequency of ω. The time-varying periodic force can be written in terms of Fourier coefficients. To describe the force, we first consider the displacement z of the AFM tip, which can generally be described as a driven harmonic oscillator model:

$$m\ddot{z} + b\dot{z} + kz = F_d(t) \tag{2.10}$$

where m, b, k are the effective mass, damping coefficient, and spring constant of the tip-cantilever system, respectively. Because the force $F_d(t)$ that drives the cantilever motion is a time-periodic function, it can be expanded into a Fourier series, as follows

$$F_d(t) = F_0\left[\frac{a_0}{2} + \sum_{m=1}^{\infty}\Big[a_m\cos(m\omega t) + b_m\sin(m\omega t)\Big]\right] \tag{2.11}$$

with the Fourier coefficients

$$a_m = \int_0^{2\pi/\omega} F_d(t)\cos(m\omega t)\,dt \tag{2.12}$$

$$b_m = \int_0^{2\pi/\omega} F_d(t)\sin(m\omega t)\,dt \tag{2.13}$$

It is expected that the driving force can strongly couple to the cantilever when a specific nth frequency component coincides with the cantilever's resonance frequency (ω_0), i.e., $\omega_0 = n\omega$. Under these conditions, only the nth component couples to the cantilever motion, whereas other components ($m \neq n$) are off-resonant and cannot affect the cantilever motion. The various n-components of the force can be tuned into resonance one-by-one by changing the driving frequency ω and fulfilling the condition $\omega = \omega_0/n$. We can then rewrite the Fourier

coefficients as

$$a_n = \int_0^{2n\pi/\omega_0} F_d(t)\cos(\omega_0 t)\,dt \tag{2.14}$$

$$b_n = \int_0^{2n\pi/\omega_0} F_d(t)\sin(\omega_0 t)\,dt \tag{2.15}$$

where n labels the specific Fourier coefficient of interest that is tuned into resonance with the cantilever. With these definitions, we can rewrite the driving force and substitute the resulting expression into the equation of motion

$$m\ddot{z} + b\dot{z} + kz = R_n\cos(\omega_o t - \theta_n) \tag{2.16}$$

where the amplitude of the time-dependent force is

$$R_n = F_0\sqrt{a_n^2 + b_n^2} \tag{2.17}$$

and its phase is

$$\theta_n = \tan^{-1}\left(\frac{b_n}{a_n}\right) \tag{2.18}$$

It is evident that the amplitude and phase of the force are fully defined by the Fourier coefficients of the chosen nth order through eqs 2.16, 2.17 and 2.18. By measuring the amplitude and phase of the force acting on the cantilever for different n, it is possible to retrieve the Fourier coefficients and, using this frequency domain information, reconstruct the time evolution of the force through eq 2.11. In principle, such a procedure would require knowledge of the coefficients of all m orders. However, by using a priori knowledge of the force evolution, such as an assumed exponential decay, it is possible to retrieve dynamic force parameters with only a few Fourier coefficients namely $n = 1$ and $n = 2$ [39]. For example in PiFM, the laser light is amplitude modulated with a square wave, producing a photoinduced

force that is periodically modulated. The modulated force can be summarized as

$$F(t) = F_{\mathrm{em}}(t) + F_{\mathrm{th}}(t) + F_{\mathrm{vdW}}(t) \tag{2.19}$$

where $F_{\mathrm{em}}(t)$ is the electromagnetic force, $F_{\mathrm{th}}(t)$ is the thermal expansion force, and $F_{\mathrm{vdW}}(t)$ is the thermally modulated van der Waals force. The electromagnetic force follows the modulated laser light instantaneously and thus does not contribute to the measured force during the interval when the light is switched off. The thermal expansion force displays relaxation dynamics during the off interval, but its contribution is expected to be negligible when operating in the noncontact or soft-contact tapping mode. We may, however, expect a strong contribution from F_{vdW} during the off interval due to the relaxation of the material expansion, which is characterized by the cooling time τ_c. We may approximate the modulated force as:

$$F(t) = \begin{cases} F_{\mathrm{vdW}}\, e^{-\frac{t}{\tau_c}} & 0 < t < \frac{T}{2} \\ F_{\mathrm{vdW}}\, (1 - e^{-\frac{(t-\frac{T}{2})}{\tau_h}}) & \frac{T}{2} < t < T \end{cases} \tag{2.20}$$

where τ_h is the characteristic time for the heat-induced expansion of the sample material. In the case of PiFM, the heating and subsequent cooling of the sample do not necessarily display the same dynamics.

Having defined the functional form for the time-periodic force, the Fourier coefficients defined in eqs 2.14 and 2.15 can be rewritten as

$$a_n = \frac{F_{\mathrm{vdW}}\omega_0}{n\pi}[f(\tau_c) \pm f(\tau_h)] \tag{2.21}$$

$$b_n = \frac{F_{\mathrm{vdW}}\omega_0^2}{n\pi}\left[-\frac{1 \pm 1}{\omega_0^2} + \tau_c f(\tau_c) \pm \tau_h f(\tau_h)\right] \tag{2.22}$$

where the function f is defined as

$$f(\tau) = \frac{\tau(1 \pm e^{-\frac{n\pi}{\tau\omega_0}})}{1 + \tau^2\omega_0^2} \tag{2.23}$$

In eqs 2.21-2.23, the plus-minus sign is designated as plus (minus) when n is an odd (even) number. The two unknowns of interest are τ_h and τ_c. From the PiFM measurement, the amplitude R_n and phase θ_n can be retrieved, allowing determination of the values for a_n and b_n. This allows us to write τ_h and τ_c in terms of experimentally accessible values. For this purpose, we define two new variables, namely

$$R_{12} = \frac{R_2}{R_1} \tag{2.24}$$

and

$$\theta_{12} = \theta_1 - \theta_2 \tag{2.25}$$

To obtain analytical expressions, we may further use the approximation , $e^{-\frac{n\pi}{\tau\omega_0}} \sim 0$ which is reasonable when $T/2 >> \tau$. With this approximation, we can write expressions for τ_c in terms of either R_{12} or θ_{12}, and the same for τ_h. By equating the resulting expressions, i.e., $\tau_c(\mathrm{R}_{12}, \tau_h) = \tau_c(\theta_{12}, \tau_h)$, we can find the function τ_h in terms of of R_{12} and θ_{12} as

$$\tau_h = \frac{\pm 2R_{12} + |\cos(\theta_{12})|}{\omega_0 |\sin(\theta_{12})|} \tag{2.26}$$

where the plus sign is used when $\theta_{12} > 0$, and the minus sign is used when $\theta_{12} < 0$. We may use a similar procedure to retrieve τ_c, which yields

$$\tau_c = \frac{2}{\omega_0 |\tan(\theta_{12})|} - \tau_h \tag{2.27}$$

To determine τ_h and τ_c, R_{12} and θ_{12} are measured experimentally. For this purpose, while the cantilever motion is detected at f_0, the laser light is sequentially modulated at $f = f_0$ to determine R_1, θ_1 and at $f = f_0/2$ to obtain R_2, θ_2. Such technique would be useful primarily in determining the presence of a photoinduced force after switching off the laser illumination to ascertain the manifestation of thermal relaxation dynamics.

2.3 Summary

In this Chapter, we have briefly discussed the working principle of TERS, followed by a discussion on our proposed numerical TERS model. The model is based on FDTD and provides a clear distinction between the near-field and far-field enhancement process in regular Raman as well as in TERS. This model forms the basis of the analysis of tip designs that are optimized for TERS, as presented in Chapter 3. Since the topics discussed in Chapters 4 and 5 are directly related to PiFM, we have introduced the operating principle of PiFM and discussed the major origins of the photo-induced force in PiFM measurements, highlighting the electromagnetic and thermal contributions. Finally, we have presented a recent development in PiFM, called FT-PiFM, which enables the measurement of force dynamics on the μs time scale. We use the FT-PiFM method for our studies on nanoprobe expansion dynamics discussed in Chapter 5.

Chapter 3

Optimizing Far-field and Near-field Properties of TERS Nanoprobes

The nanoprobe/tip plays a central role in TERS, as the structure and dimensions of the tip apex determine both the spatial resolution as well as the enhancement needed to lift the weak Raman signal above the noise. Not surprisingly, much work in the TERS field has been devoted to optimizing tip designs and fabrication protocols, including metal cones [63, 64], metal coated dielectric cones [65], a probe terminated with a single metal nanoparticle [66, 67], and optical nanoantennas [68]. In addition, to enable better coupling between the incident field and the near-field, tips have been decorated with gratings [63, 69, 70]. In most studies, the design emphasis for TERS tips has been on optimizing the enhancement of the local electric field. Whereas optimizing the electric field enhancement factor ($EF = |\mathbf{E}_{\mathrm{loc}}|/|\mathbf{E}_{\mathrm{inc}}|$) is indeed important for improving the light-matter interaction in the *near-field*, another important aspect is the optimization of the *far-field* radiative properties of the tip-antenna system. Fine-tuning of the far-field radiation efficiency and radiation direction of the tip-antenna can boost the detected signal significantly. However, comparatively little work has focused on the far-field radiative qualities of metal tips used in TERS.

Previous work has shown that modifications of the tip for improving the coupling between the near-field and the far-field in a desired direction can improve the magnitude of the detected TERS signal notably. In particular, metal tips with periodic horizontal cuts in locations away from the apex have been shown to alter the radiation profile markedly, exhibiting highly directional radiation at angles of 11.6^o [50, 71]. Such directional signals would greatly improve the collection efficiency in practical TERS experiments. To fabricate tips with horizontal grooves, focused ion beam (FIB) milling is the preferred method [16, 63, 72]. The proposed design demands ion bombardment while the tip is carefully rotated, a rather difficult procedure that is time consuming. Such fabrication challenges have prevented the actual implementation of tip designs with enhanced far-field radiation properties.

In this chapter, we propose an alternative design of a decorated metal tip, with an emphasis on feasibility of fabrication with FIB milling. Our design is based on gold tips with vertical grooves, a design strategy that has been used before in scan-probe microscopy and that is compatible with FIB capabilities [73, 74]. We study both the near-field enhancement and the far-field radiative properties of such tips in detail through our FDTD model as outlined in section 2.1.1. To recall, we define the total intensity enhancement ($I_{\text{enh}} = I_{\text{tot}}^{\text{tip}}/I_{\text{tot}}^{\text{no tip}}$) as $I_{\text{enh}} = (EF)^4 \times AE$, where EF is the *near-field* enhancement factor, and AE is an effective measure of the antenna's *far-field* radiation efficiency. Finally, We present designs that promise up to an 10-fold increase in detected far-field TERS intensity.

3.1 Sharp tip versus modified tip

The sharp metallic cone is the most commonly used probe in near-field scanning probe microscopy, including in TERS. Electrochemical etching of metal nanowires is a low-cost, simple and widely used method for nanotip preparation [75, 76, 77, 78, 79, 80]. However, due to the presence of a large number of governing parameters, such as the nature and

concentration of the electrolyte and solvent, the applied voltage frequency and amplitude, etching time and immersion depth of the wire, it remains difficult to consistently produce sharp tips with radii well below 50 nm. In this regard, FIB milling of etched tips can greatly improve the tip parameters. In this section, we study the performance of a blunt tip that has been modified with a relatively simple FIB milling procedure to produce a much sharper feature at the tip's apex.

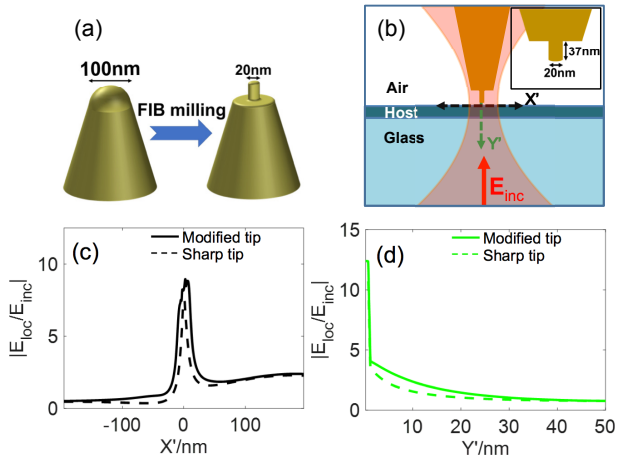

Figure 3.1: (a) Tip modification by FIB milling. (b) Simulation setup for the modified tip. (c) Magnitude of the local electric field enhancement along the dashed horizontal line in panel (b). (d) Magnitude of the local electric field enhancement (green solid curve) along the dashed vertical line in panel (b). The dashed curve in both panel (c) and (d) shows the corresponding values obtained in the last section for a 10 nm radius sharp tip.

Figure 3.1(a) shows the modification of a blunt tip to a pillar-type structure (radius = 10 nm) at the tip's apex, a structure related to one recently reported.[81] The simulation setup is shown schematically in Figure 3.1(b). Our simulations indicate that a feature of height 37 nm gives rise to good enhancement in the near-field as well as favorable far-field radiation characteristics. The magnitude of the local electric field enhancement in the lateral dimension (along black dashed line in panel 3.1(b)) is shown in Figure 3.1(c). It can be seen that the pillar-type tip shows good near-field enhancement that compares well with the performance of the ideal sharp 10 nm radius tip discussed in Figure 2.3, albeit that the lateral resolution is lowered from 6 nm to 19 nm [82, 83]. The field enhancement along the axial coordinate is shown in Figure 3.1(d), revealing performance comparable to the ideal

sharp tip.

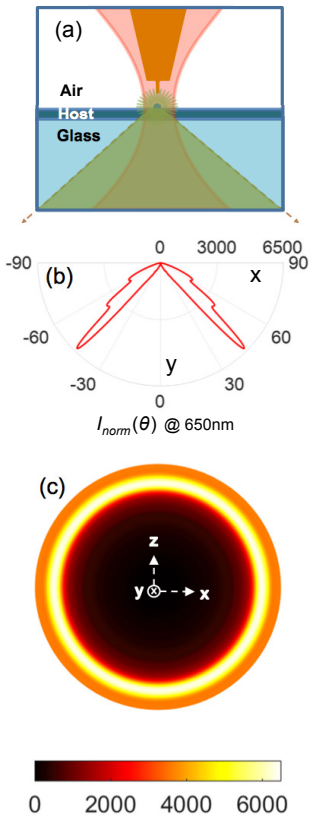

Figure 3.2: (a) Schematic of the simulation setup with the modified tip. (b) Far-field intensity of radiation from the tip-sample junction into the xy-bottom half plane, normalized to the maximum intensity found for a vertical dipole without the tip. (c) Far-field intensity in the back focal plane of the objective.

The far-field radiation pattern of the modified tip is studied in Figure 3.2. Similar to the far-field profile of the sharp tip discussed in Figure 2.4, the modified tip exhibits directional emission at around $\pm 44^o$ with the added benefit of a maximum signal enhancement that approaches $\sim$ 6300 times that of the signal without the tip, as shown in panel 3.2(b). We find that $AE = 1.33$ for the modified tip with a near-field enhancement $EF = 8.2$. Similar to the radiation pattern of the sharp tip, the pillar-type tip shows azimuthal symmetry in the back focal plane. It should be noted that relative to the ideal sharp tip, the modified tip shows reduced performance at wavelengths over $\sim$ 700 nm with lower relative AE factors. In addition, the formation of ridges and imperfect pillars can affect its performance[84]. Nonetheless, these results show that relatively simple FIB sculpting of blunt tips can result

in tip performance that approaches that of ideal conical tips.

3.2 Enhanced directional radiation with vertical grooves at the tip apex

The improved tip performance obtained through FIB-milling of a relatively simple structure suggest that additional improvements in the antenna's radiation properties can be achieved with more advanced designs. Here we explore a design that is based on the same structure discussed in the previous Section with additional patterning away from the apex. After rigorous tuning of the simulation parameters, we find excellent performance with a design that includes vertical grooves on the shaft. This design exhibits four identical grooves of height 170 nm and depth 50 nm with a horizontal spacing between the two grooves of 70 nm, as shown in Figure 3.3(a).

Previous work on FIB-based tip modification includes introducing horizontal grooving around the tip surface at locations that are comparatively far away from the tip apex [50, 63, 71, 72, 85]. Applying horizontal symmetric grooves azimuthally around the tip's shaft requires FIB milling in a number of steps with precise mechanical rotation, shown schematically in Figure 3.3(b). A simpler fabrication procedure is obtained for the proposed vertical grooves, which would require a single scanning pattern that obviates mechanical rotation, as illustrated in Figure 3.3(c). Note that the design resolution is well above the practical resolution ($\sim$ 20 nm) of most FIB-SEM tools [86]. Previous studies have demonstrated successful fabrication of similar vertical groves on nanotips [73, 74]. We note that the ridges (rather than a perfect staircase) in our design are intentional, as discussed below.

Figure 3.4(a) shows the schematic for simulating the near-field distribution in the vicinity of the grooved tip. Figure 3.4(b) and (c) show the magnitude of the total, the x-component and

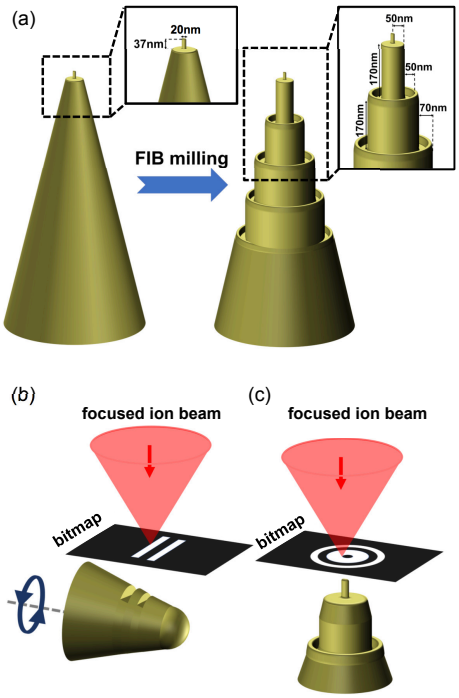

Figure 3.3: (a) 3D Schematic of the proposed vertically grooved tip. (b) Simplified diagram showing the process for making a horizontal cylindrical cut on the tip surface by FIB milling, requiring mechanical rotation for symmetrical pattern. (c) Simplified diagram showing the process for making a vertical cylindrical cut around the tip apex by FIB milling with no requirement for sample rotation.

the y-component of the local electric field enhancement, as measured along the dashed lines in panel (a). The maximum field enhancement reaches ~ 15 at the substrate surface, which is 2 times and 1.7 times better than for the ideal 10 nm radius tip and the pillar-type tip, respectively. The lateral and axial FWHM are comparable to the performance of the pillar-type tip. Figures 3.4(b) and (c) underline that the vertical field component is the dominant contributor to the local field enhancement. These simulations show that the proposed tip exhibits excellent near-field enhancement properties for TERS measurements.

The far-field response of the vertically grooved tip is shown in Figure 3.5. Figure 3.5(b) and (c) show the far field intensity patterns in the bottom-half xy-plane at the wavelengths 650 nm and 700 nm. We find an almost 4 times increase in $I_{norm}(\pm 44^o)$ compared to the pillar-type tip. In addition to the directional radiation at $\pm 44^o$, we observe the appearance of significant inner lobes at $\pm 17.3^o$. For the vertically grooved tip we find $AE = 0.65$. The

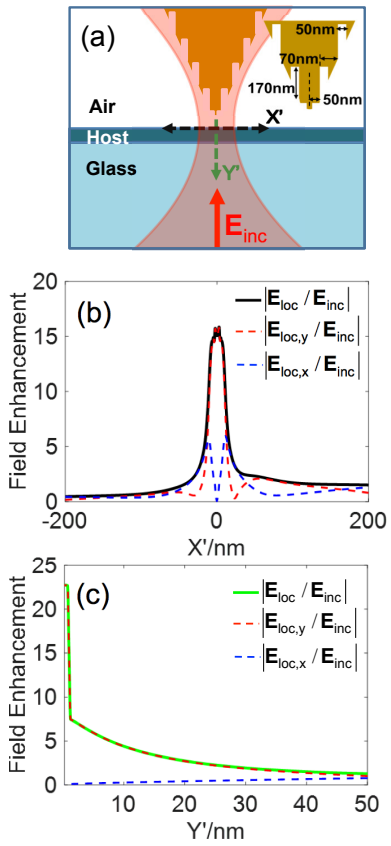

Figure 3.4: (a) Schematic of the simulation setup with the vertically grooved tip. (b) Magnitude of the total (black solid curve), x-component (blue dashed) and y-component (red dashed) of the local electric field enhancement. (c) Magnitude of the total (green solid curve), x-component (blue dashed) and y-component (red dashed) of the local electric field enhancement. Profiles in (b) and (c) are measured along the black and green dashed lines in (a).

smaller AE value suggests a measured intensity that is less than what would be expected based on the $(EF)^4$ factor. This underlines the approximate nature of the $(EF)^4$ near-field metric [45, 87], which does not take far-field radiative properties of the antenna explicitly into account. For comparison, we also calculate the total relative intensity I_{enh} when detection is carried out at a lower detection angle of $\theta_{\max} = 17.5^o$, which would correspond to a detection NA of 0.3 in air. In this case $AE = 6.58$, implying a significant enhancement of detected signal at smaller detection angles relative to the signal measured with the unmodified tip. This enhancement is a direct consequence of the appearance of the inner lobe for the vertically grooved tip. We also note that the tip's radiation profile shows a marked spectral dependence.

Figure 3.5(c), which shows the radiation profile at 700 nm, reveals that, in addition to an overall decrease in $I_{\text{norm}}(\theta)$, the strength of the $\pm 44^o$ lobes decreases more relative to that of the inner lobes. In addition, the angle of the inner lobe decreases to $\sim \pm 16^o$. We note that for wavelengths shorter than 650 nm, a similar decrease in overall signal strength is observed, although the shape of the radiation profile remains relatively constant as Figure 3.5(b).

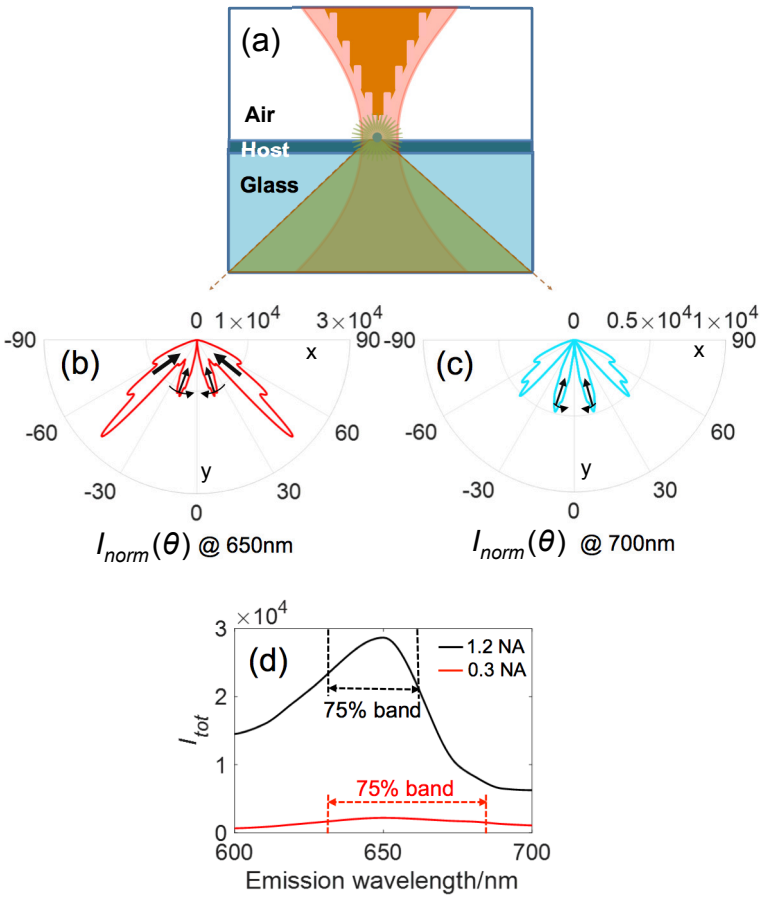

Figure 3.5: (a) Schematic of the simulation of the far-field radiation by a dipole with the presence of the vertically grooved tip. (b) The normalized far-field intensity in the bottom-half xy-plane at 650 nm. (c) Similar simulation for radiation at 700 nm. The arrows inside the lobes show the relative strength and the pattern of the signal change with wavelength. The curved arrow in the inner lobe shows peak movement. (d) Total intensity I_{tot} captured by a NA = 1.2 oil (black curve) and a NA = 0.3 dry (red curve) objective lens for the wavelength range 600 nm-700 nm. The dotted boundaries in both curves show the wavelength range where the output total intensity stays within 75% of its maximum.

The spectral changes of the radiation profile are reflected in the efficiency of capturing the

radiated Raman signal in the epi-direction. Using the 1.2 NA oil immersion objective, we see that the total I_{tot} traces a spectral profile with a clear maximum at 650 nm, our optimization wavelength. As shown by the black line in Figure 3.5d, the 75% signal mark ranges from 630 nm to 660 nm, emphasizing that a relatively broad spectral range can be intercepted with high efficiency in this detection scheme. When a lower NA lens is used, such as the 0.3 NA dry lens, the lobes at higher angles are not detected, lowering the overall signal, as evidenced by the red line in Figure 3.5d. However, the relative insensitivity of the inner lobes ensures that the spectral dependence of the detection efficiency of the lower NA is less pronounced. The 75% signal mark now spans 630 nm to 680 nm. Despite the lower signal of the 0.3 NA system, the use of the improved tip gives rise to a higher maximum normalized intensity ($\sim 11,500$) compared to the bare 10 nm tip ($\sim 3,700$). Other than slight changes in the local field enhancement [48], the whole system response and operation is expected to be relatively unaffected by the incident wavelength tuning.

3.3 Design details and underlying physics

The periodic structure of the vertically grooved tip shows similarity with the flat "bull's eye" antenna [88]. Each symmetrical circular sub-wavelength groove effectively functions as a magnetic dipole-like point source, which is likely responsible for the directional radiation at angles lower than the critical angle emission for a single emitter.

The ridges around the grooves are an intentional part of the design, as they are likely to appear in the practical fabrication of vertical grooves. These ridges have a favorable effect on the magnitude of the signal. As shown in Figure 3.6(b), a vertically grooved tip produced without any ridges (green) displays a lower signal overall compared to a tip with ridges (red). However, the ridges do not alter the spatial phase of the radiation, as directional radiation is seen at identical angles for both tips. The lower signal for the tip without ridges is related

to a decrease in the value of the local field enhancement as shown in Figure 3.6(c). This indicates that the ridges play a role in coupling energy from the far-field to the near-field region near the tip apex and vice versa.

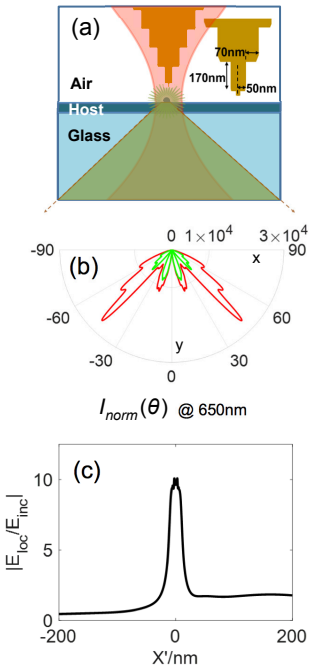

Figure 3.6: (a) Schematic of the simulation model for a vertically grooved tip without ridges. (b) Far-field radiation profile of the tip with (red) and without (green) ridges. (c) Near-field distribution of the vertically grooved tip without ridges.

Note that the vertically grooved tip is specifically designed and optimized for a bottom illumination/detection TERS system. Such vertical grooving is not expected to provide optimum response for side illumination TERS which requires different design criteria to be satisfied [71].

3.4 Total normalized far-field intensity distribution: vertically grooved tip vs sharp tip

Finally, we calculate the distribution of the total detected signal enhancement for different tips and different objective lenses, namely the 1.2 NA oil objective and the 0.3 NA dry objective. In our calculations, symmetry in the azimuthal dimension has been assumed for simplicity, which could provide some overestimation for the off-centered dipole. However, this should not have any impact on the typical performance. The results are shown in Figure 3.7 as a function the lateral position of the molecular dipole.

In Figure 3.7(a), we show the results for an optimized vertically grooved tip when the signal is detected with the 1.2 NA oil objective lens. The results are compared with the signals observed for the unmodified 10 nm radius tip shown in Figure 3.7(b). The total far-field intensity enhancement is indicated in red and the TERS enhancement factor $(EF)^4$ is shown in blue. The plots reveal that the modified tip shows an increase in total intensity enhancement I_{enh}, namely the TERS signal enhancement by 10 times relative to the ideal sharp tip. The I_{enh} follows the general trend of $(EF)^4$ and the apparent difference in value between can be understood as the antenna efficiency factor AE.

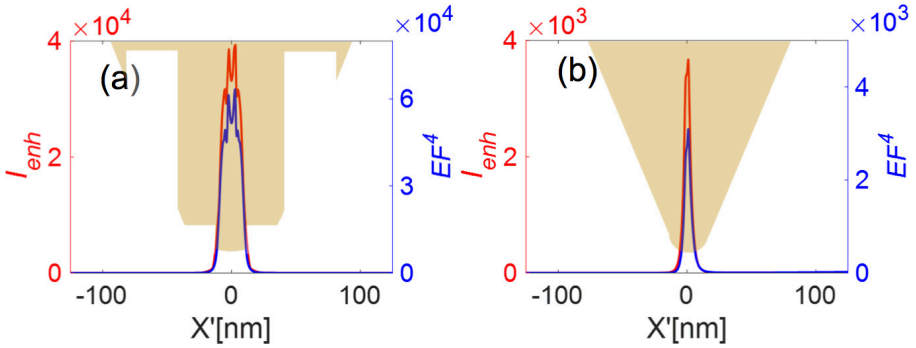

Figure 3.7: Total far-field intensity captured through a high NA 1.2 oil immersion objective lens for a dipole positioned under (a) the proposed vertically grooved tip and (b) under 10 nm sharp tip. The intensity is plotted as a function of the dipole's lateral distance from the tip apex (red solid curve, left axis). The blue solid curve in each figure shows the $(EF)^4$ factor (right axis).

The lateral dependence of the signal in panel 3.7(a) resembles a Gaussian like-shape that is centered around the tip's apex and exhibits a FWHM of 17 nm. This implies that the tip is mostly effective in radiating signal that originates from molecules within a 8.5 nm radius from the center of the tip apex, i.e. molecules father away do not contribute to the signal. The FWHM for the 10 nm sharp tip is more confined, at the expense of weaker signals, as shown in panel (b). For detection at detection angles below $\theta = \pm 44^o$, the signal is expected to be much weaker. Nonetheless, for the vertically grooved tip, radiation intensity is found in the inner lobes as well, a feature that is absent for the ideal sharp tip. For instance, when detecting with a detection cone afforded by a 0.3 NA lens, we find a total enhancement of $I_{\text{enh}} \sim 3 \times 10^5$ for a dipole under the vertically grooved tip. For comparison, the enhancement under the same conditions for the 10 nm sharp tip is $I_{\text{enh}} \sim 2 \times 10^3$. Consequently, the relative detection efficiency (intensity) with the 0.3 NA lens is dramatically improved by a relative factor of 150 for the modified tip relative to the ideal sharp tip. This translates into a 150 times stronger TERS signal when the modified tip is used.

3.5 Summary

In this chapter, we have proposed a set of realistic modifications to gold tips to improve the magnitude of the signal detected in a bottom-illuminated TERS microscope. Other than focusing solely on the near-field enhancement, we have performed simulations that seek to improve the overall far-field signal from the tip-sample system. Through detailed FDTD simulations we have found that relatively simple modifications to the metal tip can produce marked changes in the far-field radiation from the tip antenna. In particular, using feasible FIB procedures, a blunt tip can be converted into a pillar-type tip that exhibits excellent near-field enhancement of $EF = 8.2$ as well as an antenna efficiency of $AE = 1.33$ when a 1.2 NA oil immersion lens is used for excitation and detection. These properties can be further

improved by applying vertical grooves through FIB milling. The application of four periodic grooves in the shaft results in a higher near-field enhancement of $EF = 15$. Relative to an ideal (unmodified) tip of 10 nm radius, the vertically grooved tips studied here produce ~ 10 fold stronger TERS signals at the detector when a high numerical aperture lens is used. This antenna system also redirect a portion of the signal into smaller angles, which facilitates signal collection when a lower NA lens is used. For instance, for detection angles that coincide with that of a 0.3 NA lens, we find an antenna efficiency factor of $AE = 6.58$. This work shows that a significant increase in the detected TERS signal can be attained through optimization of both the near-field enhancement and far-field radiative properties of the tip. We have paid special attention to the feasibility of fabricating improved tips with FIB. We expect that the designs presented in this work can be realistically fabricated, starting from blunt $r \sim 50$ nm tips that are regularly produced through chemical tip etching. These procedures are expected to be reproducible and may thus contribute to a more routine implementation of TERS.

Chapter 4

Photo-induced Forces on Chiral Nanoprobes

Light-matter interactions are commonly dominated by the material's response to the electric component of the electromagnetic field. In most PiFM experiments, the detected force is also dominated by the electric field. This has allowed detailed PiFM mapping of electric field distributions of focused Gaussian [30, 31] as well as vector beams [29] through the optical force exerted on it. However, under certain conditions, forces related to the tip's interaction with the magnetic component of light can also become important. For instance, the use of a especially designed silicon nanoprobe has made it possible to generate PiFM maps of the magnetic field distribution of focused vector beams [32]. Magnetic fields also play a role of the detected force is sensitive to the chirality of the electromagnetic field. In this Chapter, we show that by imposing a chiral feature on a regular achiral nanoprobe, a conventional PiFM measurement can bring out the chiral properties of the incident beam, a property known as the *helicity density* [89].

Light can exist in a chiral state that is related to the curled character of the electric and

magnetic fields. The quantity commonly used for quantifying this 'degree of curliness' is the time-averaged helicity density [90, 91, 92], which is defined as $h = \frac{1}{2\omega c}\mathrm{Im}(\mathbf{E} \cdot \mathbf{H}^*)$, where $\mathbf{E}$ and $\mathbf{H}$ are the phasor electric and magnetic field at angular frequency ω, and c is the speed of light (* denotes complex conjugation) [93, 94]. The helicity density is a time-even, pseudo-scalar conserved quantity and the flux of the helicity density, i.e. the chiral momentum density, is related to the spin angular momentum of the beam [90, 95]. The latter quantity is a time-odd, pseudo-vector quantity [91] and its density is defined as $\boldsymbol{\sigma} = -\frac{\varepsilon_0}{4\omega i}(\mathbf{E} \times \mathbf{E}^*) - \frac{\mu_0}{4\omega i}(\mathbf{H} \times \mathbf{H}^*)$, where ε_0 and μ_0 are the absolute permittivity and permeability of free space [91, 96], respectively. Although both quantities describe angular momentum associated with the polarization state of light [90], only the time-averaged helicity density is classified as a conserved property of the electromagnetic field [97, 98], and, therefore, considered to be the proper descriptor of optical chirality.

The chiral property of light makes it possible to study chiral objects, such as molecules and nanostructures, in an optical manner [98, 99, 100, 101, 102, 103]. In common applications, the specimen is illuminated sequentially with left-handed and right-handed circularly polarized light (LCP and RCP), and the chiral information is inferred from the differential response of the material. The chiral state of circularly polarized light is well understood, which facilitates the analysis of such measurements. However, performing similar measurements at dimensions beyond the diffraction limit can be challenging [92, 104, 105], because the chiral state of light in the near zone cannot always be assessed with far-field measurements. Now, the question arises whether a quantity like the helicity density can be properly measured at dimensions beyond the diffraction limit of light. Although near-field and scanning nanoparticle methods have been used to probe the electric and magnetic components of vector fields at sub-diffraction limited resolution [32, 106, 107, 108, 109], a direct measurement of the helicity density in the near-field of tightly focused laser fields has so far remained out of reach.

In this chapter, we theoretically investigate the connection between the photo-induced forces felt by a chiral tip under differential RCP/LCP illumination and the chiral state of light at the nanoscale. Using image dipole theory, we have found a direct relation between the measured differential force and the chiral properties of the incident electromagnetic field in terms of the time-averaged helicity density and spin-angular momentum density. The $\exp(-i\omega t)$ time notation is implicitly assumed in analysis throughout the chapter. We further model the chiral tip as an isotropic chiral sphere to examine several design considerations and validate our dipole model with full-wave, finite element method (FEM) simulations. Finally, we present force map of helcity density of chiral beams and finish with a discussion on the error tolerance of the proposed technique due to beam imperfection.

4.1 Theoretical Analysis

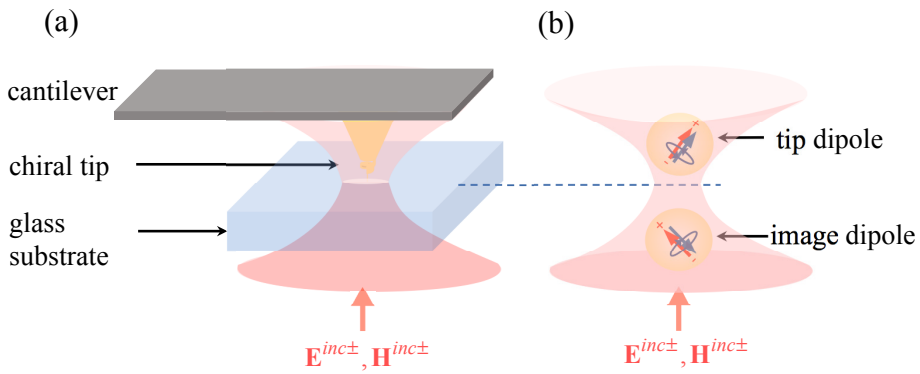

Figure 4.1: (a) Schematic of the PiFM system with a chiral tip with illumination from the bottom. (b) Photo-induced chiral tip dipole and image dipole according to image dipole theory.

In this section, we determine the mechanical force that acts on the chiral tip due to the presence of the electromagnetic field, as shown schematically in Figure 4.1(a). We can model the tip as particle and write the time-averaged force exerted on this particle as [23, 25]

$$\langle \mathbf{F} \rangle = \frac{1}{2}\mathrm{Re}\Big\{ \int_S \Big[\varepsilon(\mathbf{E}\cdot\hat{\mathbf{n}})\mathbf{E}^* + \mu^{-1}(\mathbf{B}\cdot\hat{\mathbf{n}})\mathbf{B}^* - \frac{1}{2}\left(\varepsilon|\mathbf{E}|^2 + \mu^{-1}|\mathbf{B}|^2\right)\hat{\mathbf{n}} \Big]\, dS \Big\} \tag{4.1}$$

where the integration is over the arbitrary surface S that encloses the tip-particle of volume V, $\hat{\mathbf{n}}$ is the unit vector normal to this surface, and $\mathbf{E}$ and $\mathbf{B}$ are the phasors of the total electric field and magnetic flux density, which include both the incident light and the scattered light contributions. It is assumed that the particle is embedded in a non-dissipative medium with permittivity ε and permeability μ. To simplify this expression, we next assume that the tip can be described as a dipolar particle with an electric and magnetic dipole moment in free space, written as $\mathbf{p}_{tip}$ (Cm) and $\mathbf{m}_{tip}$ (Am^2), respectively. The phasors of the dipole moments are defined as $\mathbf{p}_{tip} = \int \mathbf{r}\rho(\mathbf{r})dV$ and $\mathbf{m}_{tip} = \frac{1}{2}\int[\mathbf{r} \times \mathbf{J}(\mathbf{r})]dV$, where $\rho(\mathbf{r})$ and $\mathbf{J}(\mathbf{r})$ are the induced charge and current densities in the particle. Assuming the tip-particle's response is dominated by its electric and magnetic dipole moments, the expression for the time-averaged electromagnetic force reduces to [110, 111]

$$\langle \mathbf{F} \rangle = \frac{1}{2}\mathrm{Re}\Big\{ \big(\nabla \mathbf{E}^{loc}(\mathbf{r}_{tip})\big)^* \cdot \mathbf{p}_{tip} + \big(\nabla \mathbf{H}^{loc}(\mathbf{r}_{tip})\big)^* \cdot \mu_0 \mathbf{m}_{tip} - \frac{c\mu_0 k^4}{6\pi}(\mathbf{p}_{tip} \times \mathbf{m}^*_{tip}) \Big\} \quad (4.2)$$

where $\mathbf{E}^{loc}(\mathbf{r}_{tip})$ and $\mathbf{H}^{loc}(\mathbf{r}_{tip})$ are the local electric and magnetic field at the tip dipole position. Here, $\nabla\mathbf{E}$ and $\nabla\mathbf{H}$ are the gradient of electric and magnetic field vectors. This is of dyadic form and defined as $\nabla\mathbf{E} = \sum_i \sum_j \frac{\partial E_j}{\partial x_i}\hat{x_i}\hat{x_j}$ where i and j stands for x, y and z components of cartesian coordinates [112]. Note that sometimes in the literature the μ_0 factor in the second and third term of equation (4.2) is included in the definition of the magnetic dipole moment ($\mathbf{m}_{tip}$) [113, 114, 115]. The notation used here is the same as that in Refs. [33, 105, 92, 94, 32]. The time-averaged force has three distinct contributions: the first term on the right hand side of equation (4.2) is recognized as the electric dipolar force $\langle \mathbf{F}_e \rangle$, the second term is known as the magnetic dipolar force $\langle \mathbf{F}_m \rangle$, and the last term is called the interaction force $\langle \mathbf{F}_{int} \rangle$.

To calculate the force, we require expressions for the induced electric and magnetic dipole moments. Assuming that the tip is an isotropic and reciprocal chiral object, the dipole

moments can be related to the local fields through polarizabilities as [116]

$$\mathbf{p}_{tip} = \alpha_{ee}\mathbf{E}^{loc}(\mathbf{r}_{tip}) + \alpha_{em}\mathbf{H}^{loc}(\mathbf{r}_{tip}) \tag{4.3}$$

$$\mathbf{m}_{tip} = -\mu_0^{-1}\alpha_{em}\mathbf{E}^{loc}(\mathbf{r}_{tip}) + \alpha_{mm}\mathbf{H}^{loc}(\mathbf{r}_{tip}) \tag{4.4}$$

where α_{ee}, α_{mm} and α_{em} are the electric, magnetic and electro-magnetic polarizabilities, respectively. We have considered that $\alpha_{me} = -\mu_0^{-1}\alpha_{em}$ because of reciprocity. The local fields at the tip dipole position can be obtained from image dipole theory [20, 23, 117]. We model the effect of the substrate by substituting the substrate response by the image of the photo-induced (chiral) dipole in the tip, written as $\mathbf{p}_{img}$ and $\mathbf{m}_{img}$ and shown in Figure 4.1(b). The local electric and magnetic fields at the tip position can then be expressed as

$$\mathbf{E}^{loc}(\mathbf{r}_{tip}) = \mathbf{E}^{inc}(\mathbf{r}_{tip}) + \mathbf{E}^{sca}_{img\to tip}(\mathbf{r}_{tip}) \tag{4.5}$$

$$\mathbf{H}^{loc}(\mathbf{r}_{tip}) = \mathbf{H}^{inc}(\mathbf{r}_{tip}) + \mathbf{H}^{sca}_{img\to tip}(\mathbf{r}_{tip}) \tag{4.6}$$

where $\mathbf{E}^{inc}(\mathbf{r}_{tip})$, $\mathbf{H}^{inc}(\mathbf{r}_{tip})$ are the incident electric and magnetic field at the tip dipole location, and $\mathbf{E}^{sca}_{img\to tip}(\mathbf{r}_{tip})$, $\mathbf{H}^{sca}_{img\to tip}(\mathbf{r}_{tip})$ are the scattered electric and magnetic field by the image dipoles at the tip dipole location.

The scattered fields, which include nearfields, are defined through the image dipole moments and their Green's functions as [23, 117]

$$\mathbf{E}^{sca}_{img\to tip}(\mathbf{r}_{tip}) = \underline{\mathbf{G}}^{ee}(\mathbf{r}_{tip} - \mathbf{r}_{img}) \cdot \mathbf{p}_{img} + \underline{\mathbf{G}}^{em}(\mathbf{r}_{tip} - \mathbf{r}_{img}) \cdot \mathbf{m}_{img} \tag{4.7}$$

$$\mathbf{H}^{sca}_{img\to tip}(\mathbf{r}_{tip}) = \underline{\mathbf{G}}^{me}(\mathbf{r}_{tip} - \mathbf{r}_{img}) \cdot \mathbf{p}_{img} + \underline{\mathbf{G}}^{mm}(\mathbf{r}_{tip} - \mathbf{r}_{img}) \cdot \mathbf{m}_{img} \tag{4.8}$$

where $\underline{\mathbf{G}}(\mathbf{r}) = G_x\hat{\mathbf{x}}\hat{\mathbf{x}} + G_y\hat{\mathbf{y}}\hat{\mathbf{y}} + G_z\hat{\mathbf{z}}\hat{\mathbf{z}}$ is the dyadic Green's function in Cartesian coordinates. The Green's functions that appear in equations (4.7) and (4.8) are approximated in the

nearfield as [118]

$$\underline{\mathbf{G}}^{ee}(\mathbf{r}) = \frac{1}{4\pi\varepsilon_0|\mathbf{r}|^3}(3\hat{\mathbf{r}}\hat{\mathbf{r}} - \underline{\mathbf{I}}) \tag{4.9}$$

$$\underline{\mathbf{G}}^{mm}(\mathbf{r}) = \frac{1}{4\pi|\mathbf{r}|^3}(3\hat{\mathbf{r}}\hat{\mathbf{r}} - \underline{\mathbf{I}}) \tag{4.10}$$

$$\underline{\mathbf{G}}^{em}(\mathbf{r}) = -\frac{1}{i\omega\varepsilon_0}\nabla \times \underline{\mathbf{G}}^{mm}(\mathbf{r}) \tag{4.11}$$

$$\underline{\mathbf{G}}^{me}(\mathbf{r}) = \frac{1}{i\omega\mu_0}\nabla \times \underline{\mathbf{G}}^{ee}(\mathbf{r}) \tag{4.12}$$

where $\underline{\mathbf{I}}$ is unit dyad (tensor) and $\hat{\mathbf{r}}$ is the unit vector from the source point to the point of observation.

In the same fashion, we can also define the image dipole moments and the local fields at the image location. Our goal is to obtain self-consistent approximate expressions for the local fields at the tip location and for the dipole moments in terms of the incident light components. To achieve this, consistent with the nearfield approximation of the Green's function, we first ignore any phase retardation effects in the fields between the tip and image dipole position. Second, we will only consider terms in the polarizability up to second order (full derivation is provided in Appendix A). With these assumptions, we may use equations (4.3)-(4.6) to determine the longitudinal (z) component of the time-averaged force in the

dipole approximation as written as

$$
\begin{aligned}
\langle F_{z,grad}\rangle &= \langle F_{z,e}\rangle + \langle F_{z,m}\rangle \\
&= \frac{3}{2\pi|z|^4}\left[\frac{1}{2}\Big(-\frac{|\alpha_{ee}|^2}{\varepsilon_0}+\mu_0|\mu_0^{-1}\alpha_{em}|^2\Big)(\tfrac{1}{2}|\mathbf{E}_\parallel^{inc}|^2+|\mathbf{E}_z^{inc}|^2)\right. \\
&\qquad +\frac{1}{2}\Big(-\frac{|\alpha_{em}|^2}{\varepsilon_0}+\mu_0|\alpha_{mm}|^2\Big)(\tfrac{1}{2}|\mathbf{H}_\parallel^{inc}|^2+|\mathbf{H}_z^{inc}|^2) \\
&\qquad \left.-\mathrm{Re}\Big\{\Big(\frac{\alpha_{ee}\alpha_{em}^*}{\varepsilon_0}+\alpha_{mm}^*\alpha_{em}\Big)(\tfrac{1}{2}\mathbf{E}_\parallel^{inc}\cdot\mathbf{H}_\parallel^{inc*}+\mathbf{E}_z^{inc}\cdot\mathbf{H}_z^{inc*})\Big\}\right] \\
&\quad +\frac{6\omega}{\pi k^2|z|^5}\left[2\omega\mathrm{Re}\Big\{\frac{\alpha_{ee}\alpha_{em}^*}{\varepsilon_0}\Big\}[\boldsymbol{\sigma}_E^{inc}]_z-2\omega\mathrm{Re}\big\{\alpha_{em}\alpha_{mm}^*\big\}[\boldsymbol{\sigma}_H^{inc}]_z\right. \\
&\qquad \left.-2\mathrm{Im}\Big\{(|\alpha_{em}|^2-\mu_0\alpha_{ee}\alpha_{mm}^*)[\mathbf{S}^{inc}]_z\Big\}\right]
\end{aligned}
\tag{4.13}
$$

$$
\begin{aligned}
\langle F_{z,int}\rangle = \; & -\frac{ck^4}{12\pi}\left[\mathrm{Re}\Big\{-\alpha_{em}^*\alpha_{ee}\Big\}\mathrm{Re}\Big\{[\mathbf{E}_\parallel^{inc}\times\mathbf{E}_\parallel^{inc*}]_z\Big\}\right. \\
& +\mathrm{Re}\Big\{\mu_0\alpha_{mm}^*\alpha_{em}\Big\}\mathrm{Re}\Big\{[\mathbf{H}_\parallel^{inc}\times\mathbf{H}_\parallel^{inc*}]_z\Big\} \\
& +4\omega\mathrm{Im}\Big\{-\frac{\alpha_{em}^*\alpha_{ee}}{\varepsilon_0}\Big\}[\boldsymbol{\sigma}_E^{inc}]_z+4\omega\mathrm{Im}\Big\{-\alpha_{mm}^*\alpha_{em}\Big\}[\boldsymbol{\sigma}_H^{inc}]_z \\
& \left.+2\mathrm{Re}\Big\{\alpha_{em}^*\alpha_{em}[\mathbf{S}^{inc*}]_z\Big\}+2\mathrm{Re}\Big\{\mu_0\alpha_{mm}^*\alpha_{ee}[\mathbf{S}^{inc}]_z\Big\}\right]
\end{aligned}
\tag{4.14}
$$

where $\mathbf{E}_\parallel^{inc}=E_x^{inc}\hat{\mathbf{x}}+E_y^{inc}\hat{\mathbf{y}}$, $\mathbf{H}_\parallel^{inc}=H_x^{inc}\hat{\mathbf{x}}+H_y^{inc}\hat{\mathbf{y}}$ and $\mathbf{E}_z^{inc}=E_z^{inc}\hat{\mathbf{z}}$, $\mathbf{H}_z^{inc}=H_z^{inc}\hat{\mathbf{z}}$ are the transverse and longitudinal components of the incident fields at the tip dipole location, the notation ($\mathbf{r}_{tip}$) has been avoided here for brevity; $\mathbf{S}^{inc}=\frac{1}{2}\mathbf{E}^{inc}\times(\mathbf{H}^{inc})^*$ is the Poynting vector of the incident field; $\boldsymbol{\sigma}_E^{inc}$ and $\boldsymbol{\sigma}_H^{inc}$ are the electric and magnetic parts of the time-averaged total spin angular momentum density of the incident light; and z is the vertical distance between the tip dipole and its image. See the Appendix A for a detailed derivation of equations (4.13) and (4.14).

Equation (4.13) describes the force due to the combined electric and magnetic dipolar response of the tip. This force shows a distance dependence on the tip-sample distance which scales as z^{-4}, similar to the distance dependence of the gradient force that is typically measured in PiFM [23, 31]. The first two lines of equation (4.13) are recognized as the purely electric and purely magnetic dipolar force contributions to the gradient force, whereas the third line describes the force that arises from a nonzero scalar product of the electric and magnetic fields, i.e. the helicity density. In addition, this force also exhibits a z^{-5} distance dependence, expressed in the last two lines of equation (4.13). This part carries information about the longitudinal component of the spin angular momentum density and the Poynting vector of the incident light.

Equation (4.14) accounts for the interaction force, which lacks a direct dependence on the tip-sample distance. In addition to the purely electric and magnetic contributions to the interaction force, described by the first two lines in equation (4.14), the latter two lines add force contributions that scale with the longitudinal component of the spin angular momentum density and with the Poynting vector. Because these latter terms depend on the momentum of the incoming field, the interaction force shows similarity with the scattering force [23, 31] in PiFM.

We are interested in using the force as a way to measure the helicity density h^{inc} of an incident beam. To measure this quantity, we will use a second incident beam that is similar to the original beam but is of opposite handedness. Hence, if we define the helicity density of the original beam as $h^{inc} = h^{inc+}$, then the helicity density of the auxiliary beam is given as h^{inc-}. For this purpose, we assume two states for the incident light, indicated by $\mathbf{E}^{inc+}$, $\mathbf{H}^{inc+}$ and $\mathbf{E}^{inc-}$, $\mathbf{H}^{inc-}$, describing the input fields of different handedness. The two illumination states have the same energy densities, $|\mathbf{E}^{inc+}|^2 = |\mathbf{E}^{inc-}|^2$ and $|\mathbf{H}^{inc+}|^2 = |\mathbf{H}^{inc-}|^2$, but exhibit opposite helicity densities, $\mathrm{Im}(\mathbf{E}^{inc+} \cdot \mathbf{H}^{inc+*}) = -\mathrm{Im}(\mathbf{E}^{inc-} \cdot \mathbf{H}^{inc-*})$, i.e. $h^{inc+} = -h^{inc-}$. Note that the longitudinal spin angular momentum density components are

related as $[\boldsymbol{\sigma}_E^{inc+}]_z = -[\boldsymbol{\sigma}_E^{inc-}]_z$ and $[\boldsymbol{\sigma}_H^{inc+}]_z = -[\boldsymbol{\sigma}_H^{inc-}]_z$. We also find that $\mathbf{S}^{inc+} = \mathbf{S}^{inc-}$, and that the following relations hold

$$\begin{aligned} \mathrm{Re}\Big\{[\mathbf{E}_\parallel^{inc+} \times \mathbf{E}_\parallel^{inc+*}]_z\Big\} &= \mathrm{Re}\Big\{[\mathbf{E}_\parallel^{inc-} \times \mathbf{E}_\parallel^{inc-*}]_z\Big\} \\ \mathrm{Re}\Big\{[\mathbf{H}_\parallel^{inc+} \times \mathbf{H}_\parallel^{inc+*}]_z\Big\} &= \mathrm{Re}\Big\{[\mathbf{H}_\parallel^{inc-} \times \mathbf{H}_\parallel^{inc-*}]_z\Big\} \end{aligned} \tag{4.15}$$

We next determine the differential force, obtained by measuring the force under illumination with incident light of (+) and (−) handedness, and taking the difference. Under these conditions, the differential gradient force $\Delta\langle F_{z,grad}\rangle = \langle F_{z,grad}\rangle^+ - \langle F_{z,grad}\rangle^-$ and the differential interaction force $\Delta\langle F_{z,int}\rangle = \langle F_{z,int}\rangle^+ - \langle F_{z,int}\rangle^-$ can be obtained from equations (4.13) and (4.14) as

$$\begin{aligned} \Delta\langle F_{z,grad}\rangle = \; & \frac{6\omega c}{\pi|z|^4}\mathrm{Im}\Big\{\frac{\alpha_{em}^*}{\varepsilon_0}(\alpha_{ee} - \alpha_{mm}\varepsilon_0)\Big\}\Big(\tfrac{1}{2}h_\parallel^{inc} + h_z^{inc}\Big) \\ & + \frac{24\omega^2}{\pi k^2|z|^5}\left[\mathrm{Re}\left\{\frac{\alpha_{ee}\alpha_{em}^*}{\varepsilon_o}\right\}[\boldsymbol{\sigma}_E^{inc}]_z - \mathrm{Re}\left\{\alpha_{mm}\alpha_{em}^*\right\}[\boldsymbol{\sigma}_H^{inc}]_z\right] \end{aligned} \tag{4.16}$$

$$\Delta\langle F_{z,int}\rangle = \frac{2\omega c k^4}{3\pi}\Big[\mathrm{Im}\Big\{\frac{\alpha_{em}^*\alpha_{ee}}{\varepsilon_o}\Big\}[\boldsymbol{\sigma}_E^{inc}]_z + \mathrm{Im}\Big\{\alpha_{mm}\alpha_{em}^*\Big\}[\boldsymbol{\sigma}_H^{inc}]_z\Big] \tag{4.17}$$

where $h_\parallel^{inc} = \frac{1}{2\omega c}\mathrm{Im}\left\{\mathbf{E}_\parallel^{inc}\cdot\mathbf{H}_\parallel^{inc*}\right\}$ and $h_z^{inc} = \frac{1}{2\omega c}\mathrm{Im}\left\{\mathbf{E}_z^{inc}\cdot\mathbf{H}_z^{inc*}\right\}$ are the tangential and longitudinal helicity density, respectively. We find that the differential force is proportional to the difference in helicity density between the incident light and the auxiliary beam, i.e. $h^{inc+} - h^{inc-} = 2h^{inc}$. Since we had defined $h^{inc} = h^{inc+}$, we observe that the differential gradient force measured in this procedure is directly proportional to the desired h^{inc} of the incident chiral light. From equation (4.16) we see that the differential gradient force depends on the helicity density of the incident light, whereas (4.17) predicts that the differential interaction force carries only information on the spin angular momentum of the incident light. When using optimally chiral light[94] satisfying the relation $\mathbf{E} = \pm i\eta_0\mathbf{H}$ with $\eta_0 = \sqrt{\mu_0/\varepsilon_0}$,

the two spin angular momentum densities are such that $\boldsymbol{\sigma}_H^{inc} = \boldsymbol{\sigma}_E^{inc}$. Note that circularly polarized light is a particular case of optimally chiral light.

When analyzing the first and the second terms in equation (4.16), we note that the pre-factor containing z^{-5} grows larger than the corresponding z^{-4} pre-factor for sub-wavelength distances. The magnitude of the two contributions to the differential gradient force are, however, also determined by the material polarizabilities. In this context, we must observe that for nanoparticles made of low loss materials like silicon, the values for the polarizabilities α_{ee} and α_{mm} are mainly real when the particle is much smaller than the optical wavelength (i.e., at the quasistatic limit). Assuming the same particle has chirality, we also observe that α_{em} is mainly imaginary (see for example the expression (9) in Ref. [114] or (7) in Ref.[115]). Therefore, when the chiral tip is made of a low-loss material and much smaller than the optical wavelength, the term $\mathrm{Im}\{\alpha_{ee}\alpha_{em}^*\}$ is larger than the term $\mathrm{Re}\{\alpha_{ee}\alpha_{em}^*\}$. Similarly, we find that $\mathrm{Im}\{\alpha_{mm}\alpha_{em}^*\} \gg \mathrm{Re}\{\alpha_{mm}\alpha_{em}^*\}$. Taken together, even though the considered tip size is not deeply sub-wavelength, we find that for practical sizes and material properties of the tip, as shown in Section 4.3 (see also Appendix A section 4), the first term in equation (4.16) is dominant over the second term. For this reason, we may approximate the differential gradient force as

$$\Delta\langle F_{z,grad}\rangle \sim \frac{6\omega c}{\pi|z|^4}\mathrm{Im}\Big\{\frac{\alpha_{em}^*}{\varepsilon_0}(\alpha_{ee}-\alpha_{mm}\varepsilon_0)\Big\}\Big(\tfrac{1}{2}h_{\parallel}^{inc}+h_z^{inc}\Big) \tag{4.18}$$

and the validity of such approximation will be confirmed by the numerical results. It is clear that the strength and sign of the differential gradient force depends on α_{em}^* and thus relies on the chiral properties of the tip. For small tip-sample distances, the differential gradient force is expected to constitute the dominant contribution to the measured force, thus offering a means of experimentally extracting information about the helicity density. Unless otherwise stated, we will use equation (4.18) to determine the differential force in the follwoing sections.

4.2 Mie Scattering Formalism

We next study the characteristics of the differential gradient force. We see from equation (4.18) that $\Delta\langle F_{z,grad}\rangle$ depends on the polarizability of the tip material, including the electromagnetic polarizability. To model the tip polarizability, we assume that the tip can be described as a spherical chiral nanoparticle (NP). We also assume that the following constitutive relations hold for the chiral NP: $\mathbf{D} = \varepsilon_0\varepsilon_r\mathbf{E} + i\sqrt{\varepsilon_0\mu_0}\kappa\mathbf{H}$ and $\mathbf{B} = \mu_0\mu_r\mathbf{H} - i\sqrt{\varepsilon_0\mu_0}\kappa\mathbf{E}$, where ε_r and μ_r are the relative permittivity and relative permeability, respectively [94, 116]. The chirality parameter κ is an empirical quantity that provides the chiral strength of the material under consideration. We can next relate the electric, magnetic and electro-magnetic polarizabilities through the material parameters by using Mie scattering theory as [94, 114, 119]: $\alpha_{ee} = -6\pi i\varepsilon_0 b_1/k_0^3$, $\alpha_{mm} = -6\pi i a_1/k_0^3$ and $\alpha_{em} = 6\pi i c_1/(ck_0^3)$ where c is the free space speed of light, k_0 is the wavenumber in free space and b_1, a_1, c_1 are the Mie coefficients. In our calculations, the material parameters of the isotropic chiral NP such as ε_r and μ_r are those of crystalline silicon [120] with $\mu_r = 1$.

We next place the sphere (i.e., the tip) just above a flat and transparent dielectric substrate such that the distance between the sphere's surface and the substrate surface is 5 nm. The system is subsequently illuminated from the bottom with a plane wave of field strength 1.5×10^6 Vm^{-1} (incident intensity of 3.0 mW/μm^2) that is either in the LCP ($\mathbf{E}^{inc+} = E^{inc}\hat{\mathbf{x}} + iE^{inc}\hat{\mathbf{y}}$) or RCP ($\mathbf{E}^{inc-} = E^{inc}\hat{\mathbf{x}} - iE^{inc}\hat{\mathbf{y}}$) state, and which propagates through the transparent dielectric material toward the sphere. The CP wave induces an electric and magnetic dipole in the chiral sphere, and the presence of the substrate can subsequently be modeled by including an image of the induced electric and magnetic dipoles [29, 32], analogous to the procedure used for the point dipole model in section 4.1. For simplicity, it is assumed that the image dipole strength is identical to the induced dipole in the sphere. In the current configuration, the distance between the location of the dipole and its image is $2(r_{\mathrm{NP}} + 5\text{ nm})$, where r_{NP} is the radius of the sphere. We calculate the differential gradient

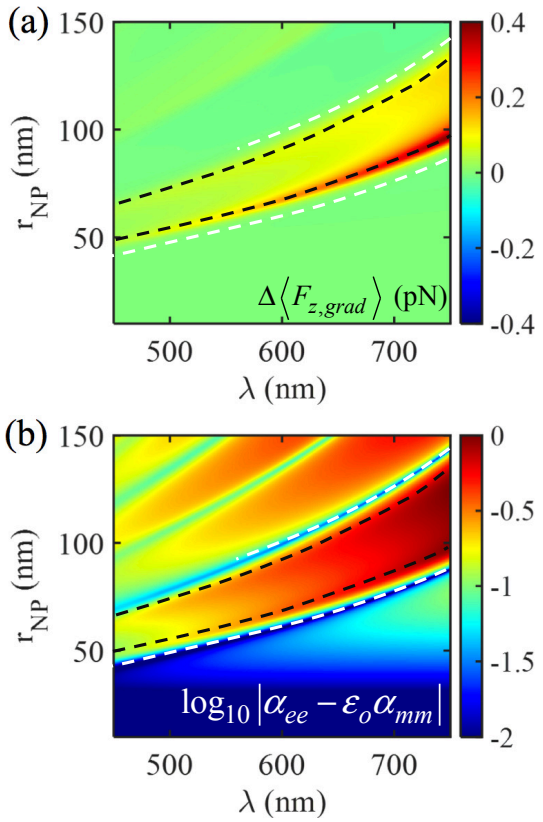

Figure 4.2: (a) Differential gradient force spectrum in pN. (b) Normalized magnitude spectrum of $\alpha_{ee} - \varepsilon_0 \alpha_{mm}$ for different radii of the chiral NP. The material properties of the chiral NP, ε_r and μ_r are considered the same as silicon with $\mu_r = 1$ and $\kappa = 0.1$. In all calculations, the tip-image dipole center-center distance is $|z| = 2r_{NP}+10$ nm. Black dashed lines indicate resonance condition of c_1 and white dashed lines indicate the local minima in the plot, which approach the Kerker condition.

force spectrum with the aid of equation (4.18) and plot it as a function of sphere radius and excitation wavelength in Fig. 4.2(a). In all calculations, the value of the bulk chirality κ of the sphere is considered real and set to 0.1 [121, 122]. It is clear that nonzero $\Delta\langle F_{z,grad}\rangle$ is achieved under certain experimental conditions. In particular, the maxima are seen to co-localize with the resonant spectral position of the electro-magnetic Mie coefficient c_1 of the chiral NP. The black dotted lines show the location of the peak values of $\mathrm{Im}(c_1)$. Changing κ does not alter the spectral resonances, but instead changes the sign and magnitude of the differential force proportionally.

A careful inspection of equation (4.18) suggests that, for any chosen r_{NP} and κ of the

tip, $\Delta\langle F_{z,grad}\rangle$ may approach zero when the first Kerker condition of the chiral NP is met, irrespective of helicity density of the incident light. The Kerker condition is $\alpha_{ee} = \varepsilon_0\alpha_{mm}$ [105, 123, 124], and the magnitude of the quantity $\alpha_{ee} - \varepsilon_0\alpha_{mm}$ is plotted in log scale in Figure 4.2(b) as a function of radius and excitation wavelength, while κ is fixed at 0.1. The white dotted lines depict the conditions where the logarithm of $|\alpha_{ee} - \varepsilon_0\alpha_{mm}|$ (normalized to maximum) has a value below -1.5 and the relation $\alpha_{ee} = \varepsilon_0\alpha_{mm}$ is approximately satisfied whereas the black dotted lines show the resonant position of electro-magnetic Mie coefficient c_1 as found in panel (a). The finite separation between the two curves assures that the Kerker condition is less likely to have any impact on helicity density measurements if the force difference measurement is properly maximized.

4.3 Full Wave Simulations

To further validate our analytical findings, we perform 3D full wave simulations to determine the force exerted on a chiral tip when it is placed above a dielectric substrate. We use the finite element method implemented in COMSOL Multiphysics. In the simulation, the tip is modeled as an isotropic chiral sphere [25, 125, 126] with the same material parameters as used above in Mie scattering formalism. Indeed, ε_r and μ_r of the sphere are same as that of silicon with $\mu_r = 1$ and the bulk chirality parameter is $\kappa = 0.1$. As shown in figure 4.3(a), the sphere is placed above a semi-infinite glass substrate ($n = 1.5$) and the distance between the glass surface and the sphere surface is 5 nm. The system is then sequentially illuminated by LCP and RCP plane waves of field strength 1.5×10^6 Vm^{-1}, corresponding to 3.0 mW/μm^2, in the bottom illumination scheme. The force exerted on the chiral sphere is determined by integrating the Maxwell's stress tensor over the outer surface of the tip (i.e., the sphere) [25]

Figures 4.3(b), (c), and (d) show the time averaged-force difference spectrum for spheres of

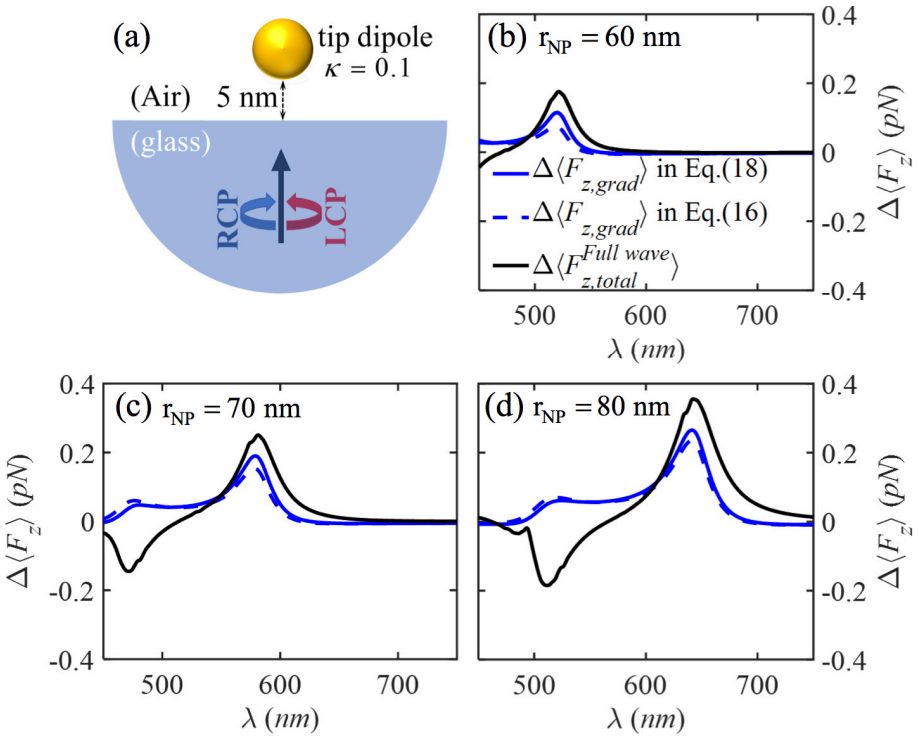

Figure 4.3: (a) Schematic of the chiral tip sphere above a glass substrate ($n = 1.5$) with radius r_{NP} and tip-surface and glass surface distance of 5 nm used in the FEM simulation. The material properties of the sphere, ε_r and μ_r are the same as silicon, with $\mu_r = 1$ and $\kappa = 0.1$. The system is illuminated by an incoming plane wave (first LCP then RCP) from below. Time-averaged differential gradient force from analytical calculation using equation 4.18 (blue solid) and equation 4.16 (blue dotted) and total force from full-wave simulations (black solid curve), for a chiral NP radius with radius (b) $r_{NP} = 50$ nm, (c) $r_{NP} = 60$ nm, and (d) $r_{NP} = 70$ nm.

radius of 50 nm, 60 nm, and 70 nm, respectively. The blue solid and dotted curves show the analytical result using equation (4.18) and equation (4.16), whereas the full-wave FEM result is indicated by the black solid line. For all three cases, the FEM simulation closely follows the analytical result obtained for the main dipolar mode, which is found at the longer wavelength and peaks with the Mie resonance of the c_1 coefficient. On resonance, the dipolar differential gradient force (blue curves) constitutes the dominant contribution to the total force difference (black curve). The dominance of the dipolar contribution grows more obvious as the radius is increased. The difference between the FEM simulation and the analytical results can be attributed to higher order multipole contributions, which are not considered in the dipolar approximation. The small difference between the solid and dotted blue curves

is due to the contribution of z^{-5} distance dependent force term in equation (4.16). This term does not carry any information on the helicity density and its significance decreases for larger radii, as is evident in Figures 4.3(b)-(d). Near resonance, the differential force is of the order of 0.25 pN for the 80 nm radius tip ($\kappa = 0.1$). Although such forces are near the noise floor of a typical PiFM microscope, sensitive experiments are likely able to resolve the targeted differental force under optimized conditions [127].

The dip at lower wavelengths (black curve) for the 70 nm and 80 nm radius tips in Figure 4.3(c) and (d) is attributed to the differential interaction force, as defined in equation (4.17). This is because, equation (4.18) is positive-valued whereas (4.17) and the z^{-5} dependent term of equation (4.16) are negative-valued in the considered wavelength range. In the same lower wavelength region, the magnitude of $\Delta\langle F_{z,grad}\rangle$ is comparatively much smaller than the magnitude of $\Delta\langle F_{z,int}\rangle$ for the 70 nm and 80 nm radius tips.

4.4 Force Map of Helicity Density

Finally, we present the differential force map of the helicity density for a focused chiral beam, a scenario of direct relevance to microscopy applications. The situation is schematically shown in Figure 4.4(a) where an isotropic chiral sphere of radius $r_{NP} = 80$ nm is scanned over the focal region of the incident beams above glass substrate. We assume a circularly polarized Gaussian beam of 2 mW average power at a wavelength of $\lambda = 641$ nm as the incident light source, which is focused by a 1.4 NA oil ($n = 1.518$) objective lens. The focal plane electric and magnetic field components used in the simulation are obtained from reference [32], page 62. We first calculate the normalized helicity density distribution at the focal plane for a focused LCP beam, which is shown in 4.4(b). We next calculate the differential force $\Delta\langle F_{z,grad}\rangle$ using equation (4.18). In Figure 4.4(c), $\Delta\langle F_{z,grad}\rangle$ is shown for the case of a tip of radius $r_{NP} = 80$ nm. As equation (4.18) suggests, the force difference

has the same spatial dependence as the non-zero helicity density of the focused LCP beam shown in Figure 4.4(b).

Lastly, we consider a chiral nanoprobe with properties as those of a helical carving of regular achiral tips [13]. Such chiral tips display dominant longitudinal chirality [128] and in the dipolar approximation this is reflected in the polarizabilty tensors as [116, 128]

$$\begin{aligned} \underline{\boldsymbol{\alpha}}_{ee} &= \alpha_{ee}^{zz}\hat{\mathbf{z}}\hat{\mathbf{z}}; \\ \underline{\boldsymbol{\alpha}}_{mm} &= \alpha_{mm}^{zz}\hat{\mathbf{z}}\hat{\mathbf{z}} \\ \underline{\boldsymbol{\alpha}}_{em} &= \alpha_{em}^{zz}\hat{\mathbf{z}}\hat{\mathbf{z}} \end{aligned} \tag{4.19}$$

Here we have ignored the non-diagonal components of the polarizability tensors for brevity. Such an approximation is reasonable as long as the helical axis is aligned along the main propagation axis. We note that even though the finite number of helical turns introduces non-zero elements of the polarizability tensor, such contributions are negligible compared to the dominant diagonal elements [128]. Under these conditions, the differential gradient force for the helical-shaped tip turns out be

$$\Delta\langle F_{z,grad}\rangle \sim \frac{6\omega c}{\pi|z|^4}\mathrm{Im}\Big\{\frac{\alpha_{em}^{zz*}}{\varepsilon_0}(\alpha_{ee}^{zz} - \alpha_{mm}^{zz}\varepsilon_0)\Big\}h_z^{inc} \tag{4.20}$$

The details of the derivation can be found in Appendix A section A.5. Interestingly, the differential gradient force for the helical-shaped tip is only sensitive to the longitudinal component of the helicity density. In contrast, the isotropic chiral tip measures both the transverse and longitudinal components in the differential force measurement, as expressed in equation (4.18).

To demonstrate these features, we consider a helical-shaped tip that is placed above a glass substrate, and subsequently scanned over the focal region as sketched in Figure 4.4(d). Figure 4.4(e) shows the calculated longitudinal component of the helicity density, revealing a

donut shaped profile. Next, to calculate the differential force we use the same polarizability values of the isotropic chiral sphere in Figure 4.4(a) for α_{ee}^{zz}, α_{mm}^{zz} and α_{em}^{zz}. The map of $\Delta\langle F_{z,grad}\rangle$ for the helical-shaped tip is depicted in figure 4.4(f), showing the expected donut profile that replicates the longitudinal component of the helicity density of the incident LCP beam. In Appendix C, we also present the helicity density maps determined through the differential force of a focused azimuthally radially polarized beam (ARPB) [105, 94, 115]. We note that in principle, a proper design of the nanoprobe should also allow for mapping the transverse components of the helicity density. This would require a probe with polarizability elements $\alpha_{em}^{xx} \neq 0$ and/or $\alpha_{em}^{yy} \neq 0$ with $\alpha_{em}^{zz} = 0$, which can be accomplished if the chiral probe exhibits a helical current path in the transverse direction.

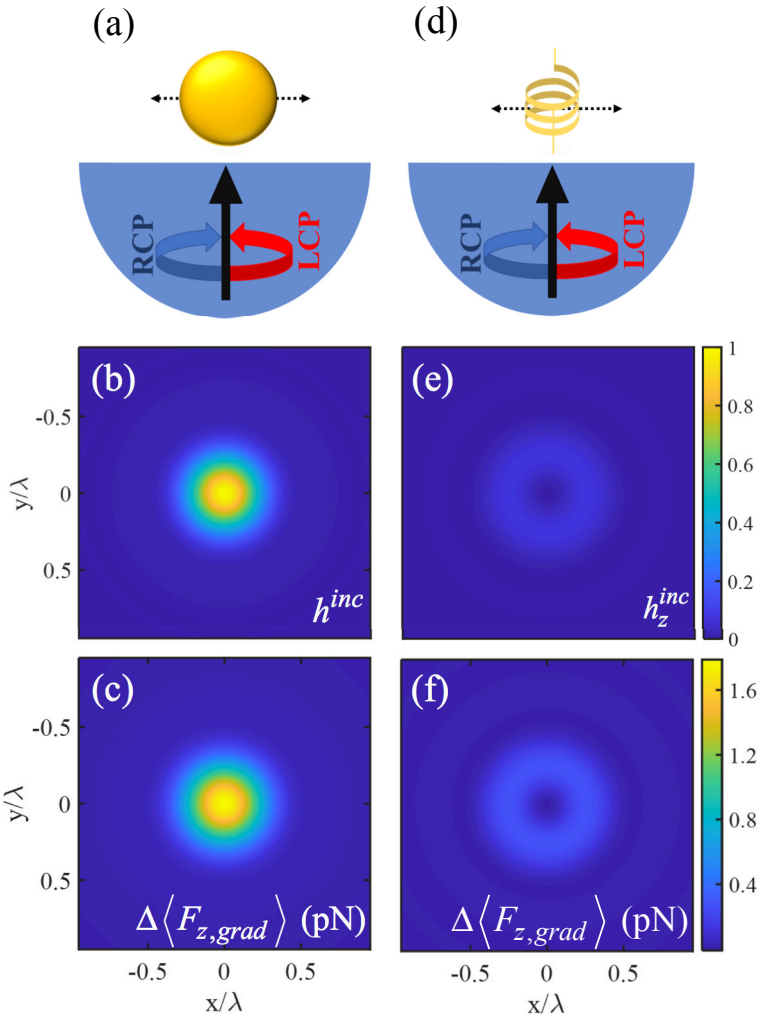

Figure 4.4: (a) Sketch of an isotropic chiral scatterer being horizontally scanned over a glass substrate through the focus of a circularly polarized (LCP/RCP) beam. (b) The focal plane distribution of total normalized helicity density ($h^{inc} = \frac{1}{2\omega c}\mathrm{Im}\{\mathbf{E^{inc}} \cdot \mathbf{H^{inc*}}\}$) of the incident circularly polarized (LCP) light focused by a 1.4 NA oil objective. (c) The differential force map, $\Delta\langle F_{z,grad}\rangle$ at the focal plane for a chiral isotropic tip of radius $r_{NP} = 80$ nm. (d) Sketch of a helical-shaped tip in the same configuration as in (a). (e) Spatial dependence of the longitudinal component of the normalized helicity density ($h_z^{inc} = \frac{1}{2\omega c}\mathrm{Im}\{E_z^{\mathrm{inc}} H_z^{\mathrm{inc*}}\}$) in (b). (f) Differential force map for the helical-shaped tip. The polarizability strength of the isotropic and helical-shaped tip has been set to the same value.

4.5 Effect of beam imperfection

In our proposed technique, the beam of interest and the auxiliary beam of opposite handedness require to have equal energy densities, namely $|\mathbf{E}^{inc+}|^2 = |\mathbf{E}^{inc-}|^2$ and $|\mathbf{H}^{inc+}|^2 = |\mathbf{H}^{inc-}|^2$, to obtain the differential force in the form of equation 18. Here, we investigate the effect of deviation from this perfect condition for a representative case. In this case study, we assume a perfect LCP beam, but a non-ideal RCP auxiliary beam. This scenario may correspond to an actual experimental situation in which the RCP beam is slightly elliptical. To model this, we introduce an error ϵ in the auxiliary beam as $|E_y^{inc-}| = |E_y^{inc}(1-\epsilon)|$ and $|H_x^{inc-}| = |H_x^{inc}(1-\epsilon)|$ where $|E_y^{inc+}| = |E_y^{inc}|$ and $|H_x^{inc+}| = |H_x^{inc}|$. Under these conditions, we retrieve the original formulation for the differential force, plus an additional force contribution that originates from the error term. This extra term is given below.

$$
\begin{aligned}
\Delta\langle F_{z,grad}\rangle_{error} = \; & -\frac{3}{2\pi|z|^4}\Bigg\{\frac{1}{2}\left(-\frac{|\alpha_{ee}|^2}{\varepsilon_0}+\mu_0|\mu_0^{-1}\alpha_{em}|^2\right)\left(\frac{1}{2}|\epsilon E_y^{inc}|^2-\mathrm{Re}(\epsilon)|E_{\mathrm{y}}^{\mathrm{inc}}|^2\right) \\
& +\frac{1}{2}\left(-\frac{|\alpha_{em}|^2}{\varepsilon_0}+\mu_0|\alpha_{mm}|^2\right)\left(\frac{1}{2}|\epsilon H_x^{inc}|^2-\mathrm{Re}(\epsilon)|H_{\mathrm{x}}^{\mathrm{inc}}|^2\right) \\
& +\mathrm{Re}\left(\frac{\alpha_{ee}\alpha_{em}^*}{\varepsilon_0}+\alpha_{mm}^*\alpha_{em}\right)\mathrm{Re}\left(\frac{1}{2}\epsilon\mathbf{E}_t^{inc}\cdot\mathbf{H}_t^{inc*}\right) \\
& +\mathrm{Im}\left(\frac{\alpha_{ee}\alpha_{em}^*}{\varepsilon_0}+\alpha_{mm}^*\alpha_{em}\right)\mathrm{Im}\left(\frac{1}{2}\epsilon\mathbf{E}_t^{inc}\cdot\mathbf{H}_t^{inc*}\right)\Bigg\} \\
& -\frac{6\omega}{\pi k^2|z|^5}\Bigg\{\mathrm{Re}(\mu_0\alpha_{em}\alpha_{mm}^*)\mathrm{Im}(\epsilon H_x^{inc}H_y^{inc*})-\mathrm{Re}(\alpha_{ee}\alpha_{em}^*)\mathrm{Im}(\epsilon E_x^{inc}E_y^{inc*}) \\
& +\mathrm{Im}\left[(|\alpha_{em}|^2-\mu_0\alpha_{ee}\alpha_{mm}^*)(\epsilon^2-2\epsilon)(E_y^{inc}H_x^{inc*})\right]\Bigg\}
\end{aligned}
\tag{4.21}
$$

To obtain an impression of the magnitude of this additional force, we calculate $\Delta\langle F_{z,grad}\rangle_{error}$ for a chiral scatterer (tip) of $\kappa = 0.1$ and 80 nm radius under LCP/RCP illumination of field strength 1.5×10^6 Vm^{-1} (incident intensity of 3.0 $\mathrm{mW}/\mu\mathrm{m}^2$) at wavelength of 641 nm. Here, we introduce the error, ϵ in the RCP light. Fig. 4.5 shows the variation of $\Delta\langle F_{z,grad}\rangle_{error}$

strength for increasing magnitude of the error parameter. The Figure shows that the additional force, $\Delta\langle F_{z,grad}\rangle_{error}$ increases with ϵ and remains below the noise floor ~ 0.08 pN for maximum error of $\epsilon = 0.03$. Thus, we may conclude that up to an amplitude variation of $\sim 3\%$ ($\epsilon = 0.03$) the error force is below the detection limit and is unlikely to affect the actual measurement in a significant way.

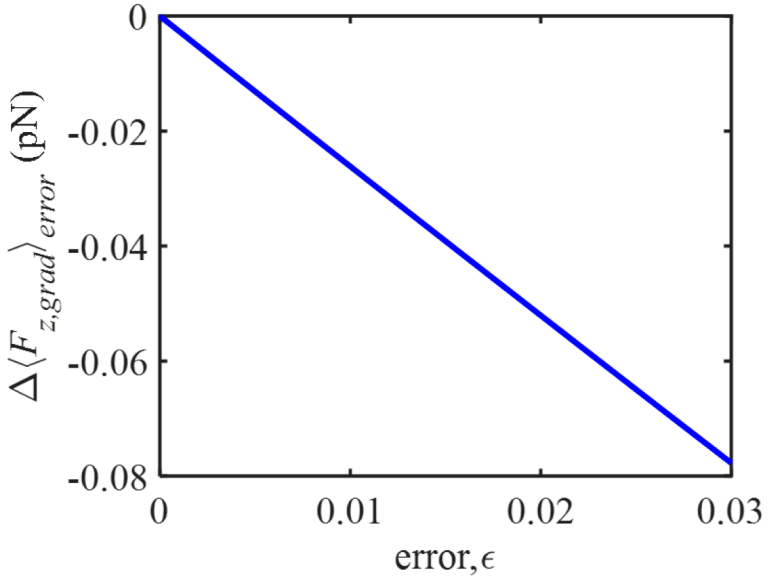

Figure 4.5: The additional force $\Delta\langle F_{z,grad}\rangle_{error}$ as a function of error parameter ϵ in the auxiliary beam (RCP) for an isotropic chiral scatterer (tip) of radius $r_{NP} = 80$ nm and $\kappa = 0.1$. The incident illumination is assumed to be plane wave LCP/RCP with electric field strength 1.5×10^6 Vm^{-1} at a wavelength of 641 nm.

4.6 Summary

In this Chapter, we have studied the information contained in the photo-induced force exerted on a chiral tip (modeled as a chiral nanosphere) when it is illuminated by chiral light. Our theoretical analysis reveals that the differential force is directly sensitive to the chiral properties of light. In particular, the dominant component to the differential gradient force is directly proportional to the helicity density of the incident chiral light, whereas the differential scattering force is sensitive solely to the spin angular momentum of the applied

light. Using realistic values for the illumination intensity, tip dimension, and the chirality parameter of the tip, we find that the differential force can reach detectable values of several hundreds of fN, just above the noise floor of common scan probe microscopy systems. Finally, we provided an error tolerance of our proposed measurement method based on the auxiliary beam imperfections. These findings are significant because a direct characterization of optical chirality at the nanoscale has hitherto been challenging. The observation that the differential gradient force can map out the local helicity density of the light is relevant for applications where knowledge of the chiral state of light at sub-diffraction-limited dimensions is important, including for sorting of chiral enantiomers with spatially confined light.

Chapter 5

Thermal dynamics of nanoprobe

Upon light illumination, the tip of a nanoprobe can absorb part of the incident energy, while scattering the rest. Light absorption eventually increases the local temperature at the tip apex, which gives subsequently rise to thermal expansion of the material. In a typical PiFM experiment, the light is amplitude modulated, which means that the thermal expansion of the material is a dynamic process. The dynamic behavior depends on several material properties, which include the absorption coefficient, thermal expansion coefficient, thermal diffusivity, heat capacity, and effective thermal conductivity [28, 39]. Whereas the thermal dissipation in a typical bulk metal is very fast and not likely to play a role in PiFM, the local small expansion at the tip's apex may display dynamic behavior that can be observed in the PiFM experiment.

In PiFM experiments with light modulation frequencies on the order of 100 kHz, the illumination time is in the ~ 10 μs range, whereas the thermal expansion dynamics of the sample or tip can unfold on the sub-μs to μs timescale. In this scenario, the light-induced heating of the material cannot be considered instantaneous. During the illumination period, we may expect heating of the tip/sample by the source in conjunction with dissipation dynamics.

Heat dissipation away from the illuminated area is driven by heat diffusion and radiation into the surrounding environment. The exact heating/cooling dynamics can be rather complex, especially for three-dimensional objects placed on substrates where interfacial heat transport is important. However, FT-PiFM experiments can retrieve effective parameters (τ_h/τ_c) of the temperature evolution in the sample of the form $T(t) = 1 - \exp -t/\tau_h$ [during light on] and $T(t) = \exp -t/\tau_c$ [during light off] where τ_h/τ_c are the heating/cooling times that effectively captures the dynamics during the on/off illumination periods [39]. In such sub-μs dynamic measurements, the nanotip expansion dynamics can be expected to play a significant role. Although the nanotip expansion is usually assumed to be too small to have a noticeable effect, the validity of this assumption has not been systematically examined.

In this chapter, we numerically analyze the expansion of the nanotip and its relaxation dynamics during laser light modulation. In section 5.1 we present and discuss a simulation model used for numerical evaluation. We subsequently determine the steady state expansion amplitude and its dynamic behavior, i.e. relaxation time t_c for two commonly used tips, namely a gold-coated silicon tip and a bare silicon tip. Furthermore, we verify the t_c found from simulation with experimental measurements using the FT-PiFM model discussed in section 2.2.2. Finally, we evaluate the effect of tip expansion under regular PiFM experimental conditions and expand on the validity of FT-PiFM model.

5.1 Numerical model and simulation setup

We are interested in determining nanotip expansion and relaxation dynamics due to laser modulation. To gain insight in the thermal dynamics of the tip, we perform time-dependent simulations using the *Heat Transfer in Solids* and *Solid Mechanics* modules in COMSOL Multiphysics. When considering laser-induced heating during on and off times, the *Heat Transfer in Solids* module provides the temporal rise/fall of the local temperature in the

vicinity the tip apex. Using the time-dependent temperature of the material, we then compute the thermal expansion/relaxation of the material and determine the thermal stress profile in the *Solid Mechanics* module to find the displacement at the tip apex as a function of time.

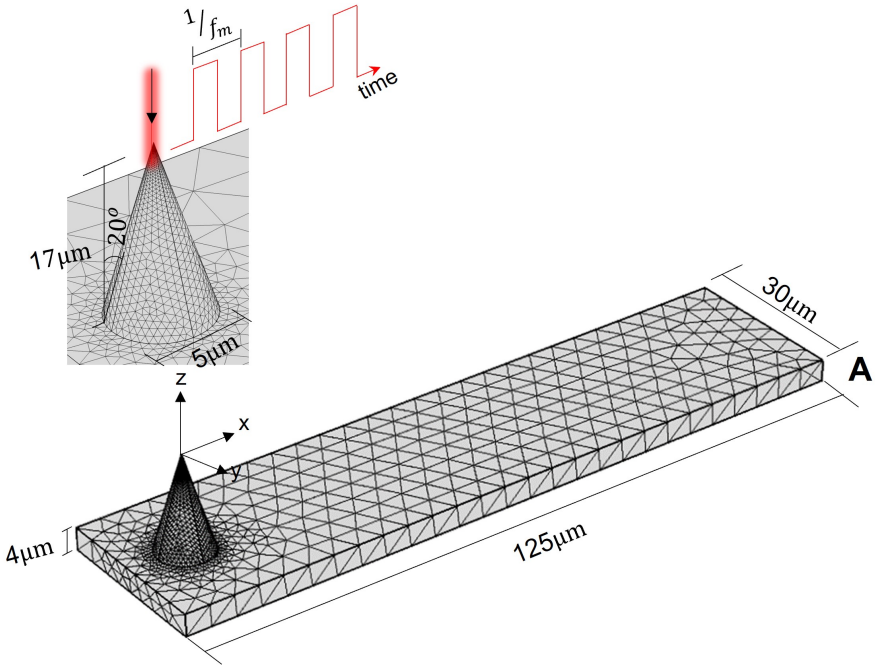

Figure 5.1: Finite element method (FEM) simulation of the cantilevered tip system upon laser illuminationm, using a modulation frequency of f_m. Detailed dimensions of the ACL type cantilever are indicated. The tetrahedral blocks represent the finite elements. **A** marks the rear end of the cantilever beam.

We perform simulations on two different tips: 1) a bare silicon tip, and 2) a silicon tip coated with a 40 nm gold layer. The relevant geometry of the cantilevered tip is shown in Fig. 5.1. The *Heat Transfer in Solids* module solves the following heat diffusion equation [58, 60] as a function of time.

$$\rho C_p \frac{\partial T}{\partial t} - \nabla \cdot (k \nabla T) = Q_{in} \tag{5.1}$$

where, ρ, C_p, T and k are the density, heat capacity, temperature, thermal conductivity

of the tip material and Q_{in} (Wm^{-3}) is the volumetric heat source inside the tip. In our situation, the laser illumination is the source of heating at the tip apex. We assume that the incident laser has a Gaussian profile with beam waist $\sigma_x = \sigma_y = 0.3$ μm that is modulated at f_m. The modulated laser illumination gives rise to laser-induced heating of the tip material near the apex. In the current model model, we define the laser induced volumetric heat, Q_{in} as [129]:

$$Q_{in} = Q_o(1 - R_c)\frac{A_c}{\pi\sigma_x\sigma_y}e^{-\frac{1}{2}[(\frac{x}{\sigma_x})^2+(\frac{y}{\sigma_y})^2]}e^{-A_c|z|} \tag{5.2}$$

where Q_o is the input power of the laser beam, A_c and R_c are the absorption coefficient and reflection coefficient of the tip material, respectively. The gold-coated silicon tip is implemented by employing a thin film coating of gold near the solid Si tip with coating thickness of 40 nm. We use the optical properties A_c and R_c of Si and gold from refs. [130] and [131]. We obtain the thermal properties, for example heat capacity and thermal conductivity, from refs. [132] and [133] for Si, and from refs. [134] and [135] for gold. In addition, the simulation requires several temperature-dependent physical properties for both silicon and gold, namely the density [132, 136], the Young's modulus [137, 138], the thermal expansion coefficient [139, 140] and the Poisson's ratio [141, 142]. The exact form of the volumetric heat input are slightly different from equation 5.2, particularly at locations away from the tip apex and for the gold-coated silicon tip, as discussed in the Appendix D. An input laser power of $Q_0 = 1$ mW and a laser wavelength of $\lambda = 0.8$ μm is chosen for all simulations. In addition, for the heat transfer simulation, the rear side of the cantilever ($\mathbf{A}$) is fixed at 300 K and the effect of heat loss into the surrounding medium (air) is assumed to be small and has been ignored in the present simulations.

We are interested in analyzing the nanoprobe's thermal contribution to PiFM experiments that are typically performed in the spectral range that stretches from the near-IR (~ 0.8 μm) to the mid-IR(~ 8 μm). The absorption coefficient a_c of the tip material plays a significant

role in determining the tip expansion. a_c decreases considerably with wavelength for silicon [130] while it monotonically increases for gold [131], albeit at a rather slow rate. However, the overall response from a 40 nm gold-coated Si tip is effectively dominated by the Si material, thus showing smaller tip expansion for both the bare Si and the gold-coated Si tips as the wavelength is increased from 0.8 μm toward the mid-IR. In the studies that follow, we have chosen the excitation wavelength as $\lambda = 0.8$ μm, for which the thermal tip expansion is expected to be relatively high. For this setting, we examine the effect of thermal expansion on PiFM measurements under experimental practical conditions.

We use Mutliphysics features like temperature coupling and thermal expansion to determine the thermal expansion from the calculated temperature profile and input the results into the *Solid Mechanics* module. This provides the required thermal stress needed for the *Solid Mechanics* module to perform a time-dependent study by solving the following equation of motion [143]

$$\rho \frac{\partial^2 \mathbf{u}}{\partial t^2} = \nabla_j \cdot \underline{\mathbf{S}} + \mathbf{F_v} \tag{5.3}$$

where ρ is the density of the tip material, $\mathbf{u}$ is the displacement vector, $\mathbf{F_v}$ represents the volume forces like gravity or centrifugal forces, $\underline{\mathbf{S}}$ is the thermal stress tensor with elements S_{ij} where $i = x, y, z$ and $j = X, Y, Z$ and the divergence operator ∇_j refers to the 2^{nd} index of the tensor. The $\mathbf{A}$ side of the cantilever is kept fixed/stationary (boundary condition). Note that we are only interested in the vertical displacement of the tip apex. Thus, we choose the tip apex to be the center of the coordinate system illustrated in Fig. 5.1. In this case, and the vertical displacement retrieved from the simulation represents the required tip apex expansion/relaxation dynamics. The simulation results are discussed in the following section.

5.2 Simulation results

In this section, we discuss the simulation results obtained from the coupled Multiphysics model discussed in section 5.1. Figure 5.2 shows the temporal evolution of the temperature near the tip apex and the resultant tip apex displacement up to 60 μs when the laser light is modulated at a frequency of $f_m = 270$ kHz. The dashed pulse train in Fig.5.2 (a) and (b) represents the modulated laser light. Note that we use the average temperature of a finite volume near the tip apex as a representative of the tip apex temperature. We observe a periodic, exponential-like rise and fall of the temperature for both silicon and gold-coated silicon tips, as shown by the solid red and blue lines in Fig. 5.2(a) and (b). However, the maximum temperature rise in silicon is almost $\sim$ 20 times as high as that in gold-coated silicon, reaching $\sim$ 306 K under the conditions studied. This may be expected since the gold-coated silicon tip is exposed to lower heating compared to the bare silicon tip, while also enjoying a lower thermal relaxation time within thin gold layer. The higher temperature rise in the bare silicon tip results in a higher displacement of the apex compared to the gold-coated silicon tip, as is evident from Fig. 5.2(c) and (d). Similar to the temperature profile, the tip apex displacement also shows exponential-like rise and fall as a function of time, gradually rising to $\sim$ 160 pm for bare silicon and to $\sim$ 4 pm for the gold-coated silicon tip.

In this study, we are particularly interested in the oscillation amplitude of the tip apex (shown as the dashed line range in Fig. 5.2(c) and (d)) and its dynamic behavior within a single cycle. Figure 5.3 (a) shows the tip expansion ΔL_{tip} calculated for a modulation frequency f_m ranging from 100 kHz to 1800 kHz. The red line in Fig. 5.3 (a) shows the tip expansion for the bare silicon tip, which is seen to remain significant over the relevant frequency range. On the other hand, the tip expansion for the gold-coated silicon system (blue) is shown to be at least 15 times less compared to that of the bare silicon tip. Interestingly, the thermal expansion is higher for lower f_m and decreases as f_m increases. This trend is present in both

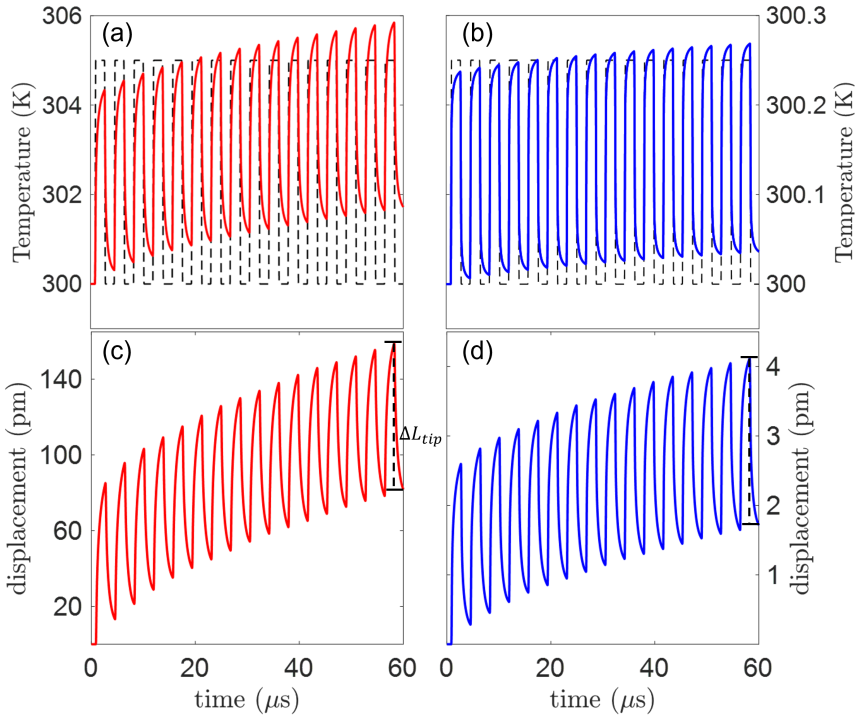

Figure 5.2: Local temperature variation profile at the tip apex region with respect to time for a (a) bare silicon and (b) gold coated silicon nano probes. The black dotted pulse train in the background represents the on-off time of the laser illumination. The resultant tip apex displacement with respect to time for (c) bare silicon and (d) gold coated silicon tips. The range shown by the dotted line in (c) and (d) is the tip expansion amplitude for silicon and gold coated silicon probe. A laser modulation frequency of 270 kHz is used in this simulation.

bare silicon and gold-coated silicon tips and can be explained with the graphical illustration in Fig. 5.3(b). Two periods of the laser modulation are shown in Fig. 5.3(b) for lower f_m in red (top) and for higher f_m in blue (bottom). As the laser on-off duration become shorter, the possible expansion of the tip apex gets smaller due to the earlier start of the heating and cooling cycle at higher f_m.

Since we aim to detect the dynamic behavior of the tip apex displacement, we also calculate the time required for the tip apex to relax during the laser-off half cycle. We name this time as the apparent cooling time, t_c and define it as the time required for tip apex to relax to e^{-1} or 36.8% of the maximum peak displacement in a cycle. In the following section we show the calculated apparent cooling time along with experimentally determined t_c values from

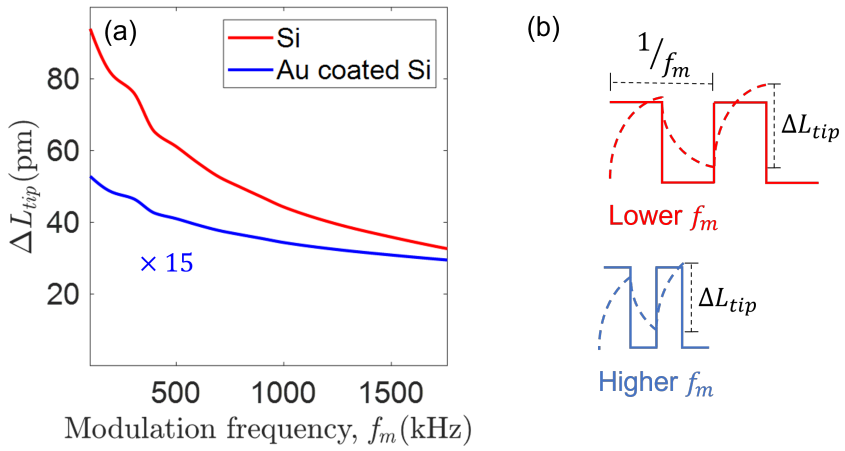

Figure 5.3: (a)Changes in laser induced tip apex expansion with laser modulation frequency, f_m, for a bare silicon tip shown in red curve and for a gold-coated silicon tip shown by the blue curve. The expansion length for the gold-coated silicon is multiplied by 15 times for better comparison. (b) Illustrations describing the decreasing trend of the tip expansion with increasing f_m. Red curve shows the oscillation trend for lower f_m and blue curve shows the trend for higher f_m. A decrease in the expansion for both the rising and falling edges is observed in the bottom plot of (b) when f_m is increased.

FT-PiFM model.

5.3 Apparent cooling time: simulation vs experiment

The FT-PiFM model is capable of quantifying the light-induced thermal relaxation dynamics in materials by recording the time-dependent force exerted on the tip. The FT-PiFM method has previously been demonstrated for registering the sub-μs dynamics of polystyrene (PS) layers (thickness of several hundreds of nm) and layers of silicon naphthalocyanine (SiNC) [39]. However, in this previous work, the potential expansion of the gold-coated Si tip and its dynamics were not considered in the analysis. In this section, we aim to employ the FT-PiFM method to determine the apparent cooling time t_c for bare silicon and gold-coated silicon tips.

The PiFM measurements are performed on an atomic force microscope (AFM) platform

coupled to an inverted optical microscope. For our measurements, we use a pulsed light source that consists of a Ti:sapphire-pumped optical parametric oscillator (Inspire OPO, Radiantis), delivering 200 fs pulses at 80 MHz. We use the idler beam at $\lambda = 809$ nm from the OPO for all the measurements. The beam is modulated by an acoustic optic modulator at frequency f_m with a 50% duty cycle. The modulated laser beam is directed to a scan probe microscope (Vistascope, Molecular Vista), as shown in Fig. 5.4(a), which includes an oil objective lens (NA = 1.42, Olympus) mounted on an inverted optical microscope. The laser beam is focused onto a borosilicate glass slide (0.17 mm thickness). The microscope is operated in non-contact/tapping mode with a gold-coated Si cantilever (ACLGG, Applied NanoStructures inc) as well as an uncoated Si cantilever (ACT, Applied NanoStructures inc). The gold-coated Si cantilever used in the experiments has its first (f_1) and second (f_2) resonance frequency at ~ 250 kHz and ~ 1500 kHz, respectively, while the Si cantilever has resonance frequencies at ~ 270 kHz and ~ 1750 kHz.

We perform an objective scan while keeping the glass slip and cantilevered tip fixed in place. Such a scan provides detectable signals at the position where the tip and the focused beam are aligned, while producing undetectable noise at all other positions. As discussed in section 2.2.2, the magnitude R_1 and phase θ_1 of the measured force at $f = f_0$, along with the magnitude R_2 and phase θ_2 at $f = f_0/2$, are required for retrieving the t_c values from equations 2.26-2.27. Thus, we take two sequential measurements with the same objective scan range, either with laser modulation frequency $f_m = f_o$ or with $f_m = f_o/2$, where f_o can be chosen as either f_1 or f_2. Figure 5.4(b) and (d) show the magnitude $R_1 = |F|$ in μV and phase $\theta_1 = \angle F$ in degrees for an objective scan of 8 μm $\times$ 8 μm area. Here, the force is measured on a gold-coated silicon tip using a laser modulation at $f_m = f_1 = 248$ kHz. We can clearly locate the area in 5.4(b), marked by a black dotted line, where the tip apex and the focused spot of the beam are closely aligned. Similarly, we re-scan the objective over the same area with $f_m = f_1/2 = 124$ kHz and record the magnitude $R_2 = |F|$ (μV) and

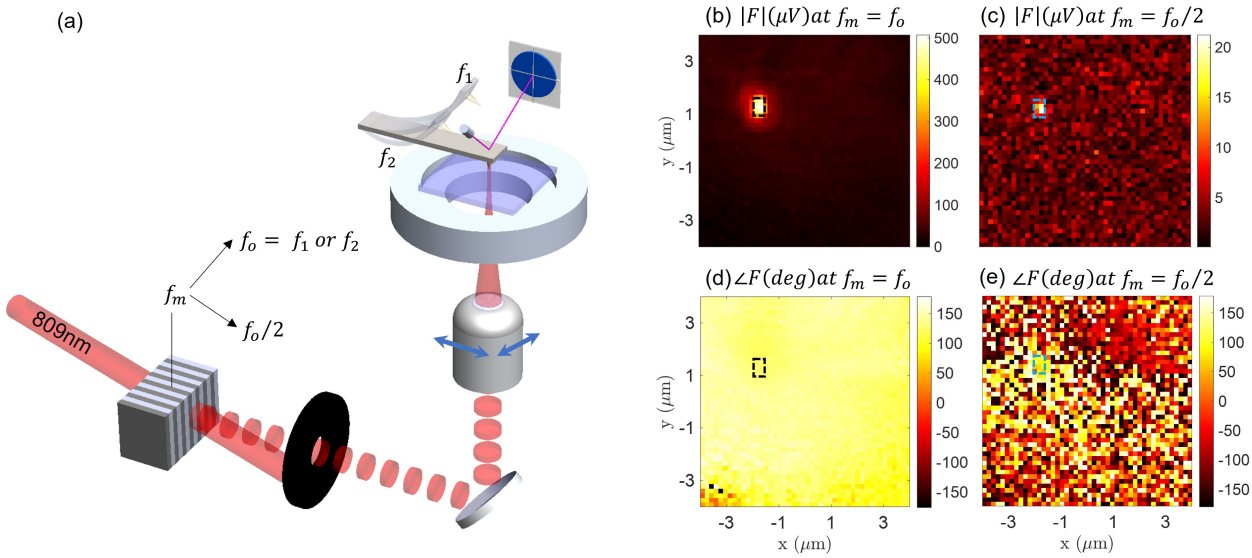

Figure 5.4: Frequency domain PiFM experiment. (a) Schematic of the experiment. The 809nm laser beam is modulated with an acoustic optic modulator and focused at the glass substrate by an 1.42 NA oil objective. The photo-induced force on a bare silicon or gold coated silicon tip is measured while the objective is scanned over a finite area.The magnitude, $|F|(\mu V)$ and phase, $\angle F(\text{deg})$ of the measures force at (b, d) $f_m = f_o$ and (c, d) $f_m = f_o/2$ over a scan area of $8\mu\text{m} \times 8\mu\text{m}$ where f_o is chosen either f_1, the 1st mechanical resonance or f_2, the 2nd mechanical resonance frequency of the cantilever.

phase $\theta_2 = \angle F$ (deg) response shown in fig. 5.4(c) and (e). As indicated by the blue dotted boxes in 5.4(d) and (e), our measurement shows a detectable force at the 1$^{\text{st}}$ overtone of the fundamental resonance, a direct reflection of the presence of force dynamics during the "off" period.

We have performed similar scans for different tips of gold-coated silicon and bare silicon using both f_1 and f_2 as the light modulation frequency. Next, we calculate the apparent cooling time t_c of an illuminated nanoprobe in a real experimental situation by plugging the average magnitude and average phase values of the force marked by dotted square in fig. 5.4(b)-(e) into equations 2.26 and 2.27. In addition, we also calculate the apparent cooling time from our simulation result as illustrated in the inset of fig. 5.5(a) where we have plotted the normalized profile of a single cycle of tip apex expansion for the bare silicon tip when using light modulation at $f_m = 270$ kHz. We have shifted the time axis to align $t = 0$ exactly at the

peak of the displacement and determine the time when ΔL_{tip} reaches the value of e^{-1} or 0.368, corresponding to the apparent cooling time, t_c. The solid red line in fig. 5.5(a) shows the calculated t_c for a range of modulation frequencies. Interestingly, we observe a declining trend of t_c with increasing f_m. We also obtain a similar trend for the gold-coated silicon tip as shown by the blue solid curve in fig. 5.5(b). The data points in fig. 5.5(a) (red) and in fig. 5.5(b) (blue) show the t_c obtained from FT-PiFM measurements on bare silicon and gold-coated silicon tips, respectively. The experimental evaluations also show the declining trajectory, corroborating the trend revealed in the simulation. We attribute this to the inherently chosen exponential model for predicting dynamic behavior under any f_m. However, the close correspondence between measurement and simulation provides clear evidence of existence of nanotip expansion dynamics under regular PiFM operation conditions.

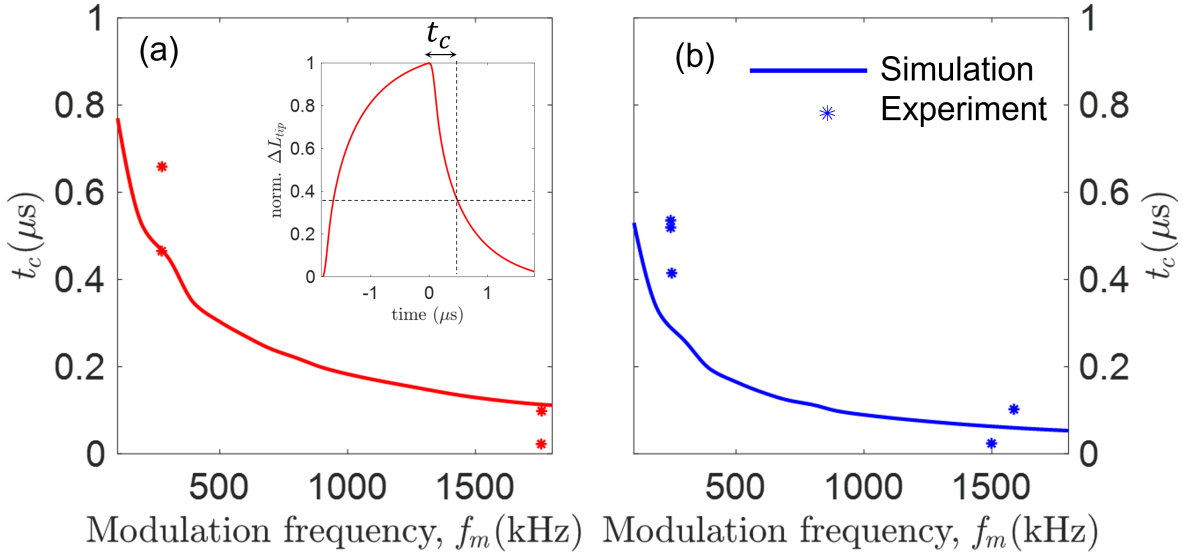

Figure 5.5: The inset in (a) shows the normalized ΔL_{tip} in a single period with the time axis shifted to align $t = 0$ at the peak. The intersection of the dotted lines shows the time t_c required for ΔL_{tip} to fall to 0.368 of its maximum value. The solid red curve in (a) and blue curve in (b) show the calculated trends of t_c from simulation with increasing f_m for (a) bare silicon and (b) gold-coated silicon tips respectively. The data points in (a) (red) and in (b) (blue) show the t_c retrieved from the measured force magnitude and phase using FT-PiFM.

5.4 Thermal effects of tip in PiFM measurement

In this section, we aim to study the impact of finite tip expansion and relaxation dynamics in PiFM measurements of photo-thermal expansion of sample. In the simple model of PiFM in non contact mode, it is assumed that the changes in the tip-sample distance $z(t)$ due to thermal expansion are linearly proportional to the changes in the photo-induced force. However, the van der Waals force, which is the relevant interaction force considered here, depends on the tip-sample distance in a nonlinear fashion:

$$F_{\mathrm{vdW}}(z) = -\frac{H_{\mathrm{eff}} R}{12 z^2} \tag{5.4}$$

where H_{eff} is the effective Hamaker constant and R is the tip radius. The magnitude of F_{vdW} is modulated because $z(t)$ is modulated by the expansion and relaxation of the sample, as well as by the expansion dynamics of the tip, i.e. $z(t) = z_0 + \Delta L(t)$, with $\Delta L(t) = \Delta L_s(t) + \Delta L_{tip}(t)$, where z_0 is the equilibrium tip-sample distance, $\Delta L_s(t)$ is the height variation of the sample due to expansion of the sample and $\Delta L_{tip}(t)$ is the height variation of the tip due to thermal expansion. Note that in this formulation, $\Delta L_s(t)$ and $\Delta L_{tip}(t)$) are negative in case of a positive expansion of the sample and tip. In the PiFM experiment, the homodyne detection method is sensitive to the change in the interaction force [28]. In the small oscillation limit, the interaction force can be written as a Taylor expansion, and the experiment is sensitive to the first-order term in the expansion. Under these conditions, the quantity reflected in the experiment is: [28, 31]

$$\Delta F_{\mathrm{vdW}}(t) \approx \left(\frac{\partial F_{\mathrm{vdW}}}{\partial z} \right)_{z_o} \Delta L(t) \tag{5.5}$$

Hence, within this description, we may expect that the assumption $\Delta F_{\mathrm{vdW}}(t) \propto \Delta L(t)$ is reasonable. Here, we wish to study the validity of these assumptions for the experimental conditions relevant to the FT-PiFM measurements.

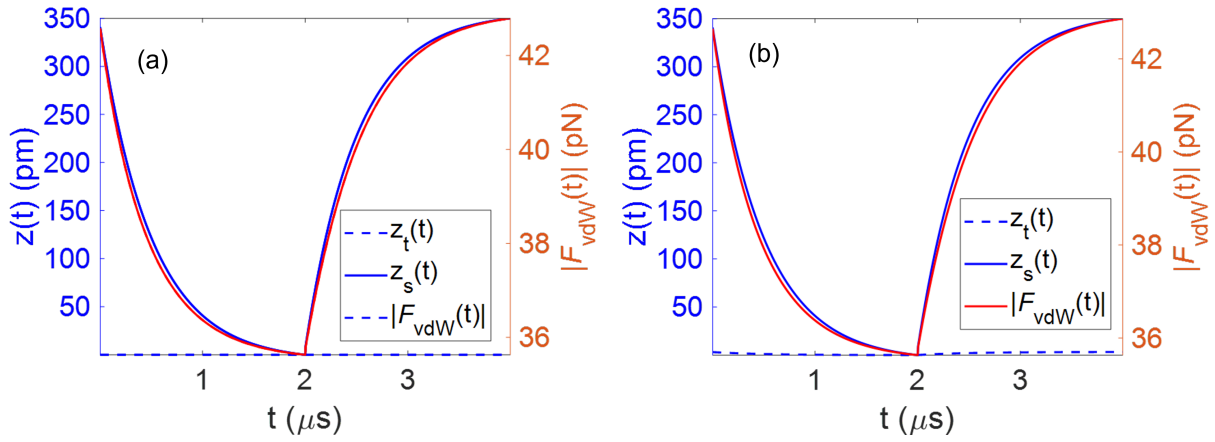

Figure 5.6: Temporal dynamics of the sample expansion (solid blue lines) and the van der Waals force (solid red lines). (a) Dynamics in the absence of tip expansion. (b) Dynamics in the presence of a maximum tip expansion $\Delta L_{tip} = 3.20$ pm with tip heating and cooling times set at $t_h = t_c = 0.5\mu s$. Dotted blue line indicates the expansion dynamics of the tip. Modulation frequency $f = 250$ kHz and the maximum sample expansion is $\Delta L_s = 350$ pm. The sample heating and cooling times are set at $\tau_h = \tau_c = 0.5\mu$s

.

In Figure 5.6(a), we show the dynamics of $z(t)$ and $F_{\text{vdW}}(t)$ during one cycle of the modulation in the absence of tip expansion, i.e. $\Delta L_{tip} = 0$. Here the heating and cooling dynamics are modeled as exponential functions, and the force is calculated from equation 5.4. The modulation frequency is chosen as $f = 250$ kHz, the tip radius is $R = 30$ nm, the equilibrium tip-sample distance is set to $z_0 = 4$ nm, and we consider the sample heating and cooling times of $\tau_h = \tau_c = 0.5$ μs. The Hamaker constant is modeled as $H_{\text{eff}} = \sqrt{H_{\text{Au}}}\sqrt{H_{\text{s}}} = \sqrt{20 \times 10^{-20}}\sqrt{6.5 \times 10^{-20}}$. To examine an extreme case, we choose the maximum expansion of the sample as $\Delta L_s = 350$ pm. Figure 5.6(a) reveals that for a very large expansion of the sample, the assumption that $\Delta F_{\text{vdW}}(t) \propto \Delta L(t)$ essentially holds. Note that the magnitude of the force changes during one cycle is approximately 7 pN under these conditions. In Figure 5.6(b), we show the same dynamics with the tip expansion included. We have used a maximum tip expansion of $\Delta L_{tip} = 3.20$ pm and the heating/cooling times for the tip are chosen as $t_h = t_c = 0.5$ μs, which are obtained from our calculations and measurements for a gold-coated silicon tip at $f_m = 250$ kHz under the current illumination conditions. Since the tip expansion is much less than the sample expansion, the addition of the tip dynamics barely

influences the experiment. However, the effect of the tip can be more substantial for smaller expansion ΔL_s of the sample. For instance, for a PS layer with a thickness up to 500nm the estimated ΔL_s ranges from 20 nm to 60 nm [28], and in these cases the tip expansion may contribute to the measured photo-induced force. To study the effect of tip expansion

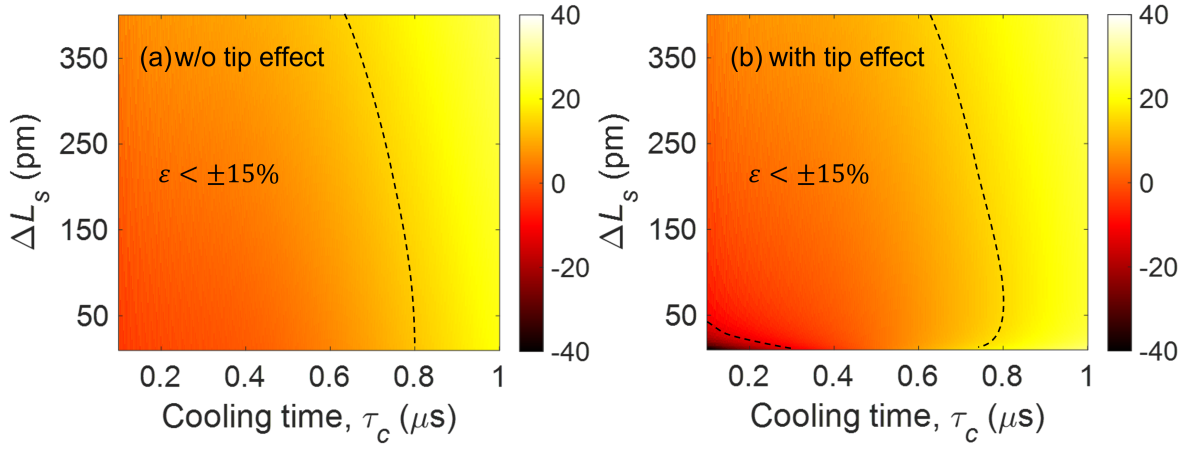

Figure 5.7: Calculated error ϵ between the sample expansion and the simulated van der Waals force in the (a) absence and (b) presence of tip expansion (max $\Delta L_{tip} = 3.20$pm) as a function of the maximum sample expansion and the sample cooling time. The dotted lines demarcate the area where the error is less than $\pm 15\%$

.

in addition to the effects of sample expansion for different cooling times, we determine the error ϵ between the ΔL_s dynamics (using a simple exponential function) and the simulated force dynamics as registered in the experiment. Specifically, we define the error as $\epsilon = \frac{\tau_{\Delta L_s(t)} - \tau_{\Delta F_{\mathrm{vdW}}(t)}}{\tau_{\Delta L_s(t)}} \times 100\%$ where $\tau_{\Delta L_s(t)}$ is the actual cooling time for sample expansion $\Delta L_s(t)$ and $\tau_{\Delta F_{\mathrm{vdW}}(t)}$ is the observed cooling time from the calculated force dynamics, $\Delta F_{\mathrm{vdW}}(t)$. In Figure 5.7, we plot ϵ as a function of $\Delta L_s(t)$ and the cooling time τ_c in the absence (a) and presence (b) of tip expansion (max $\Delta L_{tip} = 3.20$ pm). The dotted lines demarcate the area where the error is less than $\pm 15\%$. As can be seen, in the absence of tip expansion, the error is relatively low over a wide range of experimental parameters. In the presence of tip expansion, the area contracts for lower expansions and shorter cooling times. This indicates some noticeable impact of the tip expansion and its subsequent dynamics, especially for samples that are thinner, exhibit smaller thermal expansion, and feature faster relaxation times.

Nonetheless, the error remains low for a broad range of relevant experimental parameters.

The magnitude of thermal expansion depends not only on the sample thickness but also on the thermal properties of the material. The total expansion, ΔL_s of a sample is related to the maximum temperature rise in the sample, $\Delta T_{s,max}$ and the thickness, d as: [2, 28]

$$\Delta L_s \approx \sigma d \Delta T_{s,max} \tag{5.6}$$

where σ is the linear thermal expansion coefficient and $\Delta T_{s,max} = \frac{P_{abs}}{\rho C V_{heat}} \tau_c$. Here ρ and C are the density and heat capacity of the sample. P_{abs} is the absorbed power which is related to the absorption coefficient a_{abs}, intensity I_{inc} of the incident beam and the heated volume V_{heat} of the sample as $P_{abs} = \int a_{abs} I_{inc} dV_{heat}$. I_{inc} can be derived from the incident beam power and the beam waist. In addition, the sample cooling time τ_c is related to the thickness of the sample, d and its thermal diffusivity D, as $\tau_c = d^2/D$ [2, 39]. From Figure 5.7(b) we can infer that for any ΔL_s and τ_c at the region below the black dotted line in the lower left zone, the thermal effect of the finite tip expansion is no longer negligible. Approximating the dotted line as a straight line, we can denote the region below the line by the following condition:

$$\Delta L_s \left[2.63 \times 10^{10} (\mathrm{m}^{-1})\right] + \frac{d^2}{D} \left[5 \times 10^6 (\mathrm{s}^{-1})\right] <= 1.763 \tag{5.7}$$

If we further assume that the field distribution is uniform over the heated volume, then we can write $\Delta T_{s,max} \approx \frac{a_{abs} I_{inc}}{\rho C} \frac{d^2}{D}$. Using the approximate expression of $\Delta T_{s,max}$ in equation 5.6 we obtain:

$$\Delta L_s \approx \sigma d \frac{a_{abs} I_{inc}}{\rho C} \frac{d^2}{D} \tag{5.8}$$

We can now calculate I_{inc} for the beam power of 1mW and waist of 0.3μm, employing the same parameters as used Section 5.1. We can rewrite the above condition in 5.7 for the

vis/NIR illumination condition at ~ 0.8 μm as:

$$\Big[\frac{\sigma a_{abs}}{\rho C}\big[1.86\times10^{20}(\mathrm{Wm^{-3}})\big]d+\big[5\times10^{6}(\mathrm{s^{-1}})\big]\Big]\frac{d^2}{D}<=1.763 \tag{5.9}$$

The above equality provides an empirical relation between the physical and thermal properties of the sample, and can be used to predict if the effect of finite tip expansion is likely negligible under a given experimental condition. For instance, if we consider a generic material with the representative thermal properties as $D = 2.5\times10^{-7}$ m^2/s, $\rho = 1.05\times10^{3}$ kgm^{-3} and $C = 1200$ J/kg.K, and we assume the specific values of $a_{abs} = 700$ cm^{-1} and $\sigma = 70\times10^{-6}$ /K, then the above condition is satisfied for any thickness lower than $d = 162$ nm. This indicates that the thermal effect of the tip is no longer negligible for a thickness below 160 nm for this material. For organic materials, differences in threshold thickness are strongly determined by a_{abs} and σ. For example, if a_{abs} (or σ) increases by a factor of 4 times, then the thickness threshold decreases to 109 nm. In a similar manner, the thickness threshold increases to 220 nm if a_{abs} (or σ) is decreased by a factor of 4.

We note that the relation in (5.9) is effective for illumination at $\sim 0.8\mu$m and provides a meaningful estimation of the thickness threshold for materials exhibiting an absorptive response around vis/NIR, such as naphthalocyanines [39]. We conclude that above this threshold thickness, the tip effect on the measured PiFM signal is too small to have a significant impact and can thus be safely ignored.

5.5 Summary

In this chapter, we have investigated the laser-induced thermal expansion of a nanoprobe and its subsequent relaxation dynamics. We have performed simulations to determine the rise/fall dynamics of the local temperature at the tip apex and the resulting tip apex ex-

pansion dynamics. Assuming a simple exponential model, we have calculated the apparent cooling time, t_c for the bare silicon and gold-coated silicon nanoprobes. Furthermore, we have complemented our numerically determined t_c with experimental values using the FT-PiFM model. The simulations and analysis predict a tip expansion of several pm and a sub-μs cooling time for a gold-coated silicon tip. We have used the estimated tip expansion parameters to evaluate the effect of light-induced tip expansion on PiFM measurements particularly it's dynamic response. We have found that for thicker samples, the tip expansion delivers no meaningful contribution to the PiFM measurement, as the response is dominated by sample expansion. On the other hand, for thinner samples, the expected thermal expansion of the sample may approach the length scale of the tip expansion, in which case tip expansion can affect the PiFM measurement. In addition, we have provided an empirical relation among the thermal and physical properties of the sample that predicts a threshold thickness beyond which the tip expansion effect can be safely ignored. In general, for a gold-coated tip, the expected expansion is on the order of a few pm, which is generally below the detection limit if the thermal contribution is governed by the thermally modulated van der Waals force.

Bibliography

[1] Prabhat Verma. Tip-enhanced raman spectroscopy: technique and recent advances. *Chemical reviews*, 117(9):6447–6466, 2017.

[2] Junghoon Jahng, Bongsu Kim, and Eun Seong Lee. Quantitative analysis of photoinduced thermal force: Surface and volume responses. *Physical Review B*, 106(15):155424, 2022.

[3] Atsushi Taguchi, Jun Yu, Prabhat Verma, and Satoshi Kawata. Optical antennas with multiple plasmonic nanoparticles for tip-enhanced raman microscopy. *Nanoscale*, 7(41):17424–17433, 2015.

[4] Vincenzo Giannini, Antonio I Fernández-Domínguez, Susannah C Heck, and Stefan A Maier. Plasmonic nanoantennas: fundamentals and their use in controlling the radiative properties of nanoemitters. *Chemical reviews*, 111(6):3888–3912, 2011.

[5] Feng Hao, Yannick Sonnefraud, Pol Van Dorpe, Stefan A Maier, Naomi J Halas, and Peter Nordlander. Symmetry breaking in plasmonic nanocavities: subradiant lspr sensing and a tunable fano resonance. *Nano letters*, 8(11):3983–3988, 2008.

[6] Jonathan A Fan, Chihhui Wu, Kui Bao, Jiming Bao, Rizia Bardhan, Naomi J Halas, Vinothan N Manoharan, Peter Nordlander, Gennady Shvets, and Federico Capasso. Self-assembled plasmonic nanoparticle clusters. *science*, 328(5982):1135–1138, 2010.

[7] Jian Ye, Fangfang Wen, Heidar Sobhani, J Britt Lassiter, Pol Van Dorpe, Peter Nordlander, and Naomi J Halas. Plasmonic nanoclusters: near field properties of the fano resonance interrogated with sers. *Nano letters*, 12(3):1660–1667, 2012.

[8] Jeffrey M McMahon, Anne-Isabelle Henry, Kristin L Wustholz, Michael J Natan, R Griffith Freeman, Richard P Van Duyne, and George C Schatz. Gold nanoparticle dimer plasmonics: finite element method calculations of the electromagnetic enhancement to surface-enhanced raman spectroscopy. *Analytical and bioanalytical chemistry*, 394(7):1819–1825, 2009.

[9] DaJian Wu, ShuMin Jiang, Ying Cheng, and XiaoJun Liu. Fano-like resonance in symmetry-broken gold nanotube dimer. *Optics express*, 20(24):26559–26567, 2012.

[10] Z Shen, L Su, X-C Yuan, and Y-C Shen. Trapping and rotating of a metallic particle trimer with optical vortex. *Applied Physics Letters*, 109(24):241901, 2016.

[11] Andreas Horrer, Yinping Zhang, Davy Gérard, Jérémie Béal, Mathieu Kociak, Jerome Plain, and Renaud Bachelot. Local optical chirality induced by near-field mode interference in achiral plasmonic metamolecules. *Nano Letters*, 20(1):509–516, 2019.

[12] Junsuke Yamanishi, Hyo-Yong Ahn, Hidemasa Yamane, Shun Hashiyada, Hajime Ishihara, Ki Tae Nam, and Hiromi Okamoto. Optical gradient force on chiral particles. *Science advances*, 8(38):eabq2604, 2022.

[13] Yang Zhao, Amr AE Saleh, Marie Anne Van De Haar, Brian Baum, Justin A Briggs, Alice Lay, Olivia A Reyes-Becerra, and Jennifer A Dionne. Nanoscopic control and quantification of enantioselective optical forces. *Nature nanotechnology*, 12(11):1055–1059, 2017.

[14] Ufuk Kilic, Matthew Hilfiker, Alexander Ruder, Rene Feder, Eva Schubert, Mathias Schubert, and Christos Argyropoulos. Broadband enhanced chirality with tunable response in hybrid plasmonic helical metamaterials. *Advanced Functional Materials*, 31(20):2010329, 2021.

[15] Anne-Sophie Lucier, Henrik Mortensen, Yan Sun, and Peter Grütter. Determination of the atomic structure of scanning probe microscopy tungsten tips by field ion microscopy. *Physical Review B*, 72(23):235420, 2005.

[16] J. Mihaljevic, C. Hafner, and A. J. Meixner. Grating enhanced apertureless near-field optical microscopy. *Opt. Express*, 23(14):18401–18414, 2015.

[17] Zhenglong Zhang, Shaoxiang Sheng, Rongming Wang, and Mengtao Sun. Tip-enhanced raman spectroscopy, 2016.

[18] Teng-Xiang Huang, Sheng-Chao Huang, Mao-Hua Li, Zhi-Cong Zeng, Xiang Wang, and Bin Ren. Tip-enhanced raman spectroscopy: tip-related issues. *Analytical and bioanalytical chemistry*, 407(27):8177–8195, 2015.

[19] Gerd Binnig, Calvin F Quate, and Ch Gerber. Atomic force microscope. *Physical review letters*, 56(9):930, 1986.

[20] I Rajapaksa, K Uenal, and H Kumar Wickramasinghe. Image force microscopy of molecular resonance: A microscope principle. *Applied physics letters*, 97(7):073121, 2010.

[21] F Zenhausern, MP O'boyle, and HK Wickramasinghe. Apertureless near-field optical microscope. *Applied Physics Letters*, 65(13):1623–1625, 1994.

[22] Lukas Novotny and Stephan J Stranick. Near-field optical microscopy and spectroscopy with pointed probes. 2006.

[23] L. Novonty and B. Hecht. *Principles of Nano-Optics*. Cambridge University Press, Cambridge, 2012.

[24] Le Wang, Haomin Wang, Dmitri Vezenov, and Xiaoji G Xu. Direct measurement of photoinduced force for nanoscale infrared spectroscopy and chemical-sensitive imaging. *The Journal of Physical Chemistry C*, 122(41):23808–23813, 2018.

[25] Honghua U Yang and Markus B Raschke. Resonant optical gradient force interaction for nano-imaging and-spectroscopy. *New Journal of Physics*, 18(5):053042, 2016.

[26] Brian T O'Callahan, Jun Yan, Fabian Menges, Eric A Muller, and Markus B Raschke. Photoinduced tip–sample forces for chemical nanoimaging and spectroscopy. *Nano letters*, 18(9):5499–5505, 2018.

[27] Mohammad A Almajhadi, Syed Mohammad Ashab Uddin, and H Kumar Wickramasinghe. Observation of nanoscale opto-mechanical molecular damping as the origin of spectroscopic contrast in photo induced force microscopy. *Nature communications*, 11(1):1–9, 2020.

[28] Junghoon Jahng, Eric O. Potma, and Eun Seong Lee. Tip-enhanced thermal expansion force for nanoscale chemical imaging and spectroscopy in photoinduced force microscopy. *Analytical chemistry*, 90(18):11054–11061, 2018.

[29] Jinwei Zeng, Fei Huang, Caner Guclu, Mehdi Veysi, Mohammad Albooyeh, H Kumar Wickramasinghe, and Filippo Capolino. Sharply focused azimuthally polarized beams with magnetic dominance: near-field characterization at nanoscale by photoinduced force microscopy. *ACS Photonics*, 5(2):390–397, 2018.

[30] Fei Huang, Venkata Ananth Tamma, Zahra Mardy, Jonathan Burdett, and H Kumar Wickramasinghe. Imaging nanoscale electromagnetic near-field distributions using optical forces. *Scientific reports*, 5(1):1–12, 2015.

[31] Junghoon Jahng, Jordan Brocious, Dmitry A Fishman, Fei Huang, Xiaowei Li, Venkata Ananth Tamma, H Kumar Wickramasinghe, and Eric Olaf Potma. Gradient and scattering forces in photoinduced force microscopy. *Physical Review B*, 90(15):155417, 2014.

[32] Jinwei Zeng, Mohammad Albooyeh, Mohsen Rajaei, Abid Anjum Sifat, Eric O. Potma, H. Kumar Wickramasinghe, and Filippo Capolino. Photoinduced magnetic force microscopy: Enabling direct and exclusive detection of optical magnetism. arXiv, July 10, 2021. accessed 2022-02-10.

[33] Jinwei Zeng, Mahsa Darvishzadeh-Varcheie, Mohammad Albooyeh, Mohsen Rajaei, Mohammad Kamandi, Mehdi Veysi, Eric O Potma, Filippo Capolino, and HK Wickramasinghe. Exclusive magnetic excitation enabled by structured light illumination in a nanoscale mie resonator. *ACS nano*, 12(12):12159–12168, 2018.

[34] Chiao-Tzu Wang, Bei Jiang, Ya-Wei Zhou, Tian-Wen Jiang, Jian-Hua Liu, Guo-Dong Zhu, and Wen-Bin Cai. Exploiting the surface-enhanced ir absorption effect in the photothermally induced resonance afm-ir technique toward nanoscale chemical analysis. *Analytical chemistry*, 91(16):10541–10548, 2019.

[35] Haomin Wang, Eli Janzen, Le Wang, James H Edgar, and Xiaoji G Xu. Probing mid-infrared phonon polaritons in the aqueous phase. *Nano letters*, 20(5):3986–3991, 2020.

[36] I Rajapaksa and H Kumar Wickramasinghe. Raman spectroscopy and microscopy based on mechanical force detection. *Applied physics letters*, 99(16):161103, 2011.

[37] Junghoon Jahng, Jordan Brocious, Dmitry A Fishman, Steven Yampolsky, Derek Nowak, Fei Huang, Vartkess A Apkarian, H Kumar Wickramasinghe, and Eric Olaf Potma. Ultrafast pump-probe force microscopy with nanoscale resolution. *Applied Physics Letters*, 106(8):083113, 2015.

[38] Bongsu Kim, Ryan Muhammad Khan, Alexander Fast, Dmitry A Fishman, and Eric O Potma. Nanoscale excitation dynamics of carbon nanotubes probed with photoinduced force microscopy. *The Journal of Physical Chemistry C*, 124(21):11694–11700, 2020.

[39] Bongsu Kim, Junghoon Jahng, Abid Sifat, Eun Seong Lee, and Eric O Potma. Monitoring fast thermal dynamics at the nanoscale through frequency domain photoinduced force microscopy. *The Journal of Physical Chemistry C*, 125(13):7276–7286, 2021.

[40] KL Andrew Chan and Sergei G Kazarian. Tip-enhanced raman mapping with top-illumination afm. *Nanotechnology*, 22(17):175701, 2011.

[41] Natalia Martin Sabanes, Leonie MA Driessen, and Katrin F Domke. Versatile side-illumination geometry for tip-enhanced raman spectroscopy at solid/liquid interfaces. *Analytical chemistry*, 88(14):7108–7114, 2016.

[42] Houkai Chen, Yuquan Zhang, Yanmeng Dai, Changjun Min, Siwei Zhu, and Xiaocong Yuan. Facilitated tip-enhanced raman scattering by focused gap-plasmon hybridization. *Photonics Research*, 8(2):103–109, 2020.

[43] Chi Chen, Norihiko Hayazawa, and Satoshi Kawata. A 1.7 nm resolution chemical analysis of carbon nanotubes by tip-enhanced raman imaging in the ambient. *Nature communications*, 5(1):1–5, 2014.

[44] SS Kharintsev, GG Hoffmann, PS Dorozhkin, J Loos, et al. Atomic force and shear force based tip-enhanced raman spectroscopy and imaging. *Nanotechnology*, 18(31):315502, 2007.

[45] Milton Kerker. Estimation of surface-enhanced raman scattering from surface-averaged electromagnetic intensities. *Journal of colloid and interface science*, 118(2):417–421, 1987.

[46] E. D. Palik. *Handbook of Optical Constants of Solids*. Academic, New York, 1984.

[47] R. J. Hermann and M. J. Gordon. Quantitative comparison of plasmon resonances and field enhancements of near-field optical antennae using fdtd simulations. *Opt. Express*, 26(21):27668–27682, 2018.

[48] W. A Zhang, X. Cui, and O. J. F. Martin. Local field enhancement of an infinite conical metal tip illuminated by a focused beam. *J. Raman Spectrosc.*, 40(10):1338–1342, 2009.

[49] A. Taflove. *Computational Electromagnetics: The Finite-Difference Time-Domain Method*. Artech House, Boston, 2005.

[50] H. Shen, G. Lu, Y. He, Y. Cheng, H. Liub, and Q. Gong. Directional and enhanced spontaneous emission with a corrugated metal probe. *Nanoscale*, 6:7512–7518, 2014.

[51] Yves Martin, Clayton C Williams, and H Kumar Wickramasinghe. Atomic force microscope–force mapping and profiling on a sub 100-å scale. *Journal of applied Physics*, 61(10):4723–4729, 1987.

[52] Junghoon Jahng, Bongsu Kim, Eun Seong Lee, and Eric Olaf Potma. Quantitative analysis of sideband coupling in photoinduced force microscopy. *Physical Review B*, 94(19):195407, 2016.

[53] Junghoon Jahng, Faezeh Tork Ladani, Ryan Muhammad Khan, Xiaowei Li, Eun Seong Lee, and Eric Olaf Potma. Visualizing surface plasmon polaritons by their gradient force. *Optics letters*, 40(21):5058–5061, 2015.

[54] Thejaswi U. Tumkur, Xiao Yang, Benjamin Cerjan, Naomi J. Halas, Peter Nordlander, and Isabell Thomann. Photoinduced force mapping of plasmonic nanostructures. *Nano Letters*, 16(12):7942–7949, 2016.

[55] Antonio Ambrosio, Michele Tamagnone, Kundan Chaudhary, Luis A Jauregui, Philip Kim, William L Wilson, and Federico Capasso. Selective excitation and imaging of ultraslow phonon polaritons in thin hexagonal boron nitride crystals. *Light: Science & Applications*, 7(27):1–9, 2018.

[56] Michele Tamagnone, Antonio Ambrosio, Kundan Chaudhary, Luis A. Jauregui, Philip Kim, William L. Wilson, and Federico Capasso. Ultra-confined mid-infrared resonant phonon polaritons in van der waals nanostructures. *Science Advances*, 4(6):eaat7189, 2018.

[57] Faezeh Tork Ladani and Eric Olaf Potma. Dyadic green's function formalism for photoinduced forces in tip-sample nanojunctions. *Physical Review B*, 95(20):205440, 2017.

[58] Alexandre Dazzi, F Glotin, and R Carminati. Theory of infrared nanospectroscopy by photothermal induced resonance. *Journal of Applied Physics*, 107(12):124519, 2010.

[59] Feng Lu, Mingzhou Jin, and Mikhail A Belkin. Tip-enhanced infrared nanospectroscopy via molecular expansion force detection. *Nature photonics*, 8(4):307–312, 2014.

[60] Junghoon Jahng, Eric O Potma, and Eun Seong Lee. Nanoscale spectroscopic origins of photoinduced tip–sample force in the midinfrared. *Proceedings of the National Academy of Sciences*, 116(52):26359–26366, 2019.

[61] Abid Anjum Sifat, Junghoon Jahng, and Eric O Potma. Photo-induced force microscopy (pifm)–principles and implementations. *Chemical Society Reviews*, 2022.

[62] Jungseok Chae, Sangmin An, Georg Ramer, Vitalie Stavila, Glenn Holland, Yohan Yoon, A Alec Talin, Mark Allendorf, Vladimir A Aksyuk, and Andrea Centrone. Nanophotonic atomic force microscope transducers enable chemical composition and thermal conductivity measurements at the nanoscale. *Nano letters*, 17(9):5587–5594, 2017.

[63] S. Berweger, J. M. Atkin, R. L. Olmon, and M. B. Raschke. Adiabatic tip-plasmon focusing for nano-raman spectroscopy. *J. Phys. Chem. Lett.*, 1(24):3427–3432, 2010.

[64] A. Capaccio, A. Sasso, O. Tarallo, and G. Rusciano. Coral-like plasmonic probes for tip-enhanced raman spectroscopy. *Nanoscale*, 2020.

[65] L. Zhu, C. Georgi, M. Hecker, J. Rinderknecht, A. Mai, Y. Ritz, and E. Zschech. Nano-raman spectroscopy with metallized atomic force microscopy tips on strained silicon structures. *J. Appl. Phys.*, 101(10):104305, 2007.

[66] L. Xiao, K. A. Bailey, Hao Wang, and Zachary D S. Probing membrane receptor-ligand specificity with surface-and tip-enhanced raman scattering. *Anal. Chem.*, 89(17):9091–9099, 2017.

[67] P. Y. Hung, T. E O'Loughlin, A. Lewis, R. Dechter, M. Samayoa, S. Banerjee, E. L. Wood, and A. R. H. Walker. Potential application of tip-enhanced raman spectroscopy (ters) in semiconductor manufacturing. In *Metrology, Inspection, and Process Control for Microlithography XXIX*, volume 9424, page 94241S. International Society for Optics and Photonics, 2015.

[68] A. Taguchi, J. Yu, P. Verma, and S Kawata. Optical antennas with multiple plasmonic nanoparticles for tip-enhanced raman microscopy. *Nanoscale*, 7:17424–17433, 2015.

[69] D. Sadiq, J. Shirdel, J. S. Lee, E. Selishcheva, N. Park, and C. Lienau. Adiabatic nanofocusing scattering-type optical nanoscopy of individual gold nanoparticles. *Nano Lett.*, 11(4):1609–1613, 2011.

[70] S. Berweger, J. M. Atkin, R. L. Olmon, and M. B. Raschke. Light on the tip of a needle: Plasmonic nanofocusing for spectroscopy on the nanoscale. *J. Phys. Chem. Lett.*, 3(7):945–952, 2012.

[71] H. Shen, G. Lu, Z. Cao, Y. He, Y. Cheng, J. Li, Z. Li, and Q. Gong. Directionally enhanced probe for side-illumination tip enhanced spectroscopy. *J. Raman Spectrosc.*, 47(10):1194–1199, 2016.

[72] F. Lu, W. Zhang, J. Zhang, M. Liu, L. Zhang, T. Xue, C. Meng, F. Gao, T. Mei, and J. Zhao. Grating-assisted coupling enhancing plasmonic tip nanofocusing illuminated via radial vector beam. *Nanophotonics*, 8(12):2303–2311, 2019.

[73] A. Weber-Bargioni, A. Schwartzberg, M. Cornaglia, A. Ismach, J. J. Urban, Y. Pang, R. Gordon, J. Bokor, M. B. Salmeron, D. F. Ogletree, P. Ashby, S. Cabrini, and P. J. Schuck. Hyperspectral nanoscale imaging on dielectric substrates with coaxial optical antenna scan probes. *Nano Lett.*, 11(3):1201–1207, 2011.

[74] S. S. Choi, M. J. Park, C. H. Han, S. J. Oh, S. H. Han, N. K. Park, Y. Kim, and H. Choo. Fabrication of pyramidal probes with various periodic patterns and a single nanopore. *J. Vac. Sci. Technol., B*, 33(6):06F203, 2015.

[75] X. Wang, Z. Liu, M. Zhuang, H. Zhang, X. Wang, Z. Xie, D. Wu, B. Ren, and Z. Tian. Tip-enhanced raman spectroscopy for investigating adsorbed species on a single-crystal surface using electrochemically prepared au tips. *Appl. Phys. Lett.*, 91(10):101105, 2007.

[76] R. Stöckle, C. Fokas, V. Deckert, R. Zenobi, B. Sick, B. Hecht, and U. P. Wild. High-quality near-field optical probes by tube etching. *Appl. Phys. Lett.*, 75(2):160–162, 1999.

[77] F. Bonaccorso, G. Calogero, G. Di Marco, O. M. Maragò, P. G. Gucciardi, U. Giorgianni, K. Channon, and G. Sabatino. Pfabrication of gold tips by chemical etching in aqua regia. *Rev. Sci. Instrum.*, 78(10):103702, 2007.

[78] L. Eligal, F. Culfaz, V. McCaughan, N. I. Cade, and D. Richards. Etching gold tips suitable for tip-enhanced near-field optical microscopy. *Rev. Sci. Instrum.*, 80(3):033701, 2009.

[79] S. S. Kharintsev, A. I. Noskov, G. G. Hoffmann, and J. Loos. Near-field optical taper antennas fabricated with a highly replicable ac electrochemical etching method. *Nanotechnology*, 22(2):025202, dec 2010.

[80] S. Kharintsev, A. Alekseev, V. Vasilchenko, A. Kharitonov, and M. Salakhov. Electrochemical design of plasmonic nanoantennas for tip-enhanced optical spectroscopy and imaging performance. *Opt. Mater. Express*, 5(10):2225–2230, Oct 2015.

[81] H. Miranda, C. Rabelo, T. L. Vasconcelos, L. Gustavo Cançado, and A. Jorio. Optical properties of plasmon-tunable tip pyramids for tip-enhanced raman spectroscopy. *Phys. Status Solidi RRL*, 14(9):2000212, 2020.

[82] I. Song, Y. Peter, and M. Meunier. Smoothing dry-etched microstructure sidewalls using focused ion beam milling for optical applications. *J. Micromech. Microeng.*, 17(8):1593–1597, 2007.

[83] H. Kollmann, X. Piao, M. Esmann, S. F. Becker, D. Hou, C. Huynh, L. Kautschor, G. Bösker, H. Vieker, A. Beyer, A. Gölzhäuser, N. Park, R. Vogelgesang, M. Silies, and C. Lienau. Toward plasmonics with nanometer precision: Nonlinear optics of helium-ion milled gold nanoantennas. *Nano Lett.*, 14(8):4778–4784, 2014.

[84] Abid Anjum Sifat and Eric O Potma. Optimizing the near-field and far-field properties of tips in tip-enhanced raman scattering. *Journal of Raman Spectroscopy*, 52(12):2018–2028, 2021.

[85] C. Ropers, C. C. Neacsu, T. Elsaesser, M. Albrecht, M. B. Raschke, and C. Lienau. Grating-coupling of surface plasmons onto metallic tips: A nanoconfined light source. *Nano Lett.*, 7(9):2784–2788, 2007.

[86] K. Hagita, T. Higuchi, and H. Jinnai. Super-resolution for asymmetric resolution of fib-sem 3d imaging using ai with deep learning. *Sci. Rep.*, 8:5877, 2018.

[87] P. W. Barber, R. K. Chang, and H. Massoudi. Electrodynamic calculations of the surface-enhanced electric intensities on large ag spheroids. *Phys. Rev. B*, 27(12):7251, 1983.

[88] H. Aouani, O. Mahboub, E. Devaux, H. Rigneault, T. W. Ebbesen, and J. Wenger. Plasmonic antennas for directional sorting of fluorescence emission. *Nano Lett.*, 11(6):2400–2406, 2011.

[89] Abid Anjum Sifat, Filippo Capolino, and Eric O Potma. Force detection of electromagnetic chirality of tightly focused laser beams. *ACS Photonics*, 9(8):2660–2667, 2022.

[90] Konstantin Y Bliokh, Aleksandr Y Bekshaev, and Franco Nori. Dual electromagnetism: helicity, spin, momentum and angular momentum. *New Journal of Physics*, 15(3):033026, 2013.

[91] Robert P Cameron, Stephen M Barnett, and Alison M Yao. Optical helicity, optical spin and related quantities in electromagnetic theory. *New Journal of Physics*, 14(5):053050, 2012.

[92] Mina Hanifeh, Mohammad Albooyeh, and Filippo Capolino. Helicity maximization below the diffraction limit. *Physical Review B*, 102(16):165419, 2020.

[93] Jose L Trueba and Antonio F Ranada. The electromagnetic helicity. *European Journal of Physics*, 17(3):141, 1996.

[94] Mina Hanifeh, Mohammad Albooyeh, and Filippo Capolino. Optimally chiral light: Upper bound of helicity density of structured light for chirality detection of matter at nanoscale. *ACS Photonics*, 7(10):2682–2691, 2020.

[95] Konstantin Y Bliokh and Franco Nori. Characterizing optical chirality. *Physical Review A*, 83(2):021803, 2011.

[96] Stephen M Barnett. Rotation of electromagnetic fields and the nature of optical angular momentum. *Journal of modern optics*, 57(14-15):1339–1343, 2010.

[97] Yiqiao Tang and Adam E Cohen. Optical chirality and its interaction with matter. *Physical review letters*, 104(16):163901, 2010.

[98] Yiqiao Tang and Adam E Cohen. Enhanced enantioselectivity in excitation of chiral molecules by superchiral light. *Science*, 332(6027):333–336, 2011.

[99] Yang Zhao, Amr AE Saleh, and Jennifer A Dionne. Enantioselective optical trapping of chiral nanoparticles with plasmonic tweezers. *Acs Photonics*, 3(3):304–309, 2016.

[100] Maxim V Gorkunov, Alexander N Darinskii, and Alexey V Kondratov. Enhanced sensing of molecular optical activity with plasmonic nanohole arrays. *JOSA B*, 34(2):315–320, 2017.

[101] Alexander O Govorov, Zhiyuan Fan, Pedro Hernandez, Joseph M Slocik, and Rajesh R Naik. Theory of circular dichroism of nanomaterials comprising chiral molecules and nanocrystals: plasmon enhancement, dipole interactions, and dielectric effects. *Nano letters*, 10(4):1374–1382, 2010.

[102] Alexander O Govorov. Plasmon-induced circular dichroism of a chiral molecule in the vicinity of metal nanocrystals. application to various geometries. *The Journal of Physical Chemistry C*, 115(16):7914–7923, 2011.

[103] David B Amabilino. *Chirality at the nanoscale: nanoparticles, surfaces, materials and more*. John Wiley & Sons, 2009.

[104] Chi-Sing Ho, Aitzol Garcia-Etxarri, Yang Zhao, and Jennifer Dionne. Enhancing enantioselective absorption using dielectric nanospheres. *ACS Photonics*, 4(2):197–203, 2017.

[105] Mina Hanifeh and Filippo Capolino. Helicity maximization in a planar array of achiral high-density dielectric nanoparticles. *Journal of Applied Physics*, 127(9):093104, 2020.

[106] KG Lee, HW Kihm, JE Kihm, WJ Choi, H Kim, C Ropers, DJ Park, YC Yoon, SB Choi, DH Woo, et al. Vector field microscopic imaging of light. *Nature Photonics*, 1(1):53–56, 2007.

[107] T Grosjean, IA Ibrahim, MA Suarez, GW Burr, Mathieu Mivelle, and D Charraut. Full vectorial imaging of electromagnetic light at subwavelength scale. *Optics Express*, 18(6):5809–5824, 2010.

[108] B Le Feber, N Rotenberg, Daryl M Beggs, and L Kuipers. Simultaneous measurement of nanoscale electric and magnetic optical fields. *Nature Photonics*, 8(1):43–46, 2014.

[109] Thomas Bauer, Sergej Orlov, Ulf Peschel, Peter Banzer, and Gerd Leuchs. Nanointerferometric amplitude and phase reconstruction of tightly focused vector beams. *Nature Photonics*, 8(1):23–27, 2014.

[110] M Nieto-Vesperinas, JJ Sáenz, R Gómez-Medina, and L Chantada. Optical forces on small magnetodielectric particles. *Optics express*, 18(11):11428–11443, 2010.

[111] Arthur D Yaghjian. Electromagnetic forces on point dipoles. In *IEEE Antennas and Propagation Society International Symposium. 1999 Digest. Held in conjunction with: USNC/URSI National Radio Science Meeting (Cat. No. 99CH37010)*, volume 4, pages 2868–2871. IEEE, 1999.

[112] C. Tai, IEEE Antennas, Propagation Society, IEEE Microwave Theory, and Techniques Society. *Dyadic Green Functions in Electromagnetic Theory*. IEEE Press Publication Series. IEEE Press, 1994.

[113] S. B. Wang and C. T. Chan. Lateral optical force on chiral particles near a surface. *Nature Communications*, 5(1):1–8, March 2014.

[114] Mohammad Kamandi, Mohammad Albooyeh, Caner Guclu, Mehdi Veysi, Jinwei Zeng, Kumar Wickramasinghe, and Filippo Capolino. Enantiospecific detection of chiral nanosamples using photoinduced force. *Physical Review Applied*, 8(6):064010, 2017.

[115] Mohammad Kamandi, Mohammad Albooyeh, Mehdi Veysi, Mohsen Rajaei, Jinwei Zeng, H Kumar Wickramasinghe, and Filippo Capolino. Unscrambling structured chirality with structured light at the nanoscale using photoinduced force. *ACS Photonics*, 5(11):4360–4370, 2018.

[116] A. Serdyukov, I. Semchenko, S. Tertyakov, and A. Sihvola. *Electromagnetics of bi-anisotropic materials - Theory and Application*, volume 11 of *Electrocomponent Science Monographs*. Gordon and Breach Science Publishers, 2001.

[117] John David Jackson. *Classical electrodynamics*. John Wiley & Sons, 1975.

[118] Salvatore Campione, Michael B Sinclair, and Filippo Capolino. Effective medium representation and complex modes in 3d periodic metamaterials made of cubic resonators with large permittivity at mid-infrared frequencies. *Photonics and Nanostructures-Fundamentals and Applications*, 11(4):423–435, 2013.

[119] Craig F Bohren. Univ. of arizona, dept. of physics. *Light Scattering by Irregularly Shaped Particles*, page 103, 2012.

[120] David E Aspnes and AA Studna. Dielectric functions and optical parameters of si, ge, gap, gaas, gasb, inp, inas, and insb from 1.5 to 6.0 ev. *Physical review B*, 27(2):985, 1983.

[121] Rfaqat Ali, Felipe A Pinheiro, Rafael S Dutra, Felipe SS Rosa, and Paulo A Maia Neto. Enantioselective manipulation of single chiral nanoparticles using optical tweezers. *Nanoscale*, 12(8):5031–5037, 2020.

[122] Rfaqat Ali, FA Pinheiro, RS Dutra, FSS Rosa, and PA Maia Neto. Probing the optical chiral response of single nanoparticles with optical tweezers. *JOSA B*, 37(9):2796–2803, 2020.

[123] Milton Kerker, D-S Wang, and CL Giles. Electromagnetic scattering by magnetic spheres. *JOSA*, 73(6):765–767, 1983.

[124] Jeng Yi Lee, Andrey E Miroshnichenko, and Ray-Kuang Lee. Reexamination of kerker's conditions by means of the phase diagram. *Physical Review A*, 96(4):043846, 2017.

[125] M Nieto-Vesperinas, PC Chaumet, and Adel Rahmani. Near-field photonic forces. *Philosophical Transactions of the Royal Society of London. Series A: Mathematical, Physical and Engineering Sciences*, 362(1817):719–737, 2004.

[126] Ping Chu and D. L. Mills. Laser-induced forces in metallic nanosystems: The role of plasmon resonances. *Phys. Rev. Lett.*, 99:127401, Sep 2007.

[127] Junsuke Yamanishi, Hidemasa Yamane, Yoshitaka Naitoh, Yan Jun Li, Nobuhiko Yokoshi, Tatsuya Kameyama, Seiya Koyama, Tsukasa Torimoto, Hajime Ishihara, and Yasuhiro Sugawara. Optical force mapping at the single-nanometre scale. *Nature Communications*, 12(1):1–7, 2021.

[128] Christophe Caloz and Ari Sihvola. Electromagnetic chirality, part 1: the microscopic perspective [electromagnetic perspectives]. *IEEE Antennas and Propagation Magazine*, 62(1):58–71, 2020.

[129] Steven T Yang, Manyalibo J Matthews, Selim Elhadj, Diane Cooke, Gabriel M Guss, Vaughn G Draggoo, and Paul J Wegner. Comparing the use of mid-infrared versus far-infrared lasers for mitigating damage growth on fused silica. *Applied Optics*, 49(14):2606–2616, 2010.

[130] Martin A Green and Mark J Keevers. Optical properties of intrinsic silicon at 300 k. *Progress in Photovoltaics: Research and applications*, 3(3):189–192, 1995.

[131] Peter B Johnson and R-WJPrB Christy. Optical constants of the noble metals. *Physical review B*, 6(12):4370, 1972.

[132] R Kojima Endo, Yusuke Fujihara, and Masahiro Susa. Calculation of the density and heat capacity of silicon by molecular dynamics simulation. *High Temp. High Press*, 35(36):5, 2003.

[133] Chandra Prakash. Thermal conductivity variation of silicon with temperature. *Microelectronics Reliability*, 18(4):333, 1978.

[134] LB Pankratz. *Thermodynamic properties of elements and oxides*. Number 672. US Department of the Interior, Bureau of Mines, 1982.

[135] Cho Yen Ho, Reginald W Powell, and Peter E Liley. Thermal conductivity of the elements. *Journal of Physical and Chemical Reference Data*, 1(2):279–421, 1972.

[136] Robert Joseph Corruccini and John J Gniewek. *Thermal expansion of technical solids at low temperatures: A compilation from the literature*, volume 29. US Department of Commerce, National Bureau of Standards, 1961.

[137] WC Ang, P Kropelnicki, Oak Soe, JHL Ling, AB Randles, AJW Hum, JML Tsai, AAO Tay, KC Leong, and CS Tan. Novel development of the micro-tensile test at elevated temperature using a test structure with integrated micro-heater. *Journal of Micromechanics and Microengineering*, 22(8):085015, 2012.

[138] S Sakai, H Tanimoto, K Otsuka, T Yamada, Y Koda, E Kita, and H Mizubayashi. Elastic behaviors of high density nanocrystalline gold prepared by gas deposition method. *Scripta materialia*, 45(11):1313–1319, 2001.

[139] Yasumasa Okada and Yozo Tokumaru. Precise determination of lattice parameter and thermal expansion coefficient of silicon between 300 and 1500 k. *Journal of applied physics*, 56(2):314–320, 1984.

[140] FC Nix and D MacNair. The thermal expansion of pure metals: copper, gold, aluminum, nickel, and iron. *Physical Review*, 60(8):597, 1941.

[141] J Dolbow and M Gosz. Effect of out-of-plane properties of a polyimide film on the stress fields in microelectronic structures. *Mechanics of materials*, 23(4):311–321, 1996.

[142] Stephen Martin Collard and RB McLellan. High-temperature elastic constants of gold single-crystals. *Acta metallurgica et materialia*, 39(12):3143–3151, 1991.

[143] Pisidhi Karasudhi. *Foundations of solid mechanics*, volume 3. Taylor & Francis, 1991.

[144] Jungho Mun, Minkyung Kim, Younghwan Yang, Trevon Badloe, Jincheng Ni, Yang Chen, Cheng-Wei Qiu, and Junsuk Rho. Electromagnetic chirality: from fundamentals to nontraditional chiroptical phenomena. *Light: Science & Applications*, 9(1):1–18, 2020.

[145] Christophe Caloz and Ari Sihvola. Electromagnetic chirality, part 2: the macroscopic perspective [electromagnetic perspectives]. *IEEE Antennas and Propagation Magazine*, 62(2):82–98, 2020.

[146] Alessandro Ciattoni. Mirror optical activity: Nanophotonic chiral sensing from parity indefiniteness. *Physical Review Applied*, 16(3):034041, 2021.

[147] Lisa V Poulikakos, Jennifer A Dionne, and Aitzol García-Etxarri. Optical helicity and optical chirality in free space and in the presence of matter. *Symmetry*, 11(9):1113, 2019.

Appendix A

Detailed derivation of Eq. 4.16 and 4.17

A.1 Image theorem for a chiral object in dipole approximation

In the dipole approximation, we can model the chiral tip in terms of an electric and magnetic dipole. The moments of the point dipoles are defined in equations A.1 and A.2. The term α_{em} provides the relation between the electric dipole and the inducing magnetic field, as well as the magnetic dipole and the inducing electric field. In addition, α_{em} provides a microscopic measure of the chirality of the nano object and its given handedness.[94] Since we can assume that the chiral tip is nonmagnetic (as a good approximation), the magnetic dipole is produced by a circulating displacement current, which is on the macroscopic level made possible by the structural chiral feature of the object (i.e., the tip).[32, 13] We also assume that, for simplicity, the image principle provided by the substrate is the same as that of an electric mirror.

We consider now a chiral object described in terms of its electric and magnetic dipoles,

$$\mathbf{p}_{tip} = \alpha_{ee}\mathbf{E}^{loc}(\mathbf{r}_{tip}) + \alpha_{em}\mathbf{H}^{loc}(\mathbf{r}_{tip}) \tag{A.1}$$

$$\mathbf{m}_{tip} = -\mu_0^{-1}\alpha_{em}\mathbf{E}^{loc}(\mathbf{r}_{tip}) + \alpha_{mm}\mathbf{H}^{loc}(\mathbf{r}_{tip}) \tag{A.2}$$

Since, the dipoles are induced dipole, the image dipole moments can be found by applying the reflection rules for the electric and magnetic field components. Besides, the chiral dipole moments have contributions from terms proportional to α_{em}, which, as stated above, is a microscopic measure of the object's chirality. Since the mirror image of a chiral object is the same object of opposite handedness, these terms must thus reflect according to $\alpha_{em}^{img} \rightarrow -\alpha_{em}$ [144, 145, 146]. Thus using the proper reflections of the field components as equations [147] $E_x^{loc}(\mathbf{r}_{img}) = -E_x^{loc}(\mathbf{r}_{tip})$, $E_y^{loc}(\mathbf{r}_{img}) = -E_y^{loc}(\mathbf{r}_{tip})$, $E_z^{loc}(\mathbf{r}_{img}) = E_z^{loc}(\mathbf{r}_{tip})$, $H_x^{loc}(\mathbf{r}_{img}) = H_x^{loc}(\mathbf{r}_{tip})$, $H_y^{loc}(\mathbf{r}_{img}) = H_y^{loc}(\mathbf{r}_{tip})$ and $H_z^{loc}(\mathbf{r}_{img}) = -H_z^{loc}(\mathbf{r}_{tip})$ along with $\alpha_{em}^{img} = -\alpha_{em}$, we get the image dipole moments as equations (A.3-A.8)

$$p_{img,x} = \alpha_{ee}E_x^{loc}(\mathbf{r}_{img}) - \alpha_{em}H_x^{loc}(\mathbf{r}_{img}) \tag{A.3}$$

$$p_{img,y} = \alpha_{ee}E_y^{loc}(\mathbf{r}_{img}) - \alpha_{em}H_y^{loc}(\mathbf{r}_{img}) \tag{A.4}$$

$$p_{img,z} = \alpha_{ee}E_z^{loc}(\mathbf{r}_{img}) - \alpha_{em}H_z^{loc}(\mathbf{r}_{img}) \tag{A.5}$$

$$m_{img,x} = \mu_0^{-1}\alpha_{em}E_x^{loc}(\mathbf{r}_{img}) + \alpha_{mm}H_x^{loc}(\mathbf{r}_{img}) \tag{A.6}$$

$$m_{img,y} = \mu_0^{-1}\alpha_{em}E_y^{loc}(\mathbf{r}_{img}) + \alpha_{mm}H_y^{loc}(\mathbf{r}_{img}) \tag{A.7}$$

$$m_{img,z} = \mu_0^{-1}\alpha_{em}E_z^{loc}(\mathbf{r}_{img}) + \alpha_{mm}H_z^{loc}(\mathbf{r}_{img}) \tag{A.8}$$

To simplify, same magnitude of the polarizabilities has been used for the image and tip dipole. Upon comparison of the image dipole moments with the tip dipole moments and considering the relation between the field components at the two positions ($\mathbf{r}_{tip}$ and $\mathbf{r}_{img}$) through reflections, we find $p_{img,x} = -p_{tip,x}$, $p_{img,y} = -p_{tip,y}$, $p_{img,z} = p_{tip,z}$, $m_{img,x} = m_{tip,x}$, $m_{img,y} = m_{tip,y}$ and $m_{img,z} = -m_{tip,z}$. These relations comply with the image rules for the

conventional electric and magnetic dipole where the image of a vertical electric dipole or a tangential magnetic dipole is identical to the dipole moment of the original [29] and the image of a tangential electric dipole or a vertical magnetic dipole, is similar in magnitude to its original but displays opposite polarity[32].

A.2 Derivation

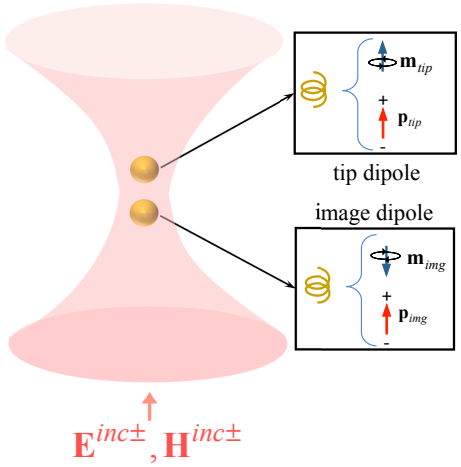

Figure A.1: Substituting the effect of substrate by image dipole theory with electric and magnetic dipole moment having proper sign.

According to image dipole theory, we replaced the effect of substrate by an image dipole as shown in figure A.1. As discussed in section $A.1$, the image dipole follow particular sign convention for tangential and vertical orientations. The local electric and magnetic field at the tip location, $\mathbf{E}^{loc}(\mathbf{r}_{tip})$ and $\mathbf{H}^{loc}(\mathbf{r}_{tip})$ can be expressed in terms of incident field($\mathbf{E}^{inc}(\mathbf{r}_{tip}), \mathbf{H}^{inc}(\mathbf{r}_{tip})$), image dipole moments($\mathbf{p}_{img}, \mathbf{m}_{img}$) and green's function($\underline{\mathbf{G}}^{ee}(\mathbf{r})$, $\underline{\mathbf{G}}^{em}(\mathbf{r})$, $\underline{\mathbf{G}}^{me}(\mathbf{r})$, $\underline{\mathbf{G}}^{mm}(\mathbf{r})$) as shown in chapter 4. We start by defining the image dipole moments as equations A.9 and A.10.

$$\mathbf{p}_{img} = \alpha_{ee}\mathbf{E}^{loc}(\mathbf{r}_{img}) + \alpha_{em}\mathbf{H}^{loc}(\mathbf{r}_{img}) \tag{A.9}$$

$$\mathbf{m}_{img} = -\mu_0^{-1}\alpha_{em}\mathbf{E}^{loc}(\mathbf{r}_{img}) + \alpha_{mm}\mathbf{H}^{loc}(\mathbf{r}_{img}) \tag{A.10}$$

First, we need to find the expressions of all six components of $\mathbf{p}_{img}$ and $\mathbf{m}_{img}$ in terms of incident beam and polarizabilities of the tip. To do that, we figure out the six linear equations relating all these six components. At first, let's work on $\mathbf{p}_{img}$, We can rewrite Eq. A.9 using the explicit form of $\mathbf{E}^{loc}$ and $\mathbf{H}^{loc}$ as:

$$\begin{aligned}
\mathbf{p}_{img} &= \alpha_{ee}[\mathbf{E}^{inc}(\mathbf{r}_{img}) + \mathbf{E}^{sca}_{tip\to img}(\mathbf{r}_{img})] + \alpha_{em}[\mathbf{H}^{inc}(\mathbf{r}_{img}) + \mathbf{H}^{sca}_{tip\to img}(\mathbf{r}_{img})] \\
\mathbf{p}_{img} &= \alpha_{ee}\mathbf{E}^{inc}(\mathbf{r}_{img}) + \alpha_{ee}\underline{\mathbf{G}}^{ee}(\mathbf{r}_{img} - \mathbf{r}_{tip}) \cdot \mathbf{p}_{tip} + \alpha_{ee}\underline{\mathbf{G}}^{em}(\mathbf{r}_{img} - \mathbf{r}_{tip}) \cdot \mathbf{m}_{tip} \\
&\quad + \alpha_{em}\mathbf{H}^{inc}(\mathbf{r}_{img}) + \alpha_{em}\underline{\mathbf{G}}^{me}(\mathbf{r}_{img} - \mathbf{r}_{tip}) \cdot \mathbf{p}_{tip} + \alpha_{em}\underline{\mathbf{G}}^{mm}(\mathbf{r}_{img} - \mathbf{r}_{tip}) \cdot \mathbf{m}_{tip}
\end{aligned}$$

Now using A.1 and A.2 we can rewrite the above equation as shown below.

$$\begin{aligned}
\mathbf{p}_{img} &= \alpha_{ee}\mathbf{E}^{inc}(\mathbf{r}_{img}) + \alpha_{em}\mathbf{H}^{inc}(\mathbf{r}_{img}) \\
&\quad + \alpha_{ee}\underline{\mathbf{G}}^{ee}(\mathbf{r}_{img} - \mathbf{r}_{tip}) \cdot (\alpha_{ee}\mathbf{E}^{loc}(\mathbf{r}_{tip}) + \alpha_{em}\mathbf{H}^{loc}(\mathbf{r}_{tip})) \\
&\quad + \alpha_{ee}\underline{\mathbf{G}}^{em}(\mathbf{r}_{img} - \mathbf{r}_{tip}) \cdot (-\mu_0^{-1}\alpha_{em}\mathbf{E}^{loc}(\mathbf{r}_{tip}) + \alpha_{mm}\mathbf{H}^{loc}(\mathbf{r}_{tip})) \\
&\quad + \alpha_{em}\underline{\mathbf{G}}^{me}(\mathbf{r}_{img} - \mathbf{r}_{tip}) \cdot (\alpha_{ee}\mathbf{E}^{loc}(\mathbf{r}_{tip}) + \alpha_{em}\mathbf{H}^{loc}(\mathbf{r}_{tip})) \\
&\quad + \alpha_{em}\underline{\mathbf{G}}^{mm}(\mathbf{r}_{img} - \mathbf{r}_{tip}) \cdot (-\mu_0^{-1}\alpha_{em}\mathbf{E}^{loc}(\mathbf{r}_{tip}) + \alpha_{mm}\mathbf{H}^{loc}(\mathbf{r}_{tip}))
\end{aligned} \tag{A.11}$$

$$
\begin{aligned}
\mathbf{p}_{img} &= \alpha_{ee}\mathbf{E}^{inc}(\mathbf{r}_{img}) + \alpha_{em}\mathbf{H}^{inc}(\mathbf{r}_{img}) \\
&+ \Big[\alpha_{ee}^2\underline{\mathbf{G}}^{ee}(\mathbf{r}_{img}-\mathbf{r}_{tip}) - \mu_0^{-1}\alpha_{em}\alpha_{ee}\underline{\mathbf{G}}^{em}(\mathbf{r}_{img}-\mathbf{r}_{tip}) \\
&+ \alpha_{ee}\alpha_{em}\underline{\mathbf{G}}^{me}(\mathbf{r}_{img}-\mathbf{r}_{tip}) - \mu_0^{-1}\alpha_{em}^2\underline{\mathbf{G}}^{mm}(\mathbf{r}_{img}-\mathbf{r}_{tip})\Big]\cdot\mathbf{E}^{inc}(\mathbf{r}_{tip}) \\
&+ \Big[\alpha_{ee}\alpha_{em}\underline{\mathbf{G}}^{ee}(\mathbf{r}_{img}-\mathbf{r}_{tip}) + \alpha_{ee}\alpha_{mm}\underline{\mathbf{G}}^{em}(\mathbf{r}_{img}-\mathbf{r}_{tip}) \\
&+ \alpha_{em}^2\underline{\mathbf{G}}^{me}(\mathbf{r}_{img}-\mathbf{r}_{tip}) + \alpha_{em}\alpha_{mm}\underline{\mathbf{G}}^{mm}(\mathbf{r}_{img}-\mathbf{r}_{tip})\Big]\cdot\mathbf{H}^{inc}(\mathbf{r}_{tip}) \\
&+ \Big[\alpha_{ee}^2\underline{\mathbf{G}}^{ee}(\mathbf{r}_{img}-\mathbf{r}_{tip}) - \mu_0^{-1}\alpha_{em}\alpha_{ee}\underline{\mathbf{G}}^{em}(\mathbf{r}_{img}-\mathbf{r}_{tip}) \\
&+ \alpha_{ee}\alpha_{em}\underline{\mathbf{G}}^{me}(\mathbf{r}_{img}-\mathbf{r}_{tip}) - \mu_0^{-1}\alpha_{em}^2\underline{\mathbf{G}}^{mm}(\mathbf{r}_{img}-\mathbf{r}_{tip})\Big]\cdot\mathbf{E}^{sca}_{img\to tip}(\mathbf{r}_{tip}) \\
&+ \Big[\alpha_{ee}\alpha_{em}\underline{\mathbf{G}}^{ee}(\mathbf{r}_{img}-\mathbf{r}_{tip}) + \alpha_{ee}\alpha_{mm}\underline{\mathbf{G}}^{em}(\mathbf{r}_{img}-\mathbf{r}_{tip}) \\
&+ \alpha_{em}^2\underline{\mathbf{G}}^{me}(\mathbf{r}_{img}-\mathbf{r}_{tip}) + \alpha_{em}\alpha_{mm}\underline{\mathbf{G}}^{mm}(\mathbf{r}_{img}-\mathbf{r}_{tip})\Big]\cdot\mathbf{H}^{sca}_{img\to tip}(\mathbf{r}_{tip}))
\end{aligned}
\tag{A.12}
$$

Now if we assume,

$$
\begin{aligned}
\underline{\mathbf{A}}^e &= \alpha_{ee}^2\underline{\mathbf{G}}^{ee}(\mathbf{r}_{img}-\mathbf{r}_{tip}) - \mu_0^{-1}\alpha_{em}\alpha_{ee}\underline{\mathbf{G}}^{em}(\mathbf{r}_{img}-\mathbf{r}_{tip}) + \alpha_{ee}\alpha_{em}\underline{\mathbf{G}}^{me}(\mathbf{r}_{img}-\mathbf{r}_{tip}) \\
&- \mu_0^{-1}\alpha_{em}^2\underline{\mathbf{G}}^{mm}(\mathbf{r}_{img}-\mathbf{r}_{tip}) \\
\underline{\mathbf{B}}^e &= \alpha_{ee}\alpha_{em}\underline{\mathbf{G}}^{ee}(\mathbf{r}_{img}-\mathbf{r}_{tip}) + \alpha_{ee}\alpha_{mm}\underline{\mathbf{G}}^{em}(\mathbf{r}_{img}-\mathbf{r}_{tip}) + \alpha_{em}^2\underline{\mathbf{G}}^{me}(\mathbf{r}_{img}-\mathbf{r}_{tip}) \\
&+ \alpha_{em}\alpha_{mm}\underline{\mathbf{G}}^{mm}(\mathbf{r}_{img}-\mathbf{r}_{tip})
\end{aligned}
$$

we can rewrite the above equation as below.

$$
\begin{aligned}
&\Big[\underline{\mathbf{I}} - \underline{\mathbf{A}}^e\cdot\underline{\mathbf{G}}^{ee}(\mathbf{r}_{tip}-\mathbf{r}_{img}) - \underline{\mathbf{B}}^e\cdot\underline{\mathbf{G}}^{me}(\mathbf{r}_{tip}-\mathbf{r}_{img})\Big]\cdot\mathbf{p}_{img} \\
&- \Big[\underline{\mathbf{A}}^e\cdot\underline{\mathbf{G}}^{em}(\mathbf{r}_{tip}-\mathbf{r}_{img}) + \underline{\mathbf{B}}^e\cdot\underline{\mathbf{G}}^{mm}(\mathbf{r}_{tip}-\mathbf{r}_{img})\Big]\cdot\mathbf{m}_{img} \\
&= \alpha_{ee}\mathbf{E}^{inc}(\mathbf{r}_{img}) + \alpha_{em}\mathbf{H}^{inc}(\mathbf{r}_{img}) + \underline{\mathbf{A}}^e\cdot\mathbf{E}^{inc}(\mathbf{r}_{tip}) + \underline{\mathbf{B}}^e\cdot\mathbf{H}^{inc}(\mathbf{r}_{tip})
\end{aligned}
\tag{A.13}
$$

Now, if we redefine,

$$\underline{\mathbf{C}}^e = \underline{\mathbf{A}}^e \cdot \underline{\mathbf{G}}^{ee}(\mathbf{r}_{tip} - \mathbf{r}_{img}) + \underline{\mathbf{B}}^e \cdot \underline{\mathbf{G}}^{me}(\mathbf{r}_{tip} - \mathbf{r}_{img})$$
$$\underline{\mathbf{D}}^e = \underline{\mathbf{A}}^e \cdot \underline{\mathbf{G}}^{em}(\mathbf{r}_{tip} - \mathbf{r}_{img}) + \underline{\mathbf{B}}^e \cdot \underline{\mathbf{G}}^{mm}(\mathbf{r}_{tip} - \mathbf{r}_{img})$$

we get the above equation as:

$$\begin{aligned}\left[\underline{\mathbf{I}} - \underline{\mathbf{C}}^e\right] \cdot \mathbf{p}_{img} - \underline{\mathbf{D}}^e \cdot \mathbf{m}_{img} = \alpha_{ee}\mathbf{E}^{inc}(\mathbf{r}_{img}) + \alpha_{em}\mathbf{H}^{inc}(\mathbf{r}_{img}) \\ + \underline{\mathbf{A}}^e \cdot \mathbf{E}^{inc}(\mathbf{r}_{tip}) + \underline{\mathbf{B}}^e \cdot \mathbf{H}^{inc}(\mathbf{r}_{tip})\end{aligned} \tag{A.14}$$

Similarly, working on $\mathbf{m}_{img}$ in Eq. A.10 we get:

$$\begin{aligned}\left[\underline{\mathbf{I}} - \underline{\mathbf{C}}^m\right] \cdot \mathbf{m}_{img} - \underline{\mathbf{D}}^m \cdot \mathbf{p}_{img} = -\mu_0^{-1}\alpha_{em}\mathbf{E}^{inc}(\mathbf{r}_{img}) + \alpha_{mm}\mathbf{H}^{inc}(\mathbf{r}_{img}) \\ + \underline{\mathbf{B}}^m \cdot \mathbf{E}^{inc}(\mathbf{r}_{tip}) + \underline{\mathbf{A}}^m \cdot \mathbf{H}^{inc}(\mathbf{r}_{tip})\end{aligned} \tag{A.15}$$

where,

$$\begin{aligned}\underline{\mathbf{A}}^m &= -\mu_0^{-1}\alpha_{em}^2\underline{\mathbf{G}}^{ee}(\mathbf{r}_{img} - \mathbf{r}_{tip}) - \mu_0^{-1}\alpha_{em}\alpha_{mm}\underline{\mathbf{G}}^{em}(\mathbf{r}_{img} - \mathbf{r}_{tip}) \\ &\quad + \alpha_{mm}\alpha_{em}\underline{\mathbf{G}}^{me}(\mathbf{r}_{img} - \mathbf{r}_{tip}) + \alpha_{mm}^2\underline{\mathbf{G}}^{mm}(\mathbf{r}_{img} - \mathbf{r}_{tip}) \\ \underline{\mathbf{B}}^m &= -\mu_0^{-1}\alpha_{em}\alpha_{ee}\underline{\mathbf{G}}^{ee}(\mathbf{r}_{img} - \mathbf{r}_{tip}) + \mu_0^{-2}\alpha_{em}^2\underline{\mathbf{G}}^{em}(\mathbf{r}_{img} - \mathbf{r}_{tip}) \\ &\quad + \alpha_{mm}\alpha_{ee}\underline{\mathbf{G}}^{me}(\mathbf{r}_{img} - \mathbf{r}_{tip}) - \mu_0^{-1}\alpha_{em}\alpha_{mm}\underline{\mathbf{G}}^{mm}(\mathbf{r}_{img} - \mathbf{r}_{tip}) \\ \underline{\mathbf{C}}^m &= \underline{\mathbf{A}}^m \cdot \underline{\mathbf{G}}^{mm}(\mathbf{r}_{tip} - \mathbf{r}_{img}) + \underline{\mathbf{B}}^m \cdot \underline{\mathbf{G}}^{em}(\mathbf{r}_{tip} - \mathbf{r}_{img}) \\ \underline{\mathbf{D}}^m &= \underline{\mathbf{A}}^m \cdot \underline{\mathbf{G}}^{me}(\mathbf{r}_{tip} - \mathbf{r}_{img}) + \underline{\mathbf{B}}^m \cdot \underline{\mathbf{G}}^{ee}(\mathbf{r}_{tip} - \mathbf{r}_{img})\end{aligned}$$

In our configuration the dipole and the image are located along "z" axis. So, we can write the green's functions as stated below.[118, 117, 23]

$\underline{\mathbf{G}}^{ee}(\mathbf{r}_{tip} - \mathbf{r}_{img}) = \underline{\mathbf{G}}^{ee}(\mathbf{r}_{img} - \mathbf{r}_{tip}) = \frac{1}{4\pi\varepsilon_0|z|^3}(3\hat{\mathbf{z}}\hat{\mathbf{z}} - \underline{\mathbf{I}})$;

$\underline{\mathbf{G}}^{em}(\mathbf{r}_{tip} - \mathbf{r}_{img}) = \underline{\mathbf{G}}^{em}(\mathbf{r}_{img} - \mathbf{r}_{tip}) = \frac{i\omega\mu_0}{4\pi k^2}\nabla\left(\frac{3\hat{\mathbf{z}}\hat{\mathbf{z}} - \underline{\mathbf{I}}}{|z|^3}\right) = \frac{3i\omega\mu_0}{4\pi k^2}\left(\frac{\hat{\mathbf{y}}\hat{\mathbf{x}} - \hat{\mathbf{x}}\hat{\mathbf{y}}}{|z|^4}\right)$;

$\underline{\mathbf{G}}^{mm}(\mathbf{r}_{tip}-\mathbf{r}_{img}) = \underline{\mathbf{G}}^{mm}(\mathbf{r}_{img}-\mathbf{r}_{tip}) = \frac{1}{4\pi|z|^3}(3\hat{\mathbf{z}}\hat{\mathbf{z}} - \underline{\mathbf{I}})$;

$\underline{\mathbf{G}}^{me}(\mathbf{r}_{tip}-\mathbf{r}_{img}) = \underline{\mathbf{G}}^{me}(\mathbf{r}_{img}-\mathbf{r}_{tip}) = -\frac{3i\omega}{4\pi k^2}\Big(\frac{\hat{\mathbf{y}}\hat{\mathbf{x}}-\hat{\mathbf{x}}\hat{\mathbf{y}}}{|z|^4}\Big)$

Now, we determine the explicit form of the eight dydas ($\underline{\mathbf{A}}^e$, $\underline{\mathbf{B}}^e$, $\underline{\mathbf{C}}^e$, $\underline{\mathbf{D}}^e$, $\underline{\mathbf{A}}^m$, $\underline{\mathbf{B}}^m$, $\underline{\mathbf{C}}^m$, $\underline{\mathbf{D}}^m$) using the form of electric and magnetic dyadic green's functions defined above.

$$
\begin{aligned}
\underline{\mathbf{A}}^e &= \big(\frac{\alpha_{ee}^2}{\varepsilon_0} - \frac{\alpha_{em}^2}{\mu_0}\big)\frac{1}{4\pi}\Big(\frac{3\hat{\mathbf{z}}\hat{\mathbf{z}}-\underline{\mathbf{I}}}{|z|^3}\Big) - \alpha_{ee}\alpha_{em}\frac{3i\omega}{2\pi k^2}\Big(\frac{\hat{\mathbf{y}}\hat{\mathbf{x}}-\hat{\mathbf{x}}\hat{\mathbf{y}}}{|z|^4}\Big)\\
\underline{\mathbf{B}}^e &= \big(\frac{\alpha_{ee}\alpha_{em}}{\varepsilon_0} + \alpha_{mm}\alpha_{em}\big)\frac{1}{4\pi}\Big(\frac{3\hat{\mathbf{z}}\hat{\mathbf{z}}-\underline{\mathbf{I}}}{|z|^3}\Big) + \big(\mu_0\alpha_{ee}\alpha_{mm} - \alpha_{em}^2\big)\frac{3i\omega}{4\pi k^2}\Big(\frac{\hat{\mathbf{y}}\hat{\mathbf{x}}-\hat{\mathbf{x}}\hat{\mathbf{y}}}{|z|^4}\Big)\\
\underline{\mathbf{C}}^e &= \big(\frac{\alpha_{ee}^2}{\varepsilon_0} - \frac{\alpha_{em}^2}{\mu_0}\big)\frac{1}{16\pi^2\varepsilon_0}\Big(\frac{3\hat{\mathbf{z}}\hat{\mathbf{z}}-\underline{\mathbf{I}}}{|z|^6}\Big) + \big(\alpha_{mm}\alpha_{em} - \frac{\alpha_{ee}\alpha_{em}}{\varepsilon_0}\big)\frac{3i\omega}{16\pi^2k^2}\Big(\frac{\hat{\mathbf{x}}\hat{\mathbf{y}}-\hat{\mathbf{y}}\hat{\mathbf{x}}}{|z|^7}\Big)\\
&\quad - \big(\mu_0\alpha_{ee}\alpha_{mm} - \alpha_{em}^2\big)\frac{9\omega^2}{16\pi^2k^4}\Big(\frac{\hat{\mathbf{y}}\hat{\mathbf{y}}+\hat{\mathbf{x}}\hat{\mathbf{x}}}{|z|^8}\Big)\\
\underline{\mathbf{D}}^e &= \big(\alpha_{mm}\alpha_{em} + \frac{\alpha_{ee}\alpha_{em}}{\varepsilon_0}\big)\frac{1}{16\pi^2}\Big(\frac{3\hat{\mathbf{z}}\hat{\mathbf{z}}-\underline{\mathbf{I}}}{|z|^6}\Big)\\
&\quad + \big(\frac{\alpha_{ee}^2}{\varepsilon_0} - \frac{2\alpha_{em}^2}{\mu_0} + \alpha_{mm}\alpha_{ee}\big)\frac{3i\omega\mu_0}{16\pi^2k^2}\Big(\frac{\hat{\mathbf{x}}\hat{\mathbf{y}}-\hat{\mathbf{y}}\hat{\mathbf{x}}}{|z|^7}\Big) - \alpha_{ee}\alpha_{em}\frac{9\omega^2\mu_0}{8\pi^2k^4}\Big(\frac{\hat{\mathbf{y}}\hat{\mathbf{y}}+\hat{\mathbf{x}}\hat{\mathbf{x}}}{|z|^8}\Big)\\
\underline{\mathbf{A}}^m &= \big(\alpha_{mm}^2 - \frac{\mu_0^{-1}\alpha_{em}^2}{\varepsilon_0}\big)\frac{1}{4\pi}\Big(\frac{3\hat{\mathbf{z}}\hat{\mathbf{z}}-\underline{\mathbf{I}}}{|z|^3}\Big) - \alpha_{mm}\alpha_{em}\frac{3i\omega}{2\pi k^2}\Big(\frac{\hat{\mathbf{y}}\hat{\mathbf{x}}-\hat{\mathbf{x}}\hat{\mathbf{y}}}{|z|^4}\Big)\\
\underline{\mathbf{B}}^m &= -\big(\frac{\mu_0^{-1}\alpha_{ee}\alpha_{em}}{\varepsilon_0} + \frac{\alpha_{mm}\alpha_{em}}{\mu_0}\big)\frac{1}{4\pi}\Big(\frac{3\hat{\mathbf{z}}\hat{\mathbf{z}}-\underline{\mathbf{I}}}{|z|^3}\Big) + \big(\mu_0^{-1}\alpha_{em}^2 - \alpha_{ee}\alpha_{mm}\big)\frac{3i\omega}{4\pi k^2}\Big(\frac{\hat{\mathbf{y}}\hat{\mathbf{x}}-\hat{\mathbf{x}}\hat{\mathbf{y}}}{|z|^4}\Big)\\
\underline{\mathbf{C}}^m &= \big(\alpha_{mm}^2 - \frac{\mu_0^{-1}\alpha_{em}^2}{\varepsilon_0}\big)\frac{1}{16\pi^2}\Big(\frac{3\hat{\mathbf{z}}\hat{\mathbf{z}}-\underline{\mathbf{I}}}{|z|^6}\Big) - \big(3\alpha_{mm}\alpha_{em} + \frac{\alpha_{ee}\alpha_{em}}{\varepsilon_0}\big)\frac{3i\omega}{16\pi^2k^2}\Big(\frac{\hat{\mathbf{x}}\hat{\mathbf{y}}-\hat{\mathbf{y}}\hat{\mathbf{x}}}{|z|^7}\Big)\\
&\quad + \big(\alpha_{em}^2 - \mu_o\alpha_{ee}\alpha_{mm}\big)\frac{9\omega^2}{16\pi^2k^4}\Big(\frac{\hat{\mathbf{y}}\hat{\mathbf{y}}+\hat{\mathbf{x}}\hat{\mathbf{x}}}{|z|^8}\Big)\\
\underline{\mathbf{D}}^m &= -\big(\mu_0^{-1}\alpha_{mm}\alpha_{em} + \frac{\mu_0^{-1}\alpha_{ee}\alpha_{em}}{\varepsilon_0}\big)\frac{1}{16\pi^2\varepsilon_0}\Big(\frac{3\hat{\mathbf{z}}\hat{\mathbf{z}}-\underline{\mathbf{I}}}{|z|^6}\Big)\\
&\quad + \big(\frac{2\mu_0^{-1}\alpha_{em}^2}{\varepsilon_0} - \alpha_{mm}^2 - \alpha_{mm}\alpha_{ee}\big)\frac{3i\omega}{16\pi^2k^2}\Big(\frac{\hat{\mathbf{x}}\hat{\mathbf{y}}-\hat{\mathbf{y}}\hat{\mathbf{x}}}{|z|^7}\Big) + \alpha_{mm}\alpha_{em}\frac{9\omega^2}{8\pi^2k^4}\Big(\frac{\hat{\mathbf{y}}\hat{\mathbf{y}}+\hat{\mathbf{x}}\hat{\mathbf{x}}}{|z|^8}\Big)
\end{aligned}
$$

At this point, we will determine 'x', 'y' and 'z' components of $\mathbf{p}_{img}$ and $\mathbf{m}_{img}$ from Eqs. A.14

and A.15. Equating 'x', 'y' and 'z' components on both sides of Eq. A.14 we get:

$$
\begin{aligned}
&p_{img,x}\Big[1+\big(\frac{\alpha_{ee}^2}{\varepsilon_0}-\frac{\alpha_{em}^2}{\mu_0}\big)\frac{1}{16\pi^2\varepsilon_0|z|^6}+\big(\mu_0\alpha_{ee}\alpha_{mm}-\alpha_{em}^2\big)\frac{9\omega^2}{16\pi^2k^4|z|^8}\Big]\\
&-p_{img,y}\big(\alpha_{mm}\alpha_{em}-\frac{\alpha_{ee}\alpha_{em}}{\varepsilon_0}\big)\frac{3i\omega}{16\pi^2k^2|z|^7}\\
&+m_{img,x}\Big[\big(\alpha_{mm}\alpha_{em}+\frac{\alpha_{ee}\alpha_{em}}{\varepsilon_0}\big)\frac{1}{16\pi^2|z|^6}+\alpha_{ee}\alpha_{em}\frac{9\omega^2\mu_0}{8\pi^2k^4|z|^8}\Big]\\
&-m_{img,y}\big(\frac{\alpha_{ee}^2}{\varepsilon_0}-\frac{2\alpha_{em}^2}{\mu_0}+\alpha_{mm}\alpha_{ee}\big)\frac{3i\omega\mu_0}{16\pi^2k^2|z|^7}=\\
&\alpha_{ee}E_x^{inc}(\mathbf{r}_{img})+\alpha_{em}H_x^{inc}(\mathbf{r}_{img})\\
&-\big(\frac{\alpha_{ee}^2}{\varepsilon_0}-\frac{\alpha_{em}^2}{\mu_0}\big)\frac{1}{4\pi|z|^3}E_x^{inc}(\mathbf{r}_{tip})+\alpha_{ee}\alpha_{em}\frac{3i\omega}{2\pi k^2|z|^4}E_y^{inc}(\mathbf{r}_{tip})\\
&-\big(\frac{\alpha_{ee}\alpha_{em}}{\varepsilon_0}+\alpha_{mm}\alpha_{em}\big)\frac{1}{4\pi|z|^3}H_x^{inc}(\mathbf{r}_{tip})-\big(\mu_0\alpha_{ee}\alpha_{mm}-\alpha_{em}^2\big)\frac{3i\omega}{4\pi k^2|z|^4}H_y^{inc}(\mathbf{r}_{tip})
\end{aligned}
\tag{A.16}
$$

$$
\begin{aligned}
&p_{img,x}\big(\alpha_{mm}\alpha_{em}-\frac{\alpha_{ee}\alpha_{em}}{\varepsilon_0}\big)\frac{3i\omega}{16\pi^2k^2|z|^7}\\
&+p_{img,y}\Big[1+\big(\frac{\alpha_{ee}^2}{\varepsilon_0}-\frac{\alpha_{em}^2}{\mu_0}\big)\frac{1}{16\pi^2\varepsilon_0|z|^6}+\big(\mu_0\alpha_{ee}\alpha_{mm}-\alpha_{em}^2\big)\frac{9\omega^2}{16\pi^2k^4|z|^8}\Big]\\
&+m_{img,x}\big(\frac{\alpha_{ee}^2}{\varepsilon_0}-\frac{2\alpha_{em}^2}{\mu_0}+\alpha_{mm}\alpha_{ee}\big)\frac{3i\omega\mu_0}{16\pi^2k^2|z|^7}\\
&+m_{img,y}\Big[\big(\alpha_{mm}\alpha_{em}+\frac{\alpha_{ee}\alpha_{em}}{\varepsilon_0}\big)\frac{1}{16\pi^2|z|^6}+\alpha_{ee}\alpha_{em}\frac{9\omega^2\mu_0}{8\pi^2k^4|z|^8}\Big]=\\
&\alpha_{ee}E_y^{inc}(\mathbf{r}_{img})+\alpha_{em}H_y^{inc}(\mathbf{r}_{img})\\
&-\alpha_{ee}\alpha_{em}\frac{3i\omega}{2\pi k^2|z|^4}E_x^{inc}(\mathbf{r}_{tip})-\big(\frac{\alpha_{ee}^2}{\varepsilon_0}-\frac{\alpha_{em}^2}{\mu_0}\big)\frac{1}{4\pi|z|^3}E_y^{inc}(\mathbf{r}_{tip})\\
&+\big(\mu_0\alpha_{ee}\alpha_{mm}-\alpha_{em}^2\big)\frac{3i\omega}{4\pi k^2|z|^4}H_x^{inc}(\mathbf{r}_{tip})-\big(\frac{\alpha_{ee}\alpha_{em}}{\varepsilon_0}+\alpha_{mm}\alpha_{em}\big)\frac{1}{4\pi|z|^3}H_y^{inc}(\mathbf{r}_{tip})
\end{aligned}
\tag{A.17}
$$

$$
\begin{aligned}
&p_{img,z}\Big[1-\big(\frac{\alpha_{ee}^2}{\varepsilon_0}-\frac{\alpha_{em}^2}{\mu_0}\big)\frac{2}{16\pi^2\varepsilon_0|z|^6}\Big]-m_{img,z}\big(\alpha_{mm}\alpha_{em}+\frac{\alpha_{ee}\alpha_{em}}{\varepsilon_0}\big)\frac{2}{16\pi^2|z|^6}=\\
&\alpha_{ee}E_z^{inc}(\mathbf{r}_{img})+\alpha_{em}H_z^{inc}(\mathbf{r}_{img})\\
&+\big(\frac{\alpha_{ee}^2}{\varepsilon_0}-\frac{\alpha_{em}^2}{\mu_0}\big)\frac{2}{4\pi|z|^3}E_z^{inc}(\mathbf{r}_{tip})+\big(\frac{\alpha_{ee}\alpha_{em}}{\varepsilon_0}+\alpha_{mm}\alpha_{em}\big)\frac{2}{4\pi|z|^3}H_z^{inc}(\mathbf{r}_{tip})
\end{aligned}
\tag{A.18}
$$

Similarly, equating 'x', 'y' and 'z' components on both sides of Eq. A.15 we get:

$$
\begin{aligned}
&-p_{img,x}\Big[\big(\alpha_{mm}+\frac{\alpha_{ee}}{\varepsilon_0}\big)\mu_0^{-1}\alpha_{em}\frac{1}{16\pi^2\varepsilon_0|z|^6}+\alpha_{mm}\alpha_{em}\frac{9\omega^2}{8\pi^2k^4|z|^8}\Big]\\
&-p_{img,y}\big(\frac{2\mu_0^{-1}\alpha_{em}^2}{\varepsilon_0}-\alpha_{mm}^2-\alpha_{mm}\alpha_{ee}\big)\frac{3i\omega}{16\pi^2k^2|z|^7}\\
&+m_{img,x}\Big[1+\big(\alpha_{mm}^2-\frac{\mu_0^{-1}\alpha_{em}^2}{\varepsilon_0}\big)\frac{1}{16\pi^2|z|^6}-\big(\alpha_{em}^2-\mu_0\alpha_{ee}\alpha_{mm}\big)\frac{9\omega^2}{16\pi^2k^4|z|^8}\Big]\\
&+m_{img,y}\big(3\alpha_{mm}+\frac{\alpha_{ee}}{\varepsilon_0}\big)\alpha_{em}\frac{3i\omega}{16\pi^2k^2|z|^7}=\\
&\quad-\mu_0^{-1}\alpha_{em}E_x^{inc}(\mathbf{r}_{img})+\alpha_{mm}H_x^{inc}(\mathbf{r}_{img})\\
&+\big(\frac{\mu_0^{-1}\alpha_{ee}\alpha_{em}}{\varepsilon_0}+\frac{\alpha_{mm}\alpha_{em}}{\mu_0}\big)\frac{1}{4\pi|z|^3}E_x^{inc}(\mathbf{r}_{tip})-\big(\mu_0^{-1}\alpha_{em}^2-\alpha_{ee}\alpha_{mm}\big)\frac{3i\omega}{4\pi k^2|z|^4}E_y^{inc}(\mathbf{r}_{tip})\\
&-\big(\alpha_{mm}^2-\frac{\mu_0^{-1}\alpha_{em}^2}{\varepsilon_0}\big)\frac{1}{4\pi|z|^3}H_x^{inc}(\mathbf{r}_{tip})+\alpha_{mm}\alpha_{em}\frac{3i\omega}{2\pi k^2|z|^4}H_y^{inc}(\mathbf{r}_{tip})
\end{aligned}
\tag{A.19}
$$

$$
\begin{aligned}
&p_{img,x}\big(\frac{2\mu_0^{-1}\alpha_{em}^2}{\varepsilon_0}-\alpha_{mm}^2-\alpha_{mm}\alpha_{ee}\big)\frac{3i\omega}{16\pi^2k^2|z|^7}\\
&-p_{img,y}\Big[\big(\alpha_{mm}+\frac{\alpha_{ee}}{\varepsilon_0}\big)\mu_0^{-1}\alpha_{em}\frac{1}{16\pi^2\varepsilon_0|z|^6}+\alpha_{mm}\alpha_{em}\frac{9\omega^2}{8\pi^2k^4|z|^8}\Big]\\
&-m_{img,x}\big(3\alpha_{mm}+\frac{\alpha_{ee}}{\varepsilon_0}\big)\alpha_{em}\frac{3i\omega}{16\pi^2k^2|z|^7}\\
&+m_{img,y}\Big[1+\big(\alpha_{mm}^2-\frac{\mu_0^{-1}\alpha_{em}^2}{\varepsilon_0}\big)\frac{1}{16\pi^2|z|^6}-\big(\alpha_{em}^2-\mu_0\alpha_{ee}\alpha_{mm}\big)\frac{9\omega^2}{16\pi^2k^4|z|^8}\Big]=\\
&-\mu_0^{-1}\alpha_{em}E_x^{inc}(\mathbf{r}_{img})+\alpha_{mm}H_x^{inc}(\mathbf{r}_{img})\\
&+\big(\mu_0^{-1}\alpha_{em}^2-\alpha_{ee}\alpha_{mm}\big)\frac{3i\omega}{4\pi k^2|z|^4}E_x^{inc}(\mathbf{r}_{tip})+\big(\frac{\mu_0^{-1}\alpha_{ee}\alpha_{em}}{\varepsilon_0}+\frac{\alpha_{mm}\alpha_{em}}{\mu_0}\big)\frac{1}{4\pi|z|^3}E_y^{inc}(\mathbf{r}_{tip})\\
&-\alpha_{mm}\alpha_{em}\frac{3i\omega}{2\pi k^2|z|^4}H_x^{inc}(\mathbf{r}_{tip})-\big(\alpha_{mm}^2-\frac{\mu_o^{-1}\alpha_{em}^2}{\varepsilon_0}\big)\frac{1}{4\pi|z|^3}H_y^{inc}(\mathbf{r}_{tip})
\end{aligned}
\tag{A.20}
$$

$$
\begin{aligned}
&p_{img,z}\big(\alpha_{mm}+\frac{\alpha_{ee}}{\varepsilon_0}\big)\mu_0^{-1}\alpha_{em}\frac{2}{16\pi^2\varepsilon_0|z|^6}+m_{img,z}\bigg[1-\big(\alpha_{mm}^2-\frac{\mu_0^{-1}\alpha_{em}^2}{\varepsilon_0}\big)\frac{2}{16\pi^2|z|^6}\bigg]=\\
&-\mu_0^{-1}\alpha_{em}E_z^{inc}(\mathbf{r}_{img})+\alpha_{mm}H_z^{inc}(\mathbf{r}_{img})\\
&-\big(\frac{\mu_0^{-1}\alpha_{ee}\alpha_{em}}{\varepsilon_0}+\frac{\alpha_{mm}\alpha_{em}}{\mu_0}\big)\frac{2}{4\pi|z|^3}E_z^{inc}(\mathbf{r}_{tip})+\big(\alpha_{mm}^2-\frac{\mu_0^{-1}\alpha_{em}^2}{\varepsilon_0}\big)\frac{2}{4\pi|z|^3}H_z^{inc}(\mathbf{r}_{tip})
\end{aligned}
\tag{A.21}
$$

Now, we define some parameters for convenience as mentioned below.

$$
\begin{aligned}
a_1&=\big(\frac{\alpha_{ee}^2}{\varepsilon_0}-\frac{\alpha_{em}^2}{\mu_0}\big)\frac{1}{4\pi};& a_4&=\big(\alpha_{mm}^2-\frac{\mu_0^{-1}\alpha_{em}^2}{\varepsilon_0}\big)\frac{1}{4\pi}\\
b_1&=\big(\mu_0\alpha_{ee}\alpha_{mm}-\alpha_{em}^2\big)\frac{3i\omega}{4\pi k^2};& c_1&=\big(\alpha_{mm}-\frac{\alpha_{ee}}{\varepsilon_0}\big)\alpha_{em}\frac{3i\omega}{16\pi^2k^2}\\
d_1&=\big(\alpha_{mm}+\frac{\alpha_{ee}}{\varepsilon_0}\big)\alpha_{em}\frac{1}{4\pi};& d_4&=\big(3\alpha_{mm}+\frac{\alpha_{ee}}{\varepsilon_0}\big)\alpha_{em}\frac{3i\omega}{16\pi^2k^2}\\
e_1&=\alpha_{ee}\alpha_{em}\frac{3i\omega}{2\pi k^2};& e_4&=\alpha_{mm}\alpha_{em}\frac{3i\omega}{2\pi k^2}\\
f_1&=\big(\frac{\alpha_{ee}^2}{\varepsilon_0}-\frac{2\alpha_{em}^2}{\mu_0}+\alpha_{mm}\alpha_{ee}\big)\frac{3i\omega\mu_0}{16\pi^2k^2};& f_4&=\big(\frac{2\mu_0^{-1}\alpha_{em}^2}{\varepsilon_0}-\alpha_{mm}\alpha_{ee}-\alpha_{mm}^2\big)\frac{3i\omega}{16\pi^2k^2}\\
P_1(z)&=1+\frac{a_1}{4\pi\varepsilon_0|z|^6}-\frac{3i\omega b_1}{4\pi k^2|z|^8};& P_2(z)&=\frac{c_1}{|z|^7};\\
M_1(z)&=\frac{d_1}{4\pi|z|^6}-\frac{3i\omega\mu_0e_1}{4\pi k^2|z|^8};& M_2(z)&=\frac{f_1}{|z|^7}\\
P_3(z)&=\frac{\mu_0^{-1}d_1}{4\pi\varepsilon_0|z|^6}-\frac{3i\omega e_4}{4\pi k^2|z|^8};& P_4(z)&=\frac{f_4}{|z|^7};\\
M_3(z)&=1+\frac{a_4}{4\pi|z|^6}-\frac{3i\omega\mu_0b_1}{4\pi k^2|z|^8};& M_4(z)&=\frac{d_4}{|z|^7}
\end{aligned}
$$

$$
\begin{aligned}
E_{effxy1}(z)&=\alpha_{ee}E_x^{inc}(\mathbf{r}_{img})+\alpha_{em}H_x^{inc}(\mathbf{r}_{img})\\
&\quad-\frac{a_1}{|z|^3}E_x^{inc}(\mathbf{r}_{tip})+\frac{e_1}{|z|^4}E_y^{inc}(\mathbf{r}_{tip})-\frac{d_1}{|z|^3}H_x^{inc}(\mathbf{r}_{tip})-\frac{b_1}{|z|^4}H_y^{inc}(\mathbf{r}_{tip});\\
E_{effxy2}(z)&=\alpha_{ee}E_y^{inc}(\mathbf{r}_{img})+\alpha_{em}H_y^{inc}(\mathbf{r}_{img})\\
&\quad-\frac{e_1}{|z|^3}E_x^{inc}(\mathbf{r}_{tip})-\frac{a_1}{|z|^4}E_y^{inc}(\mathbf{r}_{tip})+\frac{b_1}{|z|^3}H_x^{inc}(\mathbf{r}_{tip})-\frac{d_1}{|z|^4}H_y^{inc}(\mathbf{r}_{tip})
\end{aligned}
$$

$$
\begin{aligned}
E_{effxy3}(z) &= -\mu_0^{-1}\alpha_{em}E_x^{inc}(\mathbf{r}_{img}) + \alpha_{mm}H_x^{inc}(\mathbf{r}_{img}) \\
&\quad + \frac{\mu_0^{-1}d_1}{|z|^3}E_x^{inc}(\mathbf{r}_{tip}) + \frac{\mu_0^{-1}b_1}{|z|^4}E_y^{inc}(\mathbf{r}_{tip}) - \frac{a_4}{|z|^3}H_x^{inc}(\mathbf{r}_{tip}) + \frac{e_4}{|z|^4}H_y^{inc}(\mathbf{r}_{tip}) \\
E_{effxy4}(z) &= -\mu_0^{-1}\alpha_{em}E_y^{inc}(\mathbf{r}_{img}) + \alpha_{mm}H_y^{inc}(\mathbf{r}_{img}) \\
&\quad - \frac{\mu_0^{-1}b_1}{|z|^3}E_x^{inc}(\mathbf{r}_{tip}) + \frac{\mu_0^{-1}d_1}{|z|^4}E_y^{inc}(\mathbf{r}_{tip}) - \frac{e_4}{|z|^3}H_x^{inc}(\mathbf{r}_{tip}) - \frac{a_4}{|z|^4}H_y^{inc}(\mathbf{r}_{tip}) \\
E_{effz1}(z) &= \alpha_{ee}E_z^{inc}(\mathbf{r}_{img}) + \alpha_{em}H_z^{inc}(\mathbf{r}_{img}) + \frac{2a_1}{|z|^3}E_z^{inc}(\mathbf{r}_{tip}) + \frac{2d_1}{|z|^3}H_z^{inc}(\mathbf{r}_{tip}) \\
E_{effz2}(z) &= -\mu_0^{-1}\alpha_{em}E_z^{inc}(\mathbf{r}_{img}) + \alpha_{mm}H_z^{inc}(\mathbf{r}_{img}) - \frac{2\mu_0^{-1}d_1}{|z|^3}E_z^{inc}(\mathbf{r}_{tip}) + \frac{2a_4}{|z|^3}H_z^{inc}(\mathbf{r}_{tip})
\end{aligned}
$$

Rewriting the Eqs. A.16-A.21 in terms of the above parameters, we get:

$$P_1(z)p_{img,x} - P_2(z)p_{img,y} + M_1(z)m_{img,x} - M_2(z)m_{img,y} = E_{effxy1}(z) \tag{A.22}$$

$$P_2(z)p_{img,x} + P_1(z)p_{img,y} + M_2(z)m_{img,x} + M_1(z)m_{img,y} = E_{effxy2}(z) \tag{A.23}$$

$$\big[1 - \frac{2a_1}{4\pi\varepsilon_0|z|^6}\big]p_{img,z} - \frac{2d_1}{4\pi|z|^6}m_{img,z} = E_{effz1}(z) \tag{A.24}$$

$$-P_3(z)p_{img,x} - P_4(z)p_{img,y} + M_3(z)m_{img,x} + M_4(z)m_{img,y} = E_{effxy3}(z) \tag{A.25}$$

$$P_4(z)p_{img,x} - P_3(z)p_{img,y} - M_4(z)m_{img,x} + M_3(z)m_{img,y} = E_{effxy4}(z) \tag{A.26}$$

$$\frac{2d_1\mu_0^{-1}}{4\pi\varepsilon_0|z|^6}p_{img,z} + \big[1 - \frac{2a_4}{4\pi|z|^6}\big]m_{img,z} = E_{effz2}(z) \tag{A.27}$$

Solving Eqs.A.24 and A.27, we find $p_{img,z}$ and $m_{img,z}$ as equations A.28 and A.29.

$$
\begin{aligned}
p_{img,z} = &\Big[\big[1 - \frac{2a_4}{4\pi|z|^6}\big]\big[1 - \frac{2a_1}{4\pi\varepsilon_0|z|^6}\big] + \frac{2d_1\mu_0^{-1}}{4\pi\varepsilon_0|z|^6}\frac{2d_1}{4\pi|z|^6}\Big]^{-1} \\
&\Big[\big[1 - \frac{2a_4}{4\pi|z|^6}\big]E_{effz1}(z) + \frac{2d_1}{4\pi|z|^6}E_{effz2}(z)\Big]
\end{aligned} \tag{A.28}
$$

$$
\begin{aligned}
m_{img,z} = &\Big[\big[1 - \frac{2a_4}{4\pi|z|^6}\big]\big[1 - \frac{2a_1}{4\pi\varepsilon_0|z|^6}\big] - \frac{2d_1\mu_0^{-1}}{4\pi\varepsilon_0|z|^6}\frac{2d_1}{4\pi|z|^6}\Big]^{-1} \\
&\Big[\big[1 - \frac{2a_1}{4\pi\varepsilon_0|z|^6}\big]E_{effz2}(z) - \frac{2d_1\mu_o^{-1}}{4\pi\varepsilon_0|z|^6}E_{effz1}(z)\Big]
\end{aligned} \tag{A.29}
$$

Solving Eqs. A.22, A.23, A.25 and A.26, we get $p_{img,x}$, $p_{img,y}$, $m_{img,x}$ and $m_{img,y}$ as:

$$\begin{aligned} p_{img,x} = & \Big[MP_1(z)^2 + MP_2(z)^2\Big]^{-1} \\ & \Big[MP_1(z)\Big[\big(M_3(z)^2 + M_4(z)^2\big)\big(M_1(z)E_{effxy1}(z) + M_2(z)E_{effxy2}(z)\big) \\ & - \big(M_1(z)^2 + M_2(z)^2\big)\big(- M_4(z)E_{effxy4}(z) + M_3(z)E_{effxy3}(z)\big)\Big] \\ & + MP_2(z)\Big[\big(M_3(z)^2 + M_4(z)^2\big)\big(M_1(z)E_{effxy2}(z) - M_2(z)E_{effxy1}(z)\big) \\ & + \big(M_1(z)^2 + M_2(z)^2\big)\big(- M_3(z)E_{effxy4}(z) - M_4(z)E_{effxy3}(z)\big)\Big]\Big] \end{aligned} \tag{A.30}$$

$$\begin{aligned} p_{img,y} = & \Big[MP_1(z)^2 + MP_2(z)^2\Big]^{-1} \\ & \Big[MP_1(z)\Big[\big(M_3(z)^2 + M_4(z)^2\big)\big(M_1(z)E_{effxy2}(z) - M_2(z)E_{effxy1}(z)\big) \\ & + \big(M_1(z)^2 + M_2(z)^2\big)\big(- M_3(z)E_{effxy4}(z) - M_4(z)E_{effxy3}(z)\big)\Big] \\ & - MP_2(z)\Big[\big(M_3(z)^2 + M_4(z)^2\big)\big(M_1(z)E_{effxy1}(z) + M_2(z)E_{effxy2}(z)\big) \\ & - \big(M_1(z)^2 + M_2(z)^2\big)\big(- M_4(z)E_{effxy4}(z) + M_3(z)E_{effxy3}(z)\big)\Big]\Big] \end{aligned} \tag{A.31}$$

where,

$$\begin{aligned} MP_1(z) = & \big(M_3(z)^2 + M_4(z)^2\big)\big(P_1(z)M_1(z) + P_2(z)M_2(z)\big) \\ & + \big(M_1(z)^2 + M_2(z)^2\big)\big(P_3(z)M_3(z) + P_4(z)M_4(z)\big) \\ MP_2(z) = & \big(M_3(z)^2 + M_4(z)^2\big)\big(P_2(z)M_1(z) - P_1(z)M_2(z)\big) \\ & - \big(M_1(z)^2 + M_2(z)^2\big)\big(P_4(z)M_3(z) - P_3(z)M_4(z)\big) \end{aligned}$$

$$
\begin{aligned}
m_{img,x} = &\left[PM_1(z)^2 + PM_2(z)^2\right]^{-1} \\
&\Big[PM_1(z)\Big[\big(P_3(z)^2 + P_4(z)^2\big)\big(P_1(z)E_{effxy1}(z) + P_2(z)E_{effxy2}(z)\big) \\
&- \big(P_1(z)^2 + P_2(z)^2\big)\big(P_4(z)E_{effxy4}(z) - P_3(z)E_{effxy3}(z)\big)\Big] \\
&+ PM_2(z)\Big[\big(P_3(z)^2 + P_4(z)^2\big)\big(P_1(z)E_{effxy2}(z) - P_2(z)E_{effxy1}(z)\big) \\
&+ \big(P_1(z)^2 + P_2(z)^2\big)\big(P_3(z)E_{effxy4}(z) + P_4(z)E_{effxy3}(z)\big)\Big]\Big]
\end{aligned} \tag{A.32}
$$

$$
\begin{aligned}
m_{img,y} = &\left[PM_1(z)^2 + PM_2(z)^2\right]^{-1} \\
&\Big[PM_1(z)\Big[\big(P_3(z)^2 + P_4(z)^2\big)\big(P_1(z)E_{effxy2}(z) - P_2(z)E_{effxy1}(z)\big) \\
&+ \big(P_1(z)^2 + P_2(z)^2\big)\big(P_3(z)E_{effxy4}(z) + P_4(z)E_{effxy3}(z)\big)\Big] \\
&- PM_2(z)\Big[\big(P_3(z)^2 + P_4(z)^2\big)\big(P_1(z)E_{effxy1}(z) + P_2(z)E_{effxy2}(z)\big) \\
&- \big(P_1(z)^2 + P_2(z)^2\big)\big(P_4(z)E_{effxy4}(z) - P_3(z)E_{effxy3}(z)\big)\Big]\Big]
\end{aligned} \tag{A.33}
$$

where,

$$
\begin{aligned}
PM_1(z) = &\big(P_3(z)^2 + P_4(z)^2\big)\big(M_1(z)P_1(z) + M_2(z)P_2(z)\big) \\
&+ \big(P_1(z)^2 + P_2(z)^2\big)\big(M_3(z)P_3(z) + M_4(z)P_4(z)\big) \\
PM_2(z) = &\big(P_3(z)^2 + P_4(z)^2\big)\big(M_2(z)P_1(z) - M_1(z)P_2(z)\big) \\
&- \big(P_1(z)^2 + P_2(z)^2\big)\big(M_4(z)P_3(z) - M_3(z)P_4(z)\big)
\end{aligned}
$$

Now, we determine the local field components at the tip position considering the explicit

forms of the green's function.

$$\mathbf{E}^{loc}(\mathbf{r}_{tip}) = \mathbf{E}^{inc}(\mathbf{r}_{tip}) + \frac{1}{4\pi\varepsilon_0|z|^3}(3\hat{\mathbf{z}}\hat{\mathbf{z}} - \underline{\mathbf{I}}) \cdot \mathbf{p}_{img} + \frac{3i\omega\mu_0}{4\pi k^2}\left(\frac{\hat{\mathbf{y}}\hat{\mathbf{x}} - \hat{\mathbf{x}}\hat{\mathbf{y}}}{|z|^4}\right) \cdot \mathbf{m}_{img}$$

$$\mathbf{H}^{loc}(\mathbf{r}_{tip}) = \mathbf{H}^{inc}(\mathbf{r}_{tip}) - \frac{3i\omega}{4\pi k^2}\left(\frac{\hat{\mathbf{y}}\hat{\mathbf{x}} - \hat{\mathbf{x}}\hat{\mathbf{y}}}{|z|^4}\right) \cdot \mathbf{p}_{img} + \frac{1}{4\pi|z|^3}(3\hat{\mathbf{z}}\hat{\mathbf{z}} - \underline{\mathbf{I}}) \cdot \mathbf{m}_{img}$$

Separating the 'x', 'y' and 'z' components of the local fields at the tip position, we get:

$$E_x^{loc}(\mathbf{r}_{tip}) = E_x^{inc}(\mathbf{r}_{tip}) - \frac{1}{4\pi\varepsilon_0|z|^3}p_{img,x} - \frac{3i\omega\mu_0}{4\pi k^2|z|^4}m_{img,y} \tag{A.34}$$

$$E_y^{loc}(\mathbf{r}_{tip}) = E_y^{inc}(\mathbf{r}_{tip}) - \frac{1}{4\pi\varepsilon_0|z|^3}p_{img,y} + \frac{3i\omega\mu_0}{4\pi k^2|z|^4}m_{img,x} \tag{A.35}$$

$$E_z^{loc}(\mathbf{r}_{tip}) = E_z^{inc}(\mathbf{r}_{tip}) + \frac{2}{4\pi\varepsilon_0|z|^3}p_{img,z} \tag{A.36}$$

$$H_x^{loc}(\mathbf{r}_{tip}) = H_x^{inc}(\mathbf{r}_{tip}) + \frac{3i\omega}{4\pi k^2|z|^4}p_{img,y} - \frac{1}{4\pi|z|^3}m_{img,x} \tag{A.37}$$

$$H_y^{loc}(\mathbf{r}_{tip}) = H_y^{inc}(\mathbf{r}_{tip}) - \frac{3i\omega}{4\pi k^2|z|^4}p_{img,x} - \frac{1}{4\pi|z|^3}m_{img,y} \tag{A.38}$$

$$H_z^{loc}(\mathbf{r}_{tip}) = H_z^{inc}(\mathbf{r}_{tip}) + \frac{2}{4\pi|z|^3}m_{img,z} \tag{A.39}$$

Now, inserting equations A.34-A.39 into A.1 and A.2 we get the 'x', 'y' and 'z' components

of the tip dipole moment.

$$p_{tip,x} = \alpha_{ee} E_x^{inc}(\mathbf{r}_{tip}) - \frac{1}{4\pi\varepsilon_0|z|^3}\alpha_{ee} p_{img,x} - \frac{3i\omega\mu_0}{4\pi k^2|z|^4}\alpha_{ee} m_{img,y} \tag{A.40}$$
$$+ \alpha_{em} H_x^{inc}(\mathbf{r}_{tip}) + \frac{3i\omega}{4\pi k^2|z|^4}\alpha_{em} p_{img,y} - \frac{1}{4\pi|z|^3}\alpha_{em} m_{img,x}$$

$$p_{tip,y} = \alpha_{ee} E_y^{inc}(\mathbf{r}_{tip}) - \frac{1}{4\pi\varepsilon_0|z|^3}\alpha_{ee} p_{img,y} + \frac{3i\omega\mu_0}{4\pi k^2|z|^4}\alpha_{ee} m_{img,x} \tag{A.41}$$
$$+ \alpha_{em} H_y^{inc}(\mathbf{r}_{tip}) - \frac{3i\omega}{4\pi k^2|z|^4}\alpha_{em} p_{img,x} - \frac{1}{4\pi|z|^3}\alpha_{em} m_{img,y}$$

$$p_{tip,z} = \alpha_{ee} E_z^{inc}(\mathbf{r}_{tip}) + \frac{2}{4\pi\varepsilon_0|z|^3}\alpha_{ee} p_{img,z} + \alpha_{em} H_z^{inc}(\mathbf{r}_{tip}) \tag{A.42}$$
$$+ \frac{2}{4\pi|z|^3}\alpha_{em} m_{img,z}$$

$$m_{tip,x} = -\mu_0^{-1}\alpha_{em} E_x^{inc}(\mathbf{r}_{tip}) + \frac{1}{4\pi\varepsilon_0|z|^3}\mu_0^{-1}\alpha_{em} p_{img,x} + \frac{3i\omega\mu_0}{4\pi k^2|z|^4}\mu_0^{-1}\alpha_{em} m_{img,y} \tag{A.43}$$
$$+ \alpha_{mm} H_x^{inc}(\mathbf{r}_{tip}) + \frac{3i\omega}{4\pi k^2|z|^4}\alpha_{mm} p_{img,y} - \frac{1}{4\pi|z|^3}\alpha_{mm} m_{img,x}$$

$$m_{tip,y} = -\mu_0^{-1}\alpha_{em} E_y^{inc}(\mathbf{r}_{tip}) + \frac{1}{4\pi\varepsilon_0|z|^3}\mu_0^{-1}\alpha_{em} p_{img,y} - \frac{3i\omega\mu_0}{4\pi k^2|z|^4}\mu_0^{-1}\alpha_{em} m_{img,x} \tag{A.44}$$
$$+ \alpha_{mm} H_y^{inc}(\mathbf{r}_{tip}) - \frac{3i\omega}{4\pi k^2|z|^4}\alpha_{mm} p_{img,x} - \frac{1}{4\pi|z|^3}\alpha_{mm} m_{img,y}$$

$$m_{tip,z} = -\mu_0^{-1}\alpha_{em} E_z^{inc}(\mathbf{r}_{tip}) - \frac{2}{4\pi\varepsilon_0|z|^3}\mu_0^{-1}\alpha_{em} p_{img,z} + \alpha_{mm} H_x^{inc}(\mathbf{r}_{tip}) \tag{A.45}$$
$$+ \frac{2}{4\pi|z|^3}\alpha_{mm} m_{img,z}$$

A.3 Approximations

At this point, we apply some approximations. First, after performing the Taylor expansion on the terms with negative (-1) power in the expressions of p_{img} and m_{img} in equations A.40-A.45, we ignore all the terms containing polarizability power order higher than two. With

the approximation applied, equations A.28 and A.29 become as below.

$$p_{img,z} \approx E_{effz1}(z) = \alpha_{ee}E_z^{inc}(\mathbf{r}_{img}) + \alpha_{em}H_z^{inc}(\mathbf{r}_{img}) + \frac{2a_1}{|z|^3}E_z^{inc}(\mathbf{r}_{tip}) + \frac{2d_1}{|z|^3}H_z^{inc}(\mathbf{r}_{tip}) \tag{A.46}$$

$$m_{img,z} \approx E_{effz2}(z) = -\mu_o^{-1}\alpha_{em}E_z^{inc}(\mathbf{r}_{img}) + \alpha_{mm}H_z^{inc}(\mathbf{r}_{img}) - \frac{2\mu_0^{-1}d_1}{|z|^3}E_z^{inc}(\mathbf{r}_{tip}) + \frac{2a_4}{|z|^3}H_z^{inc}(\mathbf{r}_{tip}) \tag{A.47}$$

To apply the above approximation on Eq. A.30 and A.31, we cancel all the terms that contain $\left[M_1(z)^2 + M_2(z)^2\right]$ and all the terms that does not contain any $P_1(z)$. Because those terms will have polarizability power order higher than two. Doing so, we get equations A.30 and A.31 become simplified as:

$$p_{img,x} \approx P_1(z)^{-1}E_{effxy1}(z) \approx E_{effxy1}(z) = \alpha_{ee}E_x^{inc}(\mathbf{r}_{img}) + \alpha_{em}H_x^{inc}(\mathbf{r}_{img}) - \frac{a_1}{|z|^3}E_x^{inc}(\mathbf{r}_{tip}) + \frac{e_1}{|z|^4}E_y^{inc}(\mathbf{r}_{tip}) - \frac{d_1}{|z|^3}H_x^{inc}(\mathbf{r}_{tip}) - \frac{b_1}{|z|^4}H_y^{inc}(\mathbf{r}_{tip}) \tag{A.48}$$

$$p_{img,y} \approx P_1(z)^{-1}E_{effxy2}(z) \approx E_{effxy2}(z) = \alpha_{ee}E_y^{inc}(\mathbf{r}_{img}) + \alpha_{em}H_y^{inc}(\mathbf{r}_{img}) - \frac{e_1}{|z|^3}E_x^{inc}(\mathbf{r}_{tip}) - \frac{a_1}{|z|^4}E_y^{inc}(\mathbf{r}_{tip}) + \frac{b_1}{|z|^3}H_x^{inc}(\mathbf{r}_{tip}) - \frac{d_1}{|z|^4}H_y^{inc}(\mathbf{r}_{tip}) \tag{A.49}$$

Similarly, to apply the above approximation on Eq. A.32 and A.33, we cancel all the terms that contain $\left[P_3(z)^2 + P_4(z)^2\right]$ and all the terms that does not contain any $M_3(z)$. Because those terms will have polarizability power order higher than two. Thus equations A.32 and

A.33 become simplified as A.50 and A.51:

$$m_{img,x} \approx M_3(z)^{-1} E_{effxy3}(z) \approx E_{effxy3}(z) = -\mu_0^{-1}\alpha_{em} E_x^{inc}(\mathbf{r}_{img}) + \alpha_{mm} H_x^{inc}(\mathbf{r}_{img}) + \frac{\mu_0^{-1} d_1}{|z|^3} E_x^{inc}(\mathbf{r}_{tip}) + \frac{\mu_0^{-1} b_1}{|z|^4} E_y^{inc}(\mathbf{r}_{tip}) - \frac{a_4}{|z|^3} H_x^{inc}(\mathbf{r}_{tip}) + \frac{e_4}{|z|^4} H_y^{inc}(\mathbf{r}_{tip}) \quad (A.50)$$

$$m_{img,y} \approx M_3(z)^{-1} E_{effxy4}(z) \approx E_{effxy4}(z) = -\mu_0^{-1}\alpha_{em} E_y^{inc}(\mathbf{r}_{img}) + \alpha_{mm} H_y^{inc}(\mathbf{r}_{img}) - \frac{\mu_0^{-1} b_1}{|z|^3} E_x^{inc}(\mathbf{r}_{tip}) + \frac{\mu_0^{-1} d_1}{|z|^4} E_y^{inc}(\mathbf{r}_{tip}) - \frac{e_4}{|z|^3} H_x^{inc}(\mathbf{r}_{tip}) - \frac{a_4}{|z|^4} H_y^{inc}(\mathbf{r}_{tip}) \quad (A.51)$$

Now, we can calculate the 'z' component of the force as:

$$\begin{aligned} \langle \mathrm{F}_z \rangle &= \langle \mathrm{F}_{z,e} \rangle + \langle \mathrm{F}_{z,m} \rangle + \langle \mathrm{F}_{z,int} \rangle \\ &= \frac{1}{2}\mathrm{Re}\Big\{ p_{tip,x}\big(\partial_z E_x^{loc}(\mathbf{r}_{tip})\big)^* + p_{tip,y}\big(\partial_z E_y^{loc}(\mathbf{r}_{tip})\big)^* + p_{tip,z}\big(\partial_z E_z^{loc}(\mathbf{r}_{tip})\big)^* \Big\} \quad (A.52) \\ &+ \frac{1}{2}\mu_0 \mathrm{Re}\Big\{ m_{tip,x}\big(\partial_z H_x^{loc}(\mathbf{r}_{tip})\big)^* + m_{tip,y}\big(\partial_z H_y^{loc}(\mathbf{r}_{tip})\big)^* + m_{tip,z}\big(\partial_z H_z^{loc}(\mathbf{r}_{tip})\big)^* \Big\} \\ &- \frac{1}{2}\mathrm{Re}\Big\{ \frac{c\mu_0 k^4}{6\pi}(p_{tip,x} m_{tip,y}^* - p_{tip,y} m_{tip,x}^*) \Big\} \end{aligned}$$

Here, we have split the total force into three parts as electric dipolar force $\langle \mathrm{F}_{z,e} \rangle$, magnetic dipolar force $\langle \mathrm{F}_{z,m} \rangle$ and interaction force $\langle \mathrm{F}_{z,int} \rangle$. Now, to calculate the force, with the same approximation of ignoring all the terms containing polarizability power order higher than two, it is suffice to consider the tip dipole moments definition as shown below.

$$p_{tip,x} = \alpha_{ee} E_x^{inc}(\mathbf{r}_{tip}) + \alpha_{em} H_x^{inc}(\mathbf{r}_{tip}) \quad (A.53)$$

$$p_{tip,y} = \alpha_{ee} E_y^{inc}(\mathbf{r}_{tip}) + \alpha_{em} H_y^{inc}(\mathbf{r}_{tip}) \quad (A.54)$$

$$p_{tip,z} = \alpha_{ee} E_z^{inc}(\mathbf{r}_{tip}) + \alpha_{em} H_z^{inc}(\mathbf{r}_{tip}) \quad (A.55)$$

$$m_{tip,x} = -\mu_0^{-1}\alpha_{em} E_x^{inc}(\mathbf{r}_{tip}) + \alpha_{mm} H_x^{inc}(\mathbf{r}_{tip}) \quad (A.56)$$

$$m_{tip,y} = -\mu_0^{-1}\alpha_{em} E_y^{inc}(\mathbf{r}_{tip}) + \alpha_{mm} H_y^{inc}(\mathbf{r}_{tip}) \quad (A.57)$$

$$m_{tip,z} = -\mu_0^{-1}\alpha_{em} E_z^{inc}(\mathbf{r}_{tip}) + \alpha_{mm} H_z^{inc}(\mathbf{r}_{tip}) \quad (A.58)$$

At this point we consider the proper sign in the image dipole moments in the field definitions of equations A.34-A.39 with electro-magnetic polarizability $\alpha_{em}^{img} = -\alpha_{em}$. Furthermore, in determining the field gradient for force calculation from Eq. A.52, we neglect the incident field as the gradient of the distant dependent scattered field would be stronger. In addition to these, with the approximation of ignoring all the terms containing polarizability power order higher than two, it is suffice to consider the local field at the tip position as expressed in A.59-A.64.

$$E_x^{loc}(\mathbf{r}_{tip}) = -\frac{1}{4\pi\varepsilon_0|z|^3}\left[\alpha_{ee}E_x^{inc}(\mathbf{r}_{img}) - \alpha_{em}H_x^{inc}(\mathbf{r}_{img})\right] \tag{A.59}$$
$$- \frac{3i\omega\mu_0}{4\pi k^2|z|^4}\left[\mu_0^{-1}\alpha_{em}E_y^{inc}(\mathbf{r}_{img}) + \alpha_{mm}H_y^{inc}(\mathbf{r}_{img})\right]$$
$$E_y^{loc}(\mathbf{r}_{tip}) = -\frac{1}{4\pi\varepsilon_0|z|^3}\left[\alpha_{ee}E_y^{inc}(\mathbf{r}_{img}) - \alpha_{em}H_y^{inc}(\mathbf{r}_{img})\right] \tag{A.60}$$
$$+ \frac{3i\omega\mu_0}{4\pi k^2|z|^4}\left[\mu_0^{-1}\alpha_{em}E_x^{inc}(\mathbf{r}_{img}) + \alpha_{mm}H_x^{inc}(\mathbf{r}_{img})\right]$$
$$E_z^{loc}(\mathbf{r}_{tip}) = \frac{2}{4\pi\varepsilon_0|z|^3}\left[\alpha_{ee}E_z^{inc}(\mathbf{r}_{img}) - \alpha_{em}H_z^{inc}(\mathbf{r}_{img})\right] \tag{A.61}$$
$$H_x^{loc}(\mathbf{r}_{tip}) = +\frac{3i\omega}{4\pi k^2|z|^4}\left[\alpha_{ee}E_y^{inc}(\mathbf{r}_{img}) - \alpha_{em}H_y^{inc}(\mathbf{r}_{img})\right] \tag{A.62}$$
$$- \frac{1}{4\pi|z|^3}\left[\mu_0^{-1}\alpha_{em}E_x^{inc}(\mathbf{r}_{img}) + \alpha_{mm}H_x^{inc}(\mathbf{r}_{img})\right]$$
$$H_y^{loc}(\mathbf{r}_{tip}) = -\frac{3i\omega}{4\pi k^2|z|^4}\left[\alpha_{ee}E_x^{inc}(\mathbf{r}_{img}) - \alpha_{em}H_x^{inc}(\mathbf{r}_{img})\right] \tag{A.63}$$
$$- \frac{1}{4\pi|z|^3}\left[\mu_0^{-1}\alpha_{em}E_y^{inc}(\mathbf{r}_{img}) + \alpha_{mm}H_y^{inc}(\mathbf{r}_{img})\right]$$
$$H_z^{loc}(\mathbf{r}_{tip}) = \frac{2}{4\pi|z|^3}\left[\mu_0^{-1}\alpha_{em}E_z^{inc}(\mathbf{r}_{img}) + \alpha_{mm}H_z^{inc}(\mathbf{r}_{img})\right] \tag{A.64}$$

Next we impose the field reflection rules by considering $\mathbf{E}_t^{inc}(\mathbf{r}_{tip}) = -\mathbf{E}_t^{inc}(\mathbf{r}_{img}) = \mathbf{E}_t^{inc}$, $\mathbf{E}_z^{inc}(\mathbf{r}_{tip}) = \mathbf{E}_z^{inc}(\mathbf{r}_{img}) = \mathbf{E}_z^{inc}$, $\mathbf{H}_t^{inc}(\mathbf{r}_{tip}) = \mathbf{H}_t^{inc}(\mathbf{r}_{img}) = \mathbf{H}_t^{inc}$and $\mathbf{H}_z^{inc}(\mathbf{r}_{tip}) = -\mathbf{H}_z^{inc}(\mathbf{r}_{img}) = \mathbf{H}_z^{inc}$. Here, we ignore the phase difference of the incident beam at the tip dipole and image dipole location due to its sub-wavelength distance. Imposing the field reflection rules in addition to ignoring all the terms containing polarizability power order higher than two and

insering equations A.53-A.58 and equations A.59-A.64 in the A.52 we find the different force components as shown below.

$$\begin{aligned}\langle F_{z,e}\rangle = -\frac{3}{2\pi|z|^4}\Bigg\{&\frac{1}{2}\frac{|\alpha_{ee}|^2}{\varepsilon_0}(\frac{1}{2}|\mathbf{E}_t^{inc}|^2+|\mathbf{E}_z^{inc}|^2)+\frac{1}{2}\frac{|\alpha_{em}|^2}{\varepsilon_0}(\frac{1}{2}|\mathbf{H}_t^{inc}|^2+|\mathbf{H}_z^{inc}|^2)\\&+\mathrm{Re}\Big(\frac{\alpha_{ee}\alpha_{em}^*}{\varepsilon_0}(\frac{1}{2}\mathbf{E}_t^{inc}\cdot\mathbf{H}_t^{inc*}+\mathbf{E}_z^{inc}\cdot\mathbf{H}_z^{inc*})\Big)\Bigg\}\\+\frac{3\omega}{\pi k^2|z|^5}\Bigg\{&\mathrm{Re}(\mu_0\alpha_{em}\alpha_{mm}^*)\mathrm{Im}(H_x^{inc}H_y^{inc*})-\mathrm{Re}(\alpha_{ee}\alpha_{em}^*)\mathrm{Im}(E_x^{inc}E_y^{inc*})\\&-\frac{1}{2}\mathrm{Re}\Big(i\mu_0\alpha_{ee}\alpha_{mm}^*E_x^{inc}H_y^{inc*}-i|\alpha_{em}|^2H_x^{inc}E_y^{inc*}\\&-i\mu_0\alpha_{ee}\alpha_{mm}^*E_y^{inc}H_x^{inc*}+i|\alpha_{em}|^2H_y^{inc}E_x^{inc*}\Big)\Bigg\}\end{aligned}\tag{A.65}$$

$$\begin{aligned}\langle F_{z,m}\rangle = \frac{3}{2\pi|z|^4}\Bigg\{&\frac{1}{2}(\mu_0|\mu_0^{-1}\alpha_{em}|^2)(\frac{1}{2}|\mathbf{E}_t^{inc}|^2+|\mathbf{E}_z^{inc}|^2)+\frac{1}{2}(\mu_0|\alpha_{mm}|^2)(\frac{1}{2}|\mathbf{H}_t^{inc}|^2+|\mathbf{H}_z^{inc}|^2)\\&-\mathrm{Re}\Big(\alpha_{mm}^*\alpha_{em}(\frac{1}{2}\mathbf{E}_t^{inc}\cdot\mathbf{H}_t^{inc*}+\mathbf{E}_z^{inc}\cdot\mathbf{H}_z^{inc*})\Big)\Bigg\}\\-\frac{3\omega}{\pi k^2|z|^5}\Bigg\{&\mathrm{Re}(\alpha_{em}\alpha_{ee}^*)\mathrm{Im}(E_x^{inc}E_y^{inc*})-\mathrm{Re}(\mu_0\alpha_{mm}\alpha_{em}^*)\mathrm{Im}(H_x^{inc}H_y^{inc*})\\&-\frac{1}{2}\mathrm{Re}\Big(i|\alpha_{em}|^2E_x^{inc}H_y^{inc*}-i\mu_0\alpha_{mm}\alpha_{ee}^*H_x^{inc}E_y^{inc*}\\&-i|\alpha_{em}|^2E_y^{inc}H_x^{inc*}+i\mu_0\alpha_{mm}\alpha_{ee}^*H_y^{inc}E_x^{inc*}\Big)\Bigg\}\end{aligned}\tag{A.66}$$

$$\begin{aligned}\langle F_{z,int}\rangle = -\frac{ck^4}{12\pi}\Bigg\{&\mathrm{Re}(-\alpha_{em}^*\alpha_{ee})\mathrm{Re}[\mathbf{E}_t^{inc}\times\mathbf{E}_t^{inc*}]_z-\mathrm{Im}(-\alpha_{em}^*\alpha_{ee})\mathrm{Im}[\mathbf{E}_t^{inc}\times\mathbf{E}_t^{inc*}]_z\\&+\mathrm{Re}(\alpha_{em}^*\alpha_{em}[\mathbf{E}_t^{inc*}\times\mathbf{H}_t^{inc}]_z)+\mathrm{Re}(\mu_0\alpha_{mm}^*\alpha_{ee}[\mathbf{E}_t^{inc}\times\mathbf{H}_t^{inc*}]_z\\&+\mathrm{Re}(\mu_0\alpha_{mm}^*\alpha_{em})\mathrm{Re}[\mathbf{H}_t^{inc}\times\mathbf{H}_t^{inc*}]_z\\&-\mathrm{Im}(\mu_0\alpha_{mm}^*\alpha_{em})\mathrm{Im}[\mathbf{H}_t^{inc}\times\mathbf{H}_t^{inc*}]_z\Bigg\}\end{aligned}\tag{A.67}$$

where $\mathbf{E}_t^{inc} = E_x^{inc}\hat{\mathbf{x}} + E_y^{inc}\hat{\mathbf{y}}$,$\mathbf{H}_t^{inc} = H_x^{inc}\hat{\mathbf{x}} + H_y^{inc}\hat{\mathbf{y}}$ and $\mathbf{E}_z^{inc} = E_z^{inc}\hat{\mathbf{z}}$, $\mathbf{H}_z^{inc} = H_z^{inc}\hat{\mathbf{z}}$ are the transverse and longitudinal components of the incident electric and magnetic field. Now, we add A.65 and A.66 to get A.68

$$
\begin{aligned}
\langle F_{z,grad}\rangle &= \langle F_{z,e}\rangle + \langle F_{z,m}\rangle \\
&= \frac{3}{2\pi|z|^4}\Bigg\{\frac{1}{2}\Big(-\frac{|\alpha_{ee}|^2}{\varepsilon_0} + \mu_0|\mu_0^{-1}\alpha_{em}|^2\Big)\Big(\frac{1}{2}|\mathbf{E}_t^{inc}|^2 + |\mathbf{E}_z^{inc}|^2\Big) \\
&\qquad + \frac{1}{2}\Big(-\frac{|\alpha_{em}|^2}{\varepsilon_0} + \mu_0|\alpha_{mm}|^2\Big)\Big(\frac{1}{2}|\mathbf{H}_t^{inc}|^2 + |\mathbf{H}_z^{inc}|^2\Big) \\
&\qquad - \mathrm{Re}\Big(\Big(\frac{\alpha_{ee}\alpha_{em}^*}{\varepsilon_0} + \alpha_{mm}^*\alpha_{em}\Big)\Big(\frac{1}{2}\mathbf{E}_t^{inc}\cdot\mathbf{H}_t^{inc*} + \mathbf{E}_z^{inc}\cdot\mathbf{H}_z^{inc*}\Big)\Big)\Bigg\} \\
&+ \frac{6\omega}{\pi k^2|z|^5}\Bigg\{\mathrm{Re}(\mu_0\alpha_{em}\alpha_{mm}^*)\mathrm{Im}(H_x^{inc}H_y^{inc*}) - \mathrm{Re}(\alpha_{ee}\alpha_{em}^*)\mathrm{Im}(E_x^{inc}E_y^{inc*}) \\
&\qquad - 2\mathrm{Im}\Big(\big(|\alpha_{em}|^2 - \mu_0\alpha_{ee}\alpha_{mm}^*\big)[\mathbf{S}^{inc}]_z\Big)\Bigg\}
\end{aligned}
\tag{A.68}
$$

Here, we replace the time average poynting vector of the incident field $\mathbf{S}^{inc} = \frac{1}{2}\mathbf{E}^{inc} \times \mathbf{H}^{inc*}$. Now, replacing the electric and magnetic part of the time average total spin angular momentum of the incident light defined as $\boldsymbol{\sigma}^{inc} = \boldsymbol{\sigma}_E^{inc} + \boldsymbol{\sigma}_H^{inc} = -\frac{\varepsilon_0}{4\omega i}(\mathbf{E}^{inc}\times\mathbf{E}^{inc*}) - \frac{\mu_0}{4\omega i}(\mathbf{H}^{inc}\times\mathbf{H}^{inc*})$ in equation A.67, we get:

$$
\begin{aligned}
\langle F_{z,int}\rangle = -\frac{ck^4}{12\pi}\Bigg\{&\mathrm{Re}(-\alpha_{em}^*\alpha_{ee})\mathrm{Re}[\mathbf{E}_t^{inc}\times\mathbf{E}_t^{inc*}]_z + 4\omega\mathrm{Im}\Big(-\frac{\alpha_{em}^*\alpha_{ee}}{\varepsilon_0}\Big)[\boldsymbol{\sigma}_E^{inc}]_z \\
&+ 2\mathrm{Re}(\alpha_{em}^*\alpha_{em}[\mathbf{S}^{inc*}]_z) + 2\mathrm{Re}(\mu_0\alpha_{mm}^*\alpha_{ee}[\mathbf{S}^{inc}]_z) \\
&+ \mathrm{Re}(\mu_0\alpha_{mm}^*\alpha_{em})\mathrm{Re}[\mathbf{H}_t^{inc}\times\mathbf{H}_t^{inc*}]_z + 4\omega\mathrm{Im}(-\alpha_{mm}\alpha_{em}^*)[\boldsymbol{\sigma}_H^{inc}]_z\Bigg\}
\end{aligned}
\tag{A.69}
$$

We next determine the differential force, obtained by measuring the force under illumination with incident light of (+) and (−) handedness, and taking the difference. Under these conditions, the differential gradient force $\Delta\langle F_{z,grad}\rangle = \langle F_{z,grad}\rangle^+ - \langle F_{z,grad}\rangle^-$ and the differential scattering force $\Delta\langle F_{z,int}\rangle = \langle F_{z,int}\rangle^+ - \langle F_{z,int}\rangle^-$ can be obtained from equations (A.68) and

(A.69).

$$\begin{aligned}\Delta\langle F_{z,grad}\rangle &= \frac{6\omega c}{\pi|z|^4}\mathrm{Im}\Big\{\frac{\alpha_{ee}\alpha_{em}^*}{\varepsilon_0}-\alpha_{mm}\alpha_{em}^*\Big\}\Big(\frac{1}{2}h_{\parallel}^{inc}+h_z^{inc}\Big)\\ &+\frac{24\omega^2}{\pi k^2|z|^5}\left\{\mathrm{Re}(\frac{\alpha_{ee}\alpha_{em}^*}{\varepsilon_0})[\boldsymbol{\sigma}_E^{inc}]_z-\mathrm{Re}(\alpha_{mm}\alpha_{em}^*)[\boldsymbol{\sigma}_H^{inc}]_z\right\}\end{aligned} \tag{A.70}$$

$$\Delta\langle F_{z,int}\rangle = -\frac{2\omega c k^4}{3\pi}\Big[\mathrm{Im}\Big\{-\frac{\alpha_{em}^*\alpha_{ee}}{\varepsilon_0}\Big\}[\boldsymbol{\sigma}_E^{inc}]_z+\mathrm{Im}\Big\{-\alpha_{mm}\alpha_{em}^*\Big\}[\boldsymbol{\sigma}_H^{inc}]_z\Big] \tag{A.71}$$

A.4 Comparison of z^{-4} and z^{-5} dependent terms of $\Delta\langle F_{z,grad}\rangle$ in Eq. 4.16

Here, we compare the z^{-4} and z^{-5} distance dependent terms of $\Delta\langle F_{z,grad}\rangle$ in Eq. 4.16 from the main text. The z^{-5} term contains the electric and magnetic part of the spin angular momentum density $[\boldsymbol{\sigma}_E^{inc+}]_z$ and $[\boldsymbol{\sigma}_H^{inc+}]_z$. For an optimally chiral beam, such as a circularly polarized (CP) beam, we have $[\boldsymbol{\sigma}_E^{inc+}]_z = [\boldsymbol{\sigma}_H^{inc+}]_z$. This in turn makes it possible to compare the strength of the z^{-4} and z^{-5} dependent term just by calculating the real and imaginary part of the quantity $\alpha = \frac{\alpha_{em}^*}{\varepsilon_0}(\alpha_{ee}-\varepsilon_0\alpha_{mm})$. When analyzing the first and the second terms in equation (A.70) we must observe that for deeply sub-wavelength nanoparticles and non very lossy material like Silicon, the polarizabilities α_{ee} and α_{mm} assume mainly real values. Assuming the same particle has chirality, we also observe that α_{em} is mainly imaginary (see for example the expression (9) in Ref. [114] or (7) in Ref.[115]). Therefore, when the deep sub-wavelength chiral tip is made of low-loss material, the term $\mathrm{Im}(\alpha)$ is larger than the term $\mathrm{Re}(\alpha)$.

To provide an idea of the values of the imaginary and real parts of α for a practical size (not deeply sub-wavelength) of the tip, we consider an isotropic chiral scatterer with material

properties, ε_r and μ_r same as crystalline silicon with $\mu_r = 1$ and $\kappa = 0.1$. Figure A.2 (a), (b) and (c) show the spectral behavior of real(solid) and imaginary(dashed) part of α for three different radius r_{NP} of 60 nm, 70 nm and 80 nm. We clearly see that the imaginary part peaks at the respective resonant wavelength of α_{em}. The peak value of the imaginary part gets higher for increasing radii whereas the real part is small and remains invariant with radius. Besides, for higher radii, $k|z|$ approaches unity, which further decreases the pre-factor of the z^{-5} term compared to the z^{-4} term. These effects add to the dominance of the z^{-4} term over the z^{-5} term, particularly at larger radii of the chiral scatterer.

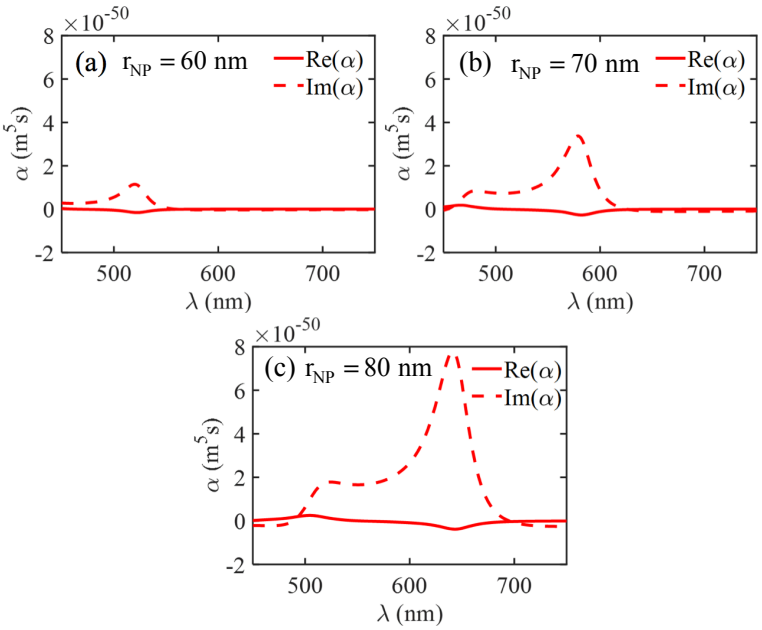

Figure A.2: Here, $\alpha = \frac{\alpha^*_{em}}{\varepsilon_0}(\alpha_{ee} - \varepsilon_0\alpha_{mm})$. Spectral response of real(solid) and imaginary(dashed) part of α for an isotropic chiral scatterer of radius (a) $r_{NP} = 60$ nm, (b) $r_{NP} = 70$ nm and (c) $r_{NP} = 80$ nm . The material properties of the chiral NP, ε_r and μ_r are considered same as silicon with $\mu_r = 1$ and $\kappa = 0.1$

A.5 Calculation of $\Delta\langle F_{z,grad}\rangle$ for the helical-shaped tip

Generally, chiral nanoprobes are made by engraving spiral feature on regular tips [13, 99]. Here, we calculate the longitudinal force felt by a chiral tip that could be made through helical carvings on regular achiral tips, but here it is modeled as an object with an anisotropic chiral polarizability. In the point dipole approximation, the chiral tip is defined as a point dipole with both electric and magnetic polarizabilities together with an electromagnetic polarizability. Using this description, in Section A.1 we considered the case of an isotropic chiral particle, whereas here we consider its anisotropic counterpart. The spiral feature enables circular displacement current upon proper light illumination. This in turn produces the induced magnetic dipole with electro-magnetic coupling. The point electric dipole moment and magnetic dipole moment defining the chiral dipole can be expressed as

$$\mathbf{p}_{tip} = \underline{\boldsymbol{\alpha}}_{ee} \cdot \mathbf{E}^{loc}(\mathbf{r}_{tip}) + \underline{\boldsymbol{\alpha}}_{em} \cdot \mathbf{H}^{loc}(\mathbf{r}_{tip}) \tag{A.72}$$

$$\mathbf{m}_{tip} = \mu_0^{-1}\underline{\boldsymbol{\alpha}}_{me} \cdot \mathbf{E}^{loc}(\mathbf{r}_{tip}) + \underline{\boldsymbol{\alpha}}_{mm} \cdot \mathbf{H}^{loc}(\mathbf{r}_{tip}) \tag{A.73}$$

where, $\underline{\boldsymbol{\alpha}}_{ee}$, $\underline{\boldsymbol{\alpha}}_{mm}$, $\underline{\boldsymbol{\alpha}}_{em}$ and $\underline{\boldsymbol{\alpha}}_{em}$ are the dyadic electric, magnetic and electromagnetic and magneto-electric polarizabilities. Due to reciprocity principal, they follow the relations $\underline{\boldsymbol{\alpha}}_{ee} = \underline{\boldsymbol{\alpha}}_{ee}^T$, $\underline{\boldsymbol{\alpha}}_{mm} = \underline{\boldsymbol{\alpha}}_{mm}^T$ and $\underline{\boldsymbol{\alpha}}_{em} = -\underline{\boldsymbol{\alpha}}_{me}^T$[128, 116]. For a helix particle, the polarizability dyadics can have the following form [128],

$$\begin{aligned}
&\underline{\boldsymbol{\alpha}}_{ee} = \alpha_{ee}^{zz}\hat{\mathbf{z}}\hat{\mathbf{z}};\\
&\underline{\boldsymbol{\alpha}}_{mm} = \alpha_{mm}^{zz}\hat{\mathbf{z}}\hat{\mathbf{z}}\\
&\underline{\boldsymbol{\alpha}}_{em} = \alpha_{em}^{zz}\hat{\mathbf{z}}\hat{\mathbf{z}}\\
&\underline{\boldsymbol{\alpha}}_{me} = -\alpha_{em}^{zz}\hat{\mathbf{z}}\hat{\mathbf{z}}
\end{aligned} \tag{A.74}$$

Next, we apply image-dipole theorem, discussed in Section A.1, to calculate the local field at the tip position. We consider the substrate to be a perfectly electric conductor and substitute

its effect by an image electric and magnetic dipoles with the dipole moments stated below:

$$\mathbf{p}_{img} = \underline{\boldsymbol{\alpha}}_{ee}^{img} \cdot \mathbf{E}^{loc}(\mathbf{r}_{img}) + \underline{\boldsymbol{\alpha}}_{em}^{img} \cdot \mathbf{H}^{loc}(\mathbf{r}_{img}) \tag{A.75}$$

$$\mathbf{m}_{img} = \mu_0^{-1} \underline{\boldsymbol{\alpha}}_{me}^{img} \cdot \mathbf{E}^{loc}(\mathbf{r}_{img}) + \underline{\boldsymbol{\alpha}}_{mm}^{img} \cdot \mathbf{H}^{loc}(\mathbf{r}_{img}) \tag{A.76}$$

Here we have imposed the mirror operation of the chiral object by proper changes in the sign of polarizabity dyadic given as

$$\begin{aligned}
\underline{\boldsymbol{\alpha}}_{ee}^{img} &= \alpha_{ee}^{zz} \hat{\mathbf{z}}\hat{\mathbf{z}}; \\
\underline{\boldsymbol{\alpha}}_{mm}^{img} &= \alpha_{mm}^{zz} \hat{\mathbf{z}}\hat{\mathbf{z}} \\
\underline{\boldsymbol{\alpha}}_{em}^{img} &= -\alpha_{em}^{zz} \hat{\mathbf{z}}\hat{\mathbf{z}} \\
\underline{\boldsymbol{\alpha}}_{me}^{img} &= \alpha_{em}^{zz} \hat{\mathbf{z}}\hat{\mathbf{z}}
\end{aligned} \tag{A.77}$$

If we follow the calculation in section 1 and eventually apply the approximation of ignoring all the terms containing polarizability power order higher than two, it is suffice to consider the tip dipole moments definition and the local field components at the tip position as:

$$p_{tip,z} = \alpha_{ee}^{zz} E_z^{inc}(\mathbf{r}_{tip}) + \alpha_{em}^{zz} H_z^{inc}(\mathbf{r}_{tip}) \tag{A.78}$$

$$m_{tip,z} = -\mu_0^{-1} \alpha_{em}^{zz} E_z^{inc}(\mathbf{r}_{tip}) + \alpha_{mm}^{zz} H_z^{inc}(\mathbf{r}_{tip}) \tag{A.79}$$

$$E_z^{loc}(\mathbf{r}_{tip}) = \frac{2}{4\pi\varepsilon_0 |z|^3} \left[\alpha_{ee}^{zz} E_z^{inc}(\mathbf{r}_{img}) - \alpha_{em}^{zz} H_z^{inc}(\mathbf{r}_{img}) \right] \tag{A.80}$$

$$H_z^{loc}(\mathbf{r}_{tip}) = \frac{2}{4\pi |z|^3} \left[\mu_0^{-1} \alpha_{em}^{zz} E_z^{inc}(\mathbf{r}_{img}) + \alpha_{mm}^{zz} H_z^{inc}(\mathbf{r}_{img}) \right] \tag{A.81}$$

We next impose the field reflection rules by considering $E_x^{inc}(\mathbf{r}_{tip}) = -E_x^{inc}(\mathbf{r}_{img}) = E_x^{inc}$, $E_y^{inc}(\mathbf{r}_{tip}) = -E_y^{inc}(\mathbf{r}_{img}) = E_y^{inc}$, $E_z^{inc}(\mathbf{r}_{tip}) = E_z^{inc}(\mathbf{r}_{img}) = E_z^{inc}$, $H_x^{inc}(\mathbf{r}_{tip}) = H_x^{inc}(\mathbf{r}_{img}) = H_x^{inc}$, $H_y^{inc}(\mathbf{r}_{tip}) = H_y^{inc}(\mathbf{r}_{img}) = H_y^{inc}$and $H_z^{inc}(\mathbf{r}_{tip}) = -H_z^{inc}(\mathbf{r}_{img}) = H_z^{inc}$. Here, we ignore the phase difference of the incident beam between position of the tip and the image due to its sub-wavelength distance. Imposing the above stated relations in addition to ignoring all the terms containing polarizability power order higher than two and insering equations

A.78-A.81 in the A.52 we find the total gradient force:

$$\langle F_{z,grad}\rangle = \langle F_{z,e}\rangle + \langle F_{z,m}\rangle = \frac{3}{2\pi|z|^4}\Bigg\{ + \frac{1}{4}(\frac{-2|\alpha_{ee}^{zz}|^2}{\varepsilon_0} + 2\mu_0|\mu_0^{-1}\alpha_{em}^{zz}|^2)|E_z^{inc}|^2 + \frac{1}{4}(\frac{-2|\alpha_{em}^{zz}|^2}{\varepsilon_0} + 2\mu_0|\alpha_{mm}^{zz}|^2)|H_z^{inc}|^2 - \mathrm{Re}\Big((\frac{\alpha_{ee}^{zz}\alpha_{em}^{zz*}}{\varepsilon_0} + \alpha_{em}^{zz}\alpha_{mm}^{zz*})E_z^{inc}H_z^{inc*}\Big)\Bigg\} \tag{A.82}$$

We next determine the differential force, obtained by measuring the force under illumination with incident light of (+) and (−) handedness, and taking the difference. Under these conditions, the differential gradient force $\Delta\langle F_{z,grad}\rangle = \langle F_{z,grad}\rangle^{+} - \langle F_{z,grad}\rangle^{-}$ becomes

$$\Delta\langle F_{z,grad}\rangle \sim \frac{6\omega c}{\pi|z|^4}\mathrm{Im}\Big\{\frac{\alpha_{ee}^{zz}\alpha_{em}^{zz*}}{\varepsilon_0} - \alpha_{mm}^{zz}\alpha_{em}^{zz*}\Big\}h_z^{inc} \tag{A.83}$$

Appendix B

Spectrum of electromagnetic Mie coefficient, c_1 and effect of κ on $\Delta\langle F_{z,grad}\rangle$

Here, we show the spectrum of the Mie coefficient c_1, that is related to the chiral electromagnetic polarizability as $\alpha_{em} = 6\pi i c_1/(ck_0^3)$ where c is the free space speed of light, and k_0 is the wavenumber in free space. For the force calculation, the nanoparticle is above a glass substrate and is illuminated by CP plane waves (LCP and RCP) from the bottom (i.e., coming from the glass substrate). For very small radii of the NP, c_1 is mainly real and positive, hence α_{em} is mainly imaginary positive.

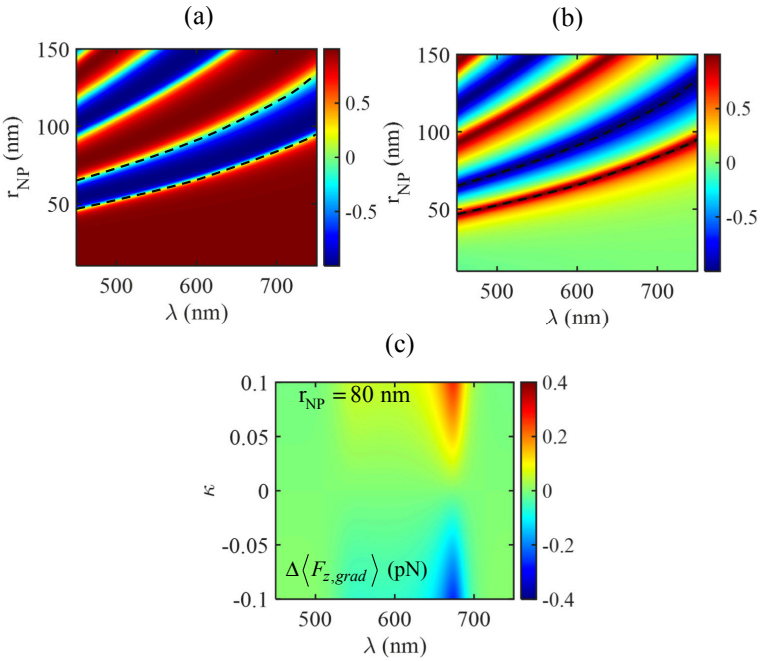

Figure B.1: Spectrum of (a) $\frac{\mathrm{Re}(c_1)}{|c_1|}$ and (b) $\frac{\mathrm{Im}(c_1)}{|c_1|}$ for changing chiral special NP radius at a fixed chirality parameter $\kappa = 0.1$ (c) The gradient difference force spectrum in pN for changing chirality parameter of the chiral NP at $r_{NP} = 80$ nm. The black dotted lines show the resonant peak positions of the electromagnetic Mie coefficient, c_1 for various NP radius. In all calcualions, tip dipole center and image dipole center distance is chosen as $2r_{NP} + 10$ nm

Appendix C

Force difference map of helicity density for a focused ARPB beam

Recently a type of chiral beam called ARPB, which combines two different vector beams namely radially polarized beam (RPB) and azimuthally polarized beam (APB) with certain phase difference between them, has been described in Refs [115, 94, 105]. Similar to Circularly Polarized light, the two ARPB beams of different handedness are obtained as $\mathrm{ARPB}^{\pm} = \mathrm{RPB} + \mathrm{e}^{\pm \mathrm{i}\pi/2}\mathrm{APB}$. We have determined the force difference map of the helicity density of a focused (by 1.4NA oil objective) ARPB beam of 2 mW incident power. Figure C.1(a) and (d) show the respective scheme in which an isotropic chiral scatterer of $r_{NP} = 80$ nm and a helical-shaped tip with equal polarizability strength are scanned on a glass substrate over the area of the focused ARPB^{+} beam.The helical-shaped tip is modeled as an anisotropic chiral polarizable nanoparticle. The isotropic chiral scatterer is chosen to be made of Si, and the anisotropic polarizability values of α_{ee}^{zz}, α_{mm}^{zz} and α_{em}^{zz} for the helical-shaped tip are considered the same as the isotropic polarizability values found for the80 nm Si chiral scatterer.

The normalized helicity density in the focal plane has been determined using the appropriate

electric and magnetic field components from [23] and is shown in C.1(b) for an $ARPB^{+}$ beam. Figure C.1(e) shows the longitudinal component of normalized helicity density in C.1(b). Contrary to the CP beam, ARPB beam shows solid circular longitudinal helicity density as shown in C.1 (e). Like the CP case, the force map for an isotropic scatterer in C.1(c) tracks the total helicity density distributions with an uneven scaling for the transverse and longitudinal component, whereas the force map for the helical-shaped tip in C.1(f) exclusively provides the longitudinal helicity density distribution with a peak force reaching ~ 1.0 pN at the center.

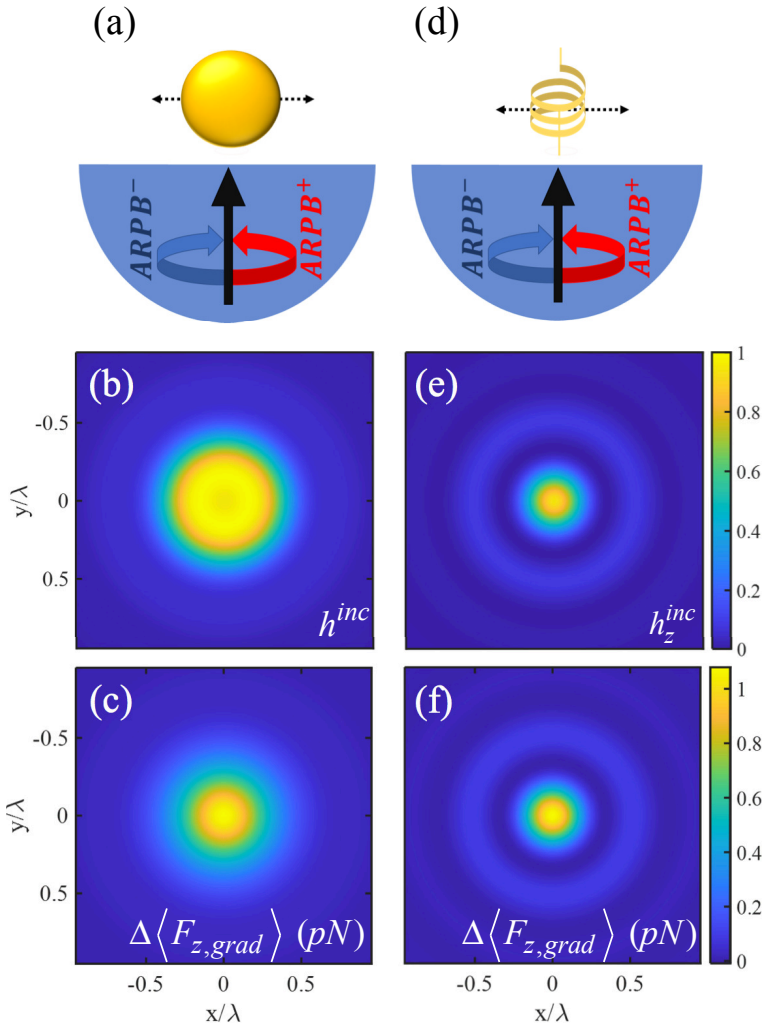

Figure C.1: Schematics describing (a) an isotropic chiral scatterer and (d) a more realistic helically curved tip being horizontally scanned over a glass substrate with a bottom illumination of focused ARPB$^+$ beam. (b) The focal plane distribution of total normalized helicity density of the incident ARPB beam (ARPB$^+$) focused by a 1.4 NA oil objective. (e) Distribution of longitudinal component of the normalized helicity density in (b). (c)The total gradient force difference map at the focal plane for a chiral isotropic tip of radius $r_{NP} = 80$ nm under the same focused illumination of ARPB$^+$ and ARPB$^-$. (f) Force difference map for the helical tip that exhibits significant longitudinal chirality ($\alpha_{em}^{xx} = \alpha_{em}^{yy} = 0$ and $\alpha_{em}^{zz} = \alpha_{em}$) and tracks the respective longitudinal helicity density trend in (e). The polarizability strength of the helically curved tip has been chosen same as the isotropic one of radius $r_{NP} = 80$ nm.

Appendix D

Exact expression of $Q_{in}(x, y, z)$:

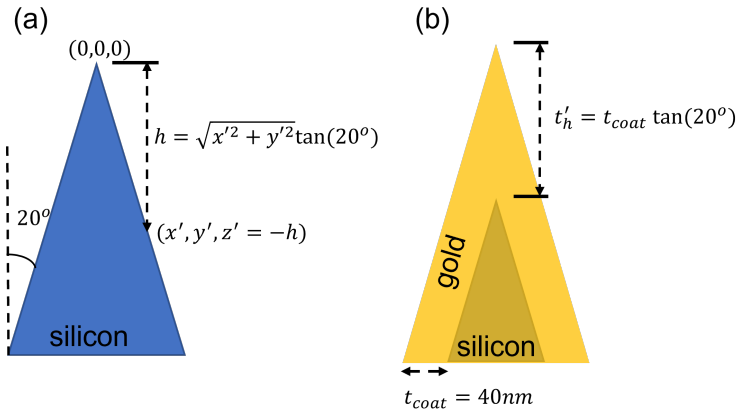

Figure D.1: Tip apex geometry and coordinate measurement for (a) bare silicon (b) gold coated silicon tip.

Figure D.1(a) shows the geometry considered at the tip apex for bare silicon tip with a half cone angle of 20^o. The center of the coordinate is chosen at the tip apex with negative z axis being along the tip axis inside the material. Considering all these geometric details, the volumetric heat equation becomes:

$$Q_{in}(x, y, z) = Q_o(1 - R_{c,Si})\frac{A_{c,Si}}{\pi\sigma_x\sigma_y}e^{-\frac{1}{2}[(\frac{x}{\sigma_x})^2+(\frac{y}{\sigma_y})^2]}e^{-A_{c,Si}|z+h|} \tag{D.1}$$

where, $R_{c,Si}$, $A_{c,Si}$ are the absorption coefficient and reflection coefficient of silicon and h is

the vertical distance from the $z = 0$ plane to the outer surface of the tip.

Figure D.1(b) shows the geometry considered at the tip apex for gold coated silicon tip. 40 nm thickness of gold is considered all around the tip that gives a vertical distance of $t'_h = t_{coat} tan(20^o)$ inside the coating. In gold coated silicon tip, the volumetric heat distribution would be different inside the coating layer and inside silicon. They can be defined as:

$$Q_{in}(x,y,z) = \begin{cases} Q_o(1-R_{c,Au})\frac{A_{c,Au}}{\pi\sigma_x\sigma_y} e^{-\frac{1}{2}[(\frac{x}{\sigma_x})^2+(\frac{y}{\sigma_y})^2]} e^{-A_{c,Au}|z+h|}; \text{(Au)} \\ Q_o(1-R_{c,Au})(A_{c,Au}t'_h)(e^{-A_{c,Au}t'_h})(1-R_{c,Si})\frac{A_{c,Si}}{\pi\sigma_x\sigma_y} e^{-\frac{1}{2}[(\frac{x}{\sigma_x})^2+(\frac{y}{\sigma_y})^2]} e^{-A_{c,Si}|z+t'_h+h|}; \text{(Si)} \end{cases} \tag{D.2}$$

where, $R_{c,Au}$, $A_{c,Au}$ are the absorption coefficient and reflection coefficient of gold.